공학박사 학위논문

Development of Flow Network Analysis Code for Core of Prismatic Very High Temperature Reactor

블록형 초고온가스로 노심 유동해석 네트워크 코드 개발 연구

2017 년 7 월

서울대학교 대학원

에너지시스템공학부

이 정 훈

Development of Flow Network Analysis Code for Core of Prismatic Very High Temperature Reactor

블록형 초고온가스로 노심 유동해석 네트워크 코드 개발 연구

지도교수 박 군 철

이 논문을 공학박사 학위논문으로 제출함
2017 년 6 월

서울대학교 대학원
에너지시스템공학부
이 정 훈

이정훈의 박사 학위논문을 인준함
2017 년 6 월

위 원 장 김 응 수 (인)

부위원장 박 군 철 (인)

위 원 조 형 규 (인)

위 원 김 민 환 (인)

위 원 황 수 현 (인)

Abstract

Development of Flow Network Analysis Code for Core of Prismatic Very High Temperature Reactor

Jeong-Hun Lee

Department of Energy System Engineering

The Graduate School

Seoul National University

The core of the prismatic very high temperature reactor (VHTR) consists of hexagonal prismatic fuel blocks and reflector blocks made of graphite. Therefore, there are interstitial gaps between blocks and the gap varies during core cycles due to the neutron-induced shrinkage of the graphite. If the core bypass flow ratio increases, the coolant channel flow is decreased and can then lower the heat removal efficiency, resulting in a locally increased fuel block temperature. Moreover, variations in the size of the gap increase the uncertainty of the core flow distribution.

Recently, the computational fluid dynamics (CFD) method has received a great deal of attention as a method for understanding the flow behavior in the VHTR core. However, the large computational cost and time required to implement CFD codes simulating the entire core hinder their application to analysis of the gap effect. An

alternative technique is the utilization of a system code, which uses lumped parameter model. The system code has advantages in computational time and cost but, the accuracy is relatively low. Therefore, to analyze flow distribution in the core of VHTR effectively, the flow network analysis code named FastNet (Flow Analysis for Steady-state Network) which uses looped network analysis method was developed in this study.

The flow network analysis code presents flow paths as a network of flow resistances, and thus requires the precise relation between the pressure loss and flow rate in given geometry. In the VHTR core, there are three types of flow paths: coolant channel, bypass gap, and cross gap. The coolant channel and the bypass gap can be analyzed using equations that relate the head loss due to friction along given length of channel. However, the relation between the pressure loss and flow rate at the cross gap cannot be analyzed easily because of its complex geometry. Moreover, the cross gap complicates the flow distribution in the connecting flow path between the coolant channel and bypass gap. For these reasons, the cross flow in the VHTR core was studied experimentally to enhance the calculation accuracy of the flow network code using the correlation of the cross flow loss coefficient. Thus, a cross flow experimental facility was constructed to investigate the cross flow phenomena in the core of the VHTR and a series of experiments were carried out under varying flow rates and gap sizes. The results of the experiments were compared with CFD (Computational Fluid Dynamics) analysis results in order to verify its prediction capability for the cross flow phenomena. Good agreement was seen between experimental results and CFD predictions and the local characteristics of the cross flow were investigated. Based on the calculation results, a correlation of pressure loss coefficient across the cross gap was developed and the developed correlation

was implemented in FastNet.

For heat transfer analysis, since the FastNet allocates 6 cells for one fuel block, the effective thermal conductivity (ETC) model was adopted. In this model, the thermal conductivities of all components in the multiple medium are homogenized to a single ETC in conjunction with the contribution of the radiation heat transfer. Moreover, the maximum fuel temperature model using unit cell was implemented to predict the highest temperature of fuel in a cell.

For verification and validation of FastNet, the calculation results were compared with CFD analysis results and experiments data. At first, flow network analysis capability was validated with the SNU multi-block experiment. Then, a single column analysis was simulated and compared with CFD analysis and CORONA calculation results. Finally, a whole core simulation was conducted to evaluate the calculation performance of FastNet and the simulation results were compared with results of CFD analysis and CORONA calculation. FastNet shows the fast calculation speed as well as reliable calculation results.

From the V&V results, it can be concluded that FastNet can provide reliable predictions on flow distribution and temperature distribution in the core of prismatic VHTR. Therefore, it is expected that FastNet can contribute to assure the core thermal margin.

Keywords

VHTR, Very High Temperature Reactor, Bypass flow, Cross flow, Looped network analysis, Pressure loss coefficient, Experiment, CFD (Computational Fluid Dynamics), Network code, Code V&V

Student Number: 2012-30267

List of Contents

Abstract ..... **i**

List of Contents ..... **v**

List of Tables ..... **vii**

List of Figures ..... **ix**

Chapter 1. Introduction **1**

1.1 Background 1

1.1.1 The Core of Very High Temperature Reactor 1

1.1.2 Studies on Bypass flow and Cross flow in the Core of VHTR 2

1.1.3 T/H Analysis Methods for the Prismatic VHTR Core 3

1.2 Objectives and Scope 4

Chapter 2. Development of FastNet **10**

2.1 Governing Equations 10

2.1.1 Conservation of Mass 11

2.1.2 Conservation of Momentum 12

2.2 Application of Linear Theory Method 12

2.3 Flow Network Modeling 14

2.3.1 Looped Network Analysis for Simple Loop 14

2.3.2 Looped Network Analysis for 3-D Network 16

2.3.3 Determination of Flow Resistance 18

Chapter 3. Cross Flow Experiment **35**

3.1 Review of Existing Studies on Cross Flow 36

3.1.1 Groehn's Experimental Study 37

3.1.2 Kaburaki's Experimental and Numerical Study 37

3.2 CFD Analysis and Assessment for Cross Flow Phenomena with Groehn's Experiments 39

3.2.1 Description of Groehn's Experimental Study 39

3.2.2 CFD Modeling 40

3.2.3 CFD Analysis Results 41

3.3 Cross Flow Experiment for the Core of GT-MHR 44

3.4 CFD Simulation of Cross Flow Experiment 47

3.4.1 Kaburaki's Experimental and Numerical Study 48
3.4.2 Results of the CFD Calculation Validation 49
3.4.3 Pressure Loss Coefficient 51
3.5 Correlation of Cross Flow Loss Coefficient for GT-MHR Core 52
Chapter 4. Heat Transfer Modeling in FastNet 87
4.1 Governing Equations 87
4.2 Effective Thermal Conductivity Model 89
4.3 Maximum Fuel Temperature Model 91
4.3 Procedure of FastNet 94
Chapter 5. Verification and Validation of FastNet 110
5.1 Validation of Flow Network Model 110
5.2 Code to Code Validation 112
5.2.1 Single Column Analysis 112
5.2.2 Whole Core Analysis 113
5.3 Whole Core Analysis ..... 오류! 책갈피가 정의되어 있지 않습니다.
Chapter 6. Conclusions 141
6.1 Summary 141
6.2 Recommendations 142
Nomenclature 144
References 146
Appendix A. Uncertainty Analysis for the Cross Flow Experiment 153
Appendix B. Flow Direction Dependency of Cross Flow Loss Coefficient 158
Appendix C. Friction Factor Model Sensitivity Test 161
Appendix D. y^+ Sensitivity Test for Gamma-Theta Model 165
국문 초록 175

List of Tables

Table 2.1 The relation between 3-D network and the number of equations 24

Table 3.1 Empirically determined constants, C_1 and C_2, in Eq. (3.4).....56
Table 3.2 Conditions of CFD modeling.....57
Table 3.3 Average velocity and maximum velocity in the cross gap (flow rate 1.0 kg/s) 58
Table 3.4 Cross flow rate 59
Table 3.5 Pressure values at the coolant channels in cross gap (flow rate 1.0 kg/s case) 60
Table 3.6 Flow velocity at the coolant channel of upstream block and downstream block.....61
Table 3.7 Main variables for scaling analysis.....62
Table 3.8 Test matrix.....63
Table 3.9 Measuring instruments.....64
Table 3.10 Uncertainties of the measured variables 65
Table 3.11 CFD simulation conditions 66
Table 3.12 Grid convergence test results 67

Table 4.1 Volume fraction for types of solid cell.....98

Table 5.1 Calculation conditions for single column analysis 115
Table 5.2 Coolant outlet temperature and maximum fuel temperature 116
Table 5.3 Coolant outlet temperature and maximum fuel temperature 117
Table 5.4 Flow distribution.....118
Table 5.5 Maximum temperature in the fuel columns [°C].....119
Table 5.6 Difference of temperatures [°C].....120
Table 5.7 Calculation speed of FastNet over that of CORONA 121

Table A.1 Readings of inlet and outlet flow rate. 157
Table A.2 Friction factor according to roughness.....163
Table A.3. y^+ values for two different mesh cases.....167

Table A.4 Variables for two different mesh cases 168

List of Figures

Figure 1.1 Core of prismatic VHTR (Strydom et al., 2013) 6
Figure 1.2 Bypass flow and cross flow 7
Figure 1.3 Flow network of core of prismatic VHTR 8
Figure 1.4 Outline of the study 9

Figure 2.1 Flow network with 1 loop and 4 pipes 25
Figure 2.2 Flow network with 20 loops and 49 pipes 25
Figure 2.3 Matrix form of the network with 20 loops and 49 pipes 26
Figure 2.4 Targeted 3-D network for one fuel block 27
Figure 2.5 Simple 3-D network of a cube and converted 2-D network for a cube 28
Figure 2.6 3-D network for a 2-layer cube and 2-D network for a 2-layer cube ... 29
Figure 2.7 Targeted network for the network analysis of prismatic VHTR core ... 30
Figure 2.8 Coolant channels in fuel block and the representative flow path for the network analysis 31
Figure 2.9 Two identical parallel flow paths 32
Figure 2.10 Control rod fuel block and control rod reflector block solid cell (red line) for FastNet 33
Figure 2.11 Pressure loss for sudden area change; sudden contraction at bypass gap and converging flow at the coolant channel 34

Figure 3.1 Groehn's experimental setup (Groehn, 1982) 68
Figure 3.2 Fuel block model of Kaburaki's study (Kaburaki, 1990) 69
Figure 3.3 Computational domain and mesh structure of cross gap (gap size 6 mm case) 70
Figure 3.4 Velocity streamlines at the cross gap in radial direction (flow rate 1 kg/s and cross gap widths 1.85, 3.75 and 6 mm in sequence order) 71
Figure 3.5 Pressure contours at the cross gap in radial direction (flow rate 1 kg/s and cross gap widths 1.85, 3.75, and 6 mm in sequence order) 72
Figure 3.6 Velocity contours in axial direction (flow rate 1.0 kg/s and cross gap widths 1.85, 3.75, and 6 mm in sequence order) 73

Figure 3.7 Flow velocity distribution under cross flow (flow rate 1.6 kg/s and for cross gap 6 mm) 74
Figure 3.8 Distribution of velocity difference between upstream block and downstream block under cross flow (flow rate 1.6 kg/s and for cross gap 6 mm) 75
Figure 3.9 Flow loss coefficient at the cross gap 76
Figure 3.10 Standard fuel block of PMR200 77
Figure 3.11 Standard fuel block of PMR200 78
Figure 3.12 Standard fuel block of PMR200 79
Figure 3.13 The cross flow rate and the cross flow ratio to the main flow rate 80
Figure 3.14 Computational domain and mesh structure 81
Figure 3.15 Comparison results for whole cases 82
Figure 3.16 Comparison of the CFD prediction and experiments for whole cases 83
Figure 3.17 Pressure loss coefficient at the cross gap 84
Figure 3.18 Comparison results of the loss coefficient correlations with the experimental data for whole cases 85
Figure 3.19 Comparison results of the loss coefficient correlations with the experimental data 86

Figure 4.1 Effective Thermal Conductivity model 99
Figure 4.2 Solid meshes and cell types for the control rod fuel block and control rod reflector block 100
Figure 4.3 Unit cell for Maximum Fuel Temperature model 101
Figure 4.4 1-D estimated conduction in unit cell for predicting maximum fuel temperature 102
Figure 4.5 CFD analysis results for unit cell model 103
Figure 4.6 Comparison results of Max Fuel Temp model and CFD analysis 104
Figure 4.7 The flow chart of FastNet 105
Figure 4.8 The example of meshes for flow network analysis and solid conduction analysis 106
Figure 4.9 The example of 3-D mesh for looped network analysis 107
Figure 4.10 Solid mesh for the example of calculation for solid conduction 108
Figure 4.11 Calculation of lateral mixing for energy balance 109

Figure 5.1 SNU multi-block experimental facility and block configuration and the fluid mesh for the experimental facility....122
Figure 5.2 Block configuration of each case....123
Figure 5.3 Comparative results of FastNet prediction and experimental data (BG2-CG0 case)....124
Figure 5.4 Comparative results of FastNet prediction and experimental data (BG6-CG0 case)....125
Figure 5.5 Comparative results of FastNet prediction and experimental data (BG6242-CG2 case)....127
Figure 5.6 Comparative results of FastNet prediction and CFD analysis (BG2-CG0 case)....128
Figure 5.7 Comparative results of FastNet prediction and CFD analysis (BG6-CG0 case)....129
Figure 5.8 Comparative results of FastNet prediction and CFD analysis (BG6242-CG2 case)....130
Figure 5.9 Calculation domain for CFD and network model of FastNet....131
Figure 5.10 Comparison results of CFD analysis and FastNet prediction (axial distribution of hottest fuel compact)....132
Figure 5.11 Temperature distribution at Line AB (CFD and FastNet)....133
Figure 5.12 Residual graph of CFX calculation (left: momentum and mass, middle: heat transfer, right: turbulence KE)....134
Figure 5.13 Comparison of calculation time between FastNet and CORONA....135
Figure 5.14 1/6 core model for CFD calculation (S.N. Lee, 2017)....136
Figure 5.15 Fuel column number and power peaking factor....137
Figure 5.16 FastNet calculation results of flow distribution and temperature distribution of core....138
Figure 5.17 Comparison results of temperature distributions at the hot spot plane (CFX, CORONA, FastNet)....139
Figure 5.18 Comparison of calculation time between FastNet and CORONA for whole core simulation....140

Figure A.1 Two different conditions with the opposite direction of cross flow....159
Figure A.2 Pressure loss coefficient for cross flow....160
Figure A.3 Turbulent intermittency distributions in axial direction (left: high y^+, right: low y^+)....169

Figure A.4 Turbulent intermittency distribution in radial direction (left: high y^+, right: low y^+).....170
Figure A.5 Velocity distribution in axial direction (left: high y^+, right: low y^+)..171
Figure A.6 Velocity distribution in radial direction (left: high y^+, right: low y^+) 172
Figure A.7 Pressure distribution at the cross gap in radial direction (left: high y^+, right: low y^+).....173
Figure A.8 Velocity streamline at cross gap in radial direction (left: high y^+, right: low y^+).....174

Chapter 1

Introduction

1.1 Background

1.1.1 The Core of Very High Temperature Reactor

The Very High Temperature Reactor (VHTR), one of the Generation-IV (Gen-IV) reactors, is uranium-fueled, graphite-moderated and helium-cooled reactor. It has several advantages of enhanced fuel integrity, proliferation resistance, relatively simple fuel cycle and modularity to supply electricity (Gauthier et al., 2006). Prismatic VHTR is one of the prospective VHTR type candidates and it was reported that the graphite block shape has advantages for neutron economy and high temperature structural integrity (Baxter et al., 2000).

The core of prismatic VHTR consists of assemblies of hexagonal graphite fuel blocks as shown in Fig. 1.1 (Strydom et al., 2013). Between the fuel blocks, there exist vertical and horizontal gaps for reloading of the fuel elements. The gaps can be enlarged and their shapes can be changed by thermal expansion and fast-neutron induced shrinkage. Thus, a certain portion of the helium coolant can flow through these gaps between fuel blocks; the flow that passes through the vertical gaps is called a bypass flow and one through the horizontal gaps is called a cross flow as

depicted in Fig. 1.2. Furthermore, the shape of the graphite blocks changes during the reactor operation because of neutron damage and thermal expansion (General Atomics, 1988). From the Fort St. Vrain high temperature gas-cooled reactor operation experience, it was reported that the fluctuation event of the primary coolant outlet temperature and the reactor power was caused by the bypass flow and the cross flow (Olson et al., 1982). From that experience, the importance of bypass flow and cross flow has been raised and some studies on the bypass flow and the cross flow have been carried out.

1.1.2 Studies on Bypass flow and Cross flow in the Core of VHTR

Groehn (1982) studied the effect of cross flow on the main coolant flow at a two-block test section with a wedge-shaped gap. Kaburaki and Takizuka (1990) studied the cross flow characteristics experimentally and numerically for a parallel gap and a wedge-shaped gap. Sato et al. (2010) investigated the cooling effect of bypass flow using computational fluid dynamics (CFD) and concluded that the coolant outlet temperatures increase with an increase in the gap-width and, also, the bypass flow causes a large lateral temperature gradient in the block. Johnson and Sato (2012) carried out the CFD analysis for a one-twelfth symmetric sector for normal operation in a 350 MWth prismatic VHTR. It was shown that the effect of increasing gap width causes increased maximum fuel temperature while providing significant cooling to the near-gap region. Kim and Lim (2011) evaluated the local gap size variation between graphite blocks and conducted the analysis for the core bypass flow and hot spot based on the calculated gap distributions. Yoon et al. (2011, 2012) conducted the experimental study and CFD analysis for multi-block facility

with varying bypass gap size and cross gap size. The CFD model was validated with the experimental data and the effect of the bypass flow and cross flow on the flow distribution in prismatic VHTR core was investigated. Tung et al. (2012) investigated the effects of graphite surface roughness on bypass flow in HTGR with CFD analysis and the results indicated that increasing surface roughness increases the maximum fuel and helium temperatures as do increases in gap width. Wang et al. (2014 and 2016) and Worasit et al. (2016) conducted the CFD analysis and experimental study to investigate the coolant distribution in the reactor core based on the two-layer block facility built at Texas A&M University, which is a small-scale model for a portion of prismatic core of VHTR. They provided experimental data and a guideline and validating source for the related experiments. They found out that the pressure drop in the bypass gap was a function of the Reynolds number in the gap and the bypass gap size. From above, because of the uncertainty of the flow distribution in the core of VHTR, the analysis of the flow distribution has been conducted with numerical codes.

1.1.3 T/H Analysis Methods for the Prismatic VHTR Core

As the studies on the flow analysis of core of prismatic VHTR have been conducted with CFD codes, CFD codes have lots of advantages such as predicting local temperature and local flow field in detail. However, they require vast computational cost and time as well as efforts to generating computational grids. Considering the efforts to regenerating grids for various gap conditions, CFD codes have clear limitation of application for whole core analysis for the prismatic VHTR since when designing a reactor core, lots of cases should be tested.

The second option could be system codes such as GAMMA+ (Lim et al., 2006) and RELAP5-3D (INL, 2009). The system codes have strengths in transient calculation and relatively low calculation cost and time thanks to their coarse mesh and one-dimensional flow analysis. However, the accuracy of the system codes is not enough for the thermo-fluid analysis of core of prismatic VHTR.

The other option could be the CORONA code (Tak et al., 2014) which uses 1-D analysis for fluid and 3-D analysis for solid conduction. It has great advantages in calculation time and cost because of 1-D fluid analysis and great accuracy thanks to 3-D solid conduction analysis.

1.2 Objectives and Scope

The objectives of this study are to develop a flow network analysis code for core of prismatic VHTR, which can compute whole core analysis in short time with acceptable accuracy. When designing a reactor, calculation time of design code is one of critical features since various design options and conditions should be considered and covered. Therefore, the improving calculation speed of the code was focused in this study. To speed up of the code, flow network analysis method was implemented.

The flow network code requires the information of relation between pressure loss and flow rate and it presents flow paths as a network of flow resistances. In the core of VHTR, there are three types of flow paths; coolant channel, bypass gap, and cross gap and those flow paths can be represented as a flow network as shown in Fig. 1.3. The coolant channel is a normal pipe flow and the bypass gap is the flow path between parallel plates which can be analyzed using equations which relate

the head loss or pressure loss due to friction along a given length of channel to average velocity of the fluid flow. However, the relation between the pressure loss and flow rate at the cross gap cannot be analyzed easily because of its complex geometry. Moreover, the cross gap complicates the flow distribution connecting flow paths; the coolant channel and bypass gap. From those reasons, the experimental study on the cross flow in the core of VHTR was carried out to develop a correlation of pressure loss coefficient for the cross flow. Then, the developed correlation was implemented to the network code to enhance the calculation accuracy. The developed correlation could be applied to other codes such as CORONA and GAMMA+ and improve their calculation accuracies.

For the capability of heat transfer analysis of the developed code, Effective Thermal Conductivity (ETC) model was used since the code allocates 6 solid meshes for a fuel block. Because of the coarse mesh, the code cannot calculate the local temperature. However, since what is of interest is the maximum fuel temperature, a prediction model is required. Hence, the prediction model for maximum fuel temperature was introduced using unit-cell based model.

To confirm the calculation capability of the network code, validation was carried out with experimental data and CFD analysis results. As validation data, the SNU multi-block experiment (Yoon et al., 2012) was used. For the code-to-code validation of the network code, a single column analysis was simulated and compared with CFD analysis and CORONA calculation results. Finally, to confirm the performance of the developed code, whole core analysis was conducted and the results was also compared with results of CFD analysis and CORONA calculation. The outline of this study was presented in Fig. 1.4.

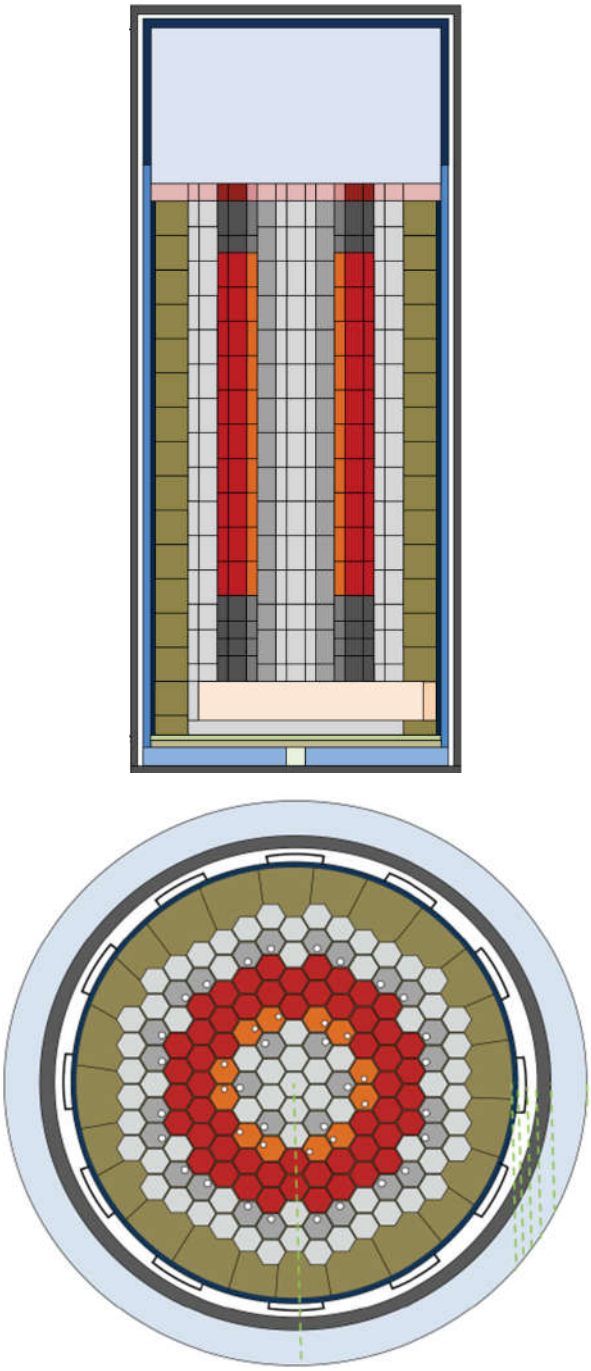

Figure 1.1 Core of prismatic VHTR (Strydom et al., 2013)

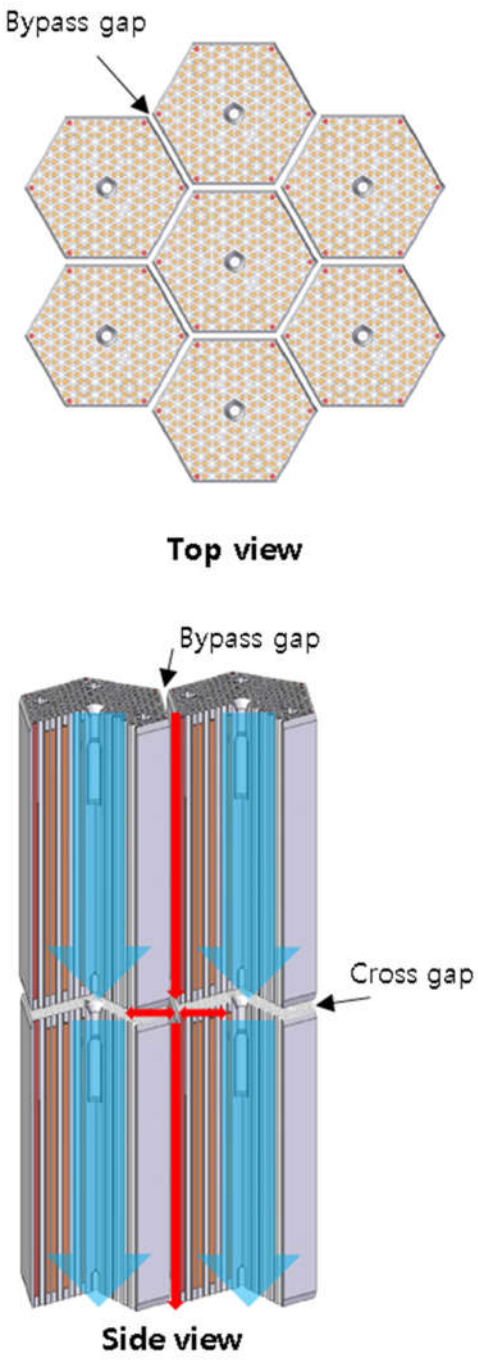

Figure 1.2 Bypass flow and cross flow

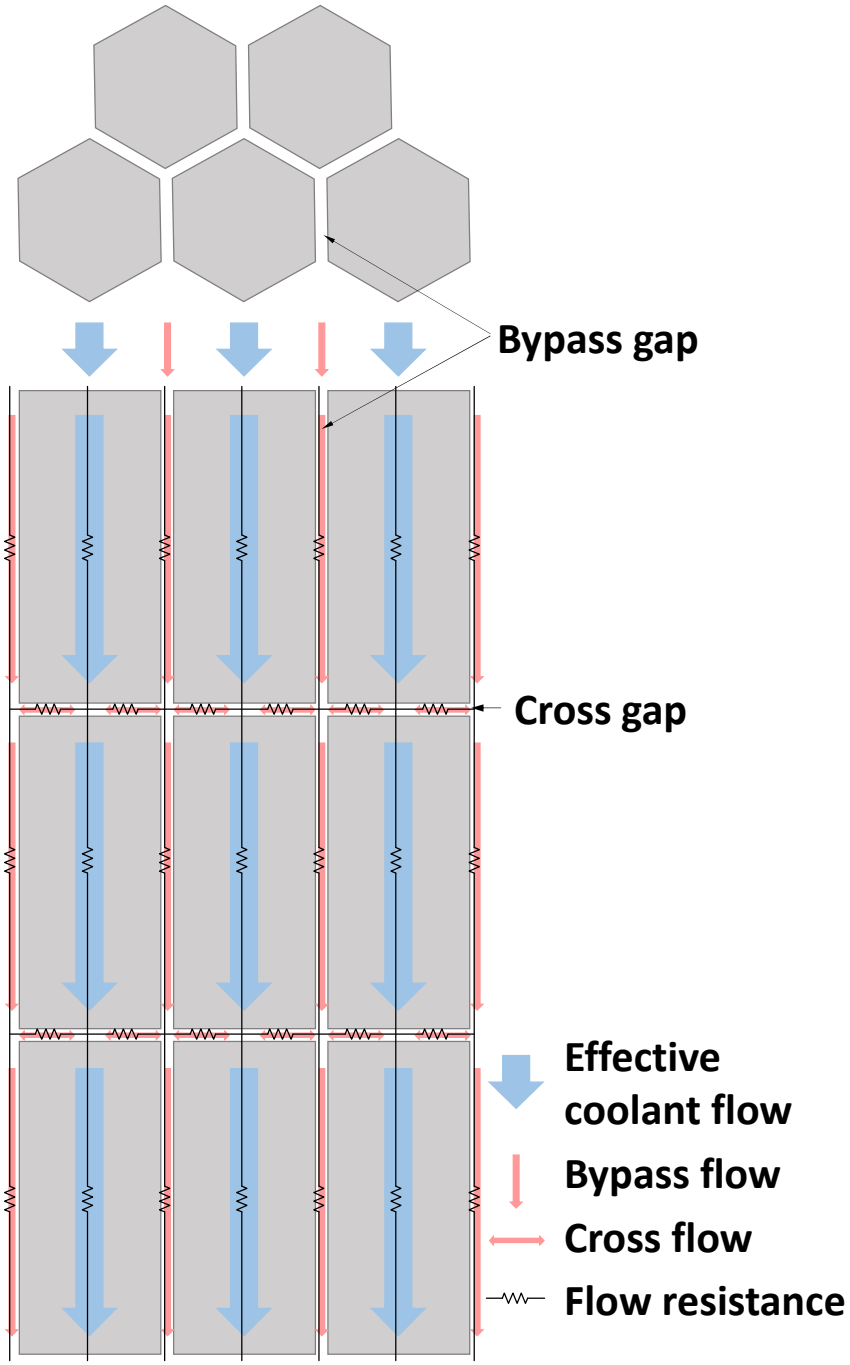

Figure 1.3 Flow network of core of prismatic VHTR

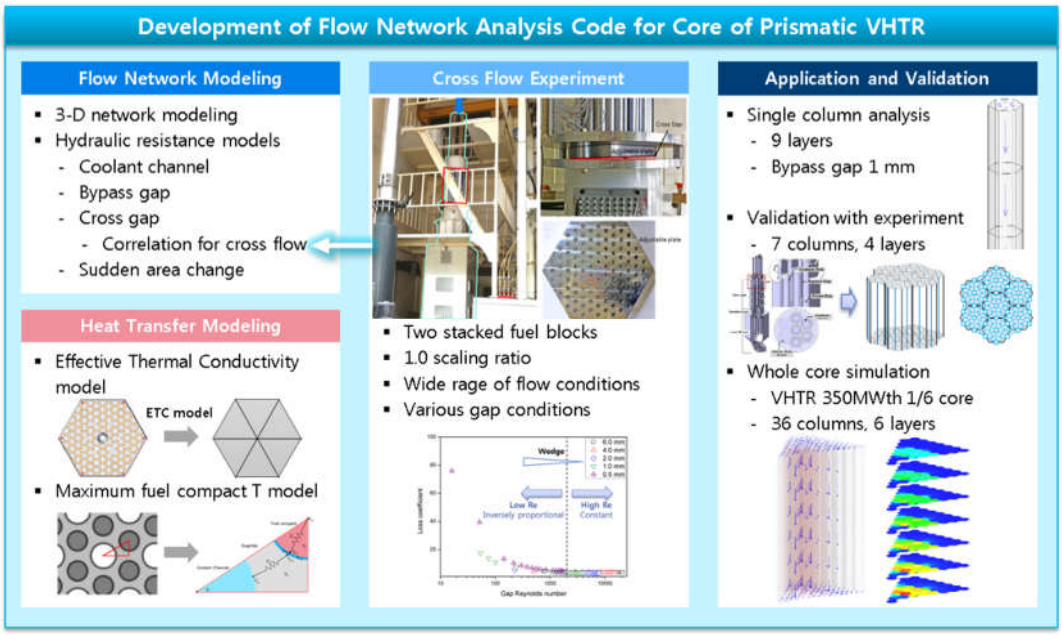

Figure 1.4 Outline of the study

Chapter 2

Development of FastNet

2.1 Governing Equations

In the VHTR core, main flows are pipe flows and pipe flow is usually calculated with Darcy-Weisbach equation. The form of Darcy-Weisbach equation is Eq. (1).

$$h_f = f\frac{L}{D}\frac{V^2}{2g} \tag{2.1}$$

Where h is head loss, f is friction factor, L is length of the flow path, D is diameter of path, V is flow velocity, and g is the gravity acceleration.

To analyze network, Eq. (2.1) can be expressed as relation of head loss and flow rate.

$$h_f = RQ^2, \qquad where\, R = \frac{fL}{2gDA^2} \tag{2.2}$$

Where A is flow area, Q is the volumetric flow rate, and R is the loss factor that can be thought as flow resistance.

If a network has one or more closed loop, it is called looped network. In a simple pipe network, the flow is unique and can be obtained easily. However, in case of a looped network, the number of pipes is too large to find the flows by merely applying flow continuity equations at nodes. Furthermore, nonlinearity of the head and flow rate makes the problem more difficult. The analysis of looped network consists of the determination of flow rates of the pipes and heads at the nodes. The following laws, called Kirchhoff's circuit laws (Paul, 2001), generate the governing equations.

- The algebraic sum of inflow and outflow discharges at a node is zero.
- The algebraic sum of the head loss around a loop is zero

2.1.1 Conservation of Mass

Conservation of mass at a node is established based on the law that the amounts of inflow and outflow are same at the junction where the pipes are connected. In another word, the sum of inflow and outflow at a node is zero. For a junction node j, conservation of mass can be written as Eq. (2.3).

$$F_j = \sum_{n=1}^{j_n} Q_{jn} = 0 \tag{2.3}$$

Where, Q_{jn} is the inlet flow from *n-th* pipe at node j, q_j is the outlet flow at the node, and j_n is the total number of pipes at node j. This mass equation is used at every node in the system and so, it can be referred as nodal equation.

2.1.2 Conservation of Momentum

The conservation equation of momentum can be represented with head loss. Hence, the momentum equation can be called as head loss equation. While traversing along a loop, as one reaches at the starting node, the net head loss is zero. In short, the sum of the head loss around a loop is zero. It can be written as Eq. (2.4).

$$F_k = \sum_{n=1}^{k_n} R_{kn} \left| Q_{kn} \right| Q_{kn} = 0 \tag{2.4}$$

Where, K_n is the total number of pipes at the *k-th* loop. Since one loop has one head loss equation, it can be referred as loop equation.

2.2 Application of Linear Theory Method

The linear theory method is a looped network analysis method presented by Wood and Charles (1972). The entire network is analyzed altogether by calculating matrix. The nodal flow continuity equations are obviously linear but the looped head-loss equations are nonlinear. In this method, the looped momentum equations are modified to be linear for previously known discharges and solved iteratively. The process is repeated until the two solutions are close to the allowable limits. The nodal equations are Eq. (2.3). It can be generalized in the following form for the entire network as Eq. (2.5).

$$F_j = \sum_{n=1}^{i_L} a_{jn} Q_{jn} = 0 \tag{2.5}$$

Where a_{jn} is +1 if positive discharge flows in pipe n, -1 if negative discharge flows in pipe n, and 0 if pipe n is not connected to node j. The total pipes in the network are i_L. The loop head-loss equations are Eq. (2.4). It can be linearized as Eq. (2.6).

$$F_k = \sum_{n=1}^{k_n} b_{kn} Q_{kn} = 0 \tag{2.6}$$

Where $b_{kn}=R_{kn}|Q_{kn}|$ for initially known pipe discharges. The coefficient b_{kn} is revised with current pipe discharges for the next iteration. This results in a set of linear equations, which are solved by using any standard method for solving linear equations. Thus, the total set of equations required for i_L unknown pipe discharges are

- Nodal continuity equations for $n_L - 1$ nodes
- Loop head-loss equations for k_L loops

The overall procedure for looped network analysis by the linear theory method can be summarized in the following steps:

Step 1: Number pipes, nodes, and loops.

Step 2: Write nodal discharge equations as Eq. (2.3).

Step 3: Write loop head-loss equations as Eq. (2.6).

Step 4: Assume initial pipe flows, Q_1, Q_2, Q_3, … arbitrarily.

Step 5: Generalize nodal continuity and loop equations for the entire network.

Step 6: Calculate pipe discharges. The form of generated equation is $\boldsymbol{Ax=b}$, which can be solved for Q_i.

Step 7: Recalculate coefficients b_{kn} from the obtained Q_i values.

Step 8: Repeat the process again until the calculated Q_i values in two consecutive iterations are close to predefined limits.

2.3 Flow Network Modeling

2.3.1 Looped Network Analysis for Simple Loop

Assuming a flow network with 1 loop and 4 pipes as shown in Fig. 2.1, 4 node equations and 1 loop equation can be obtained. Since 1 node equation is linearly dependent with other 3 node equations, 1 node equation should be removed. Hence, from the network, 3 node equations and one loop equation are finally obtained. Since the unknown variables are 4 flow rates for 4 pipes, solving the 4 equations can give the desired solution. In the network code, the linear equations are solved in the form of a matrix as seen in Eq. (2.9).

$$\begin{cases} Q_{total} = Q_1 + Q_2 \\ -Q_1 + Q_3 = 0 \\ -Q_2 + Q_4 = 0 \\ Q_3 + Q_4 = Q_{total} \end{cases} \tag{2.7}$$

$$R_1|Q_1|Q_1 + R_3|Q_3|Q_3 - R_2|Q_2|Q_2 - R_4|Q_4|Q_4 = 0 \tag{2.8}$$

$$\begin{pmatrix} +1 & +1 & 0 & 0 \\ -1 & 0 & +1 & 0 \\ 0 & -1 & 0 & +1 \\ b_1 & b_2 & b_3 & b_4 \end{pmatrix} \begin{pmatrix} Q_1 \\ Q_2 \\ Q_3 \\ Q_4 \end{pmatrix} = \begin{pmatrix} Q_{total} \\ 0 \\ 0 \\ 0 \end{pmatrix} \tag{2.9}$$

Applying this method to a network with 20 loops and 49 pipes (flow paths) as depicted in Fig. 2.2, 30 node equations and 20 loop equations can be obtained and, finally, 49 equations are obtained by excluding one from the node equations. From here, since the number of unknowns and that of equations are the same, the desired solution can be obtained. By generalizing this rule for 2-D network, the governing equations can be constructed by the total node equations except one and the total loop equations for the entire network. Fig. 2.3 is the matrix for solving the flow network with 20 loops and 49 pipes. The matrix for solving flow networks is difficult to apply the iterative solver because the matrix components are located irregularly and the size difference of the coefficients is too large. To handle this problem, direct method solver, CSparse, was adopted and this solver has following five characteristics (Davis, 2006).

1. Embodying much of the theory behind sparse matrix algorithms
2. Being either asymptotically optimal in its run time and memory usage or fast in practice
3. Being concise so as to be easily understood and short enough to print in the book
4. Covering a wide spectrum of matrix operations
5. Being accurate and robust

2.3.2 Looped Network Analysis for 3-D Network

Although 2-D network analysis is possible through the above method, 3-D network which is targeted network cannot be analyzed directly and has not been attempted yet. Hence, in this study, method for the looped network analysis of 3-D network was developed. The developed method was applied to the 3-D network of core of prismatic VHTR thereby the network could be effectively analyzed.

To construct governing equations, there are two basic rules as followings.

- The total number of equations should be the same as that of pipes (flow paths).
- Any equations should not be made up of manipulating other equations (linearly dependent).

For a targeted network of one fuel block, the network consists of 14 nodes, 24 loops and 31 pipes (flow paths) as depicted in Fig. 2.4. Applying previous method to the network, the number of governing equations is 37 (13 node equations + 24 loop equations). However, since the number of unknowns are 31, 6 equations are linearly dependent on other equations and should be diminished. To find out linearly dependent equations, simple 3-D network for a cube was assumed as descripted in the upper side of Fig. 2.5. The numbers of nodes, loops, and pipes are 8, 6, and 12, respectively. Since the number of equations from previous method is 13, it means that there is one linearly dependent equation. The lower side of Fig. 2.5 is a converted 2-D network for a cube. From Fig. 2.5, the loop equation through nodes 4-5-6-7 is linearly dependent on other loop equations. For a 2-layer 3-D network,

the numbers of nodes, loops, and pipes are 12, 11, and 20, respectively as depicted in Fig. 2.6. Hence, according to the previous method, the total number of governing equations is 22. Likewise, 2 equations are linearly dependent on other equations and should diminished. As shown in the lower side of Fig. 2.6, the loops through nodes 4-5-6-7 and 8-9-10-11 are linearly dependent on other equations. From this scheme, for 3-D networks, the equations for horizontal loops except for one should be diminished. To generalize this scheme for 3-D network analysis, the scheme was applied to the targeted network as shown in Fig. 2.7. The targeted network was composed of 2 layers of 7 fuel-block columns. If the top horizontal face network is called the base face network, the numbers of layers, base nodes, base loops, and base pipes are L, n, l, and p ($= n - 1 + l$), respectively. Through the improved method, the total number of governing equations T_{GE} can be written by Eq. (2.10).

$$T_{GE} = (L+1) \cdot n - 1 + l + L \cdot p \tag{2.10}$$

The total number of pipes for the entire network can be written by Eq. (2.11).

$$P_{Total} = (L+1) \cdot p + L \cdot n \tag{2.11}$$

If the number of equations is equal to the number of unknowns (total pipes), Eq. (2.10) should be the same as Eq. (2.11).

$$
\begin{aligned}
T_{GE} &= (L+1)\cdot n - 1 + l + L\cdot p \\
&= L\cdot n + (n-1+l) + L\cdot p \\
&= L\cdot n + p + L\cdot p \\
&= L\cdot n + (L+1)p = P_{Total}
\end{aligned}
\tag{2.12}
$$

From Eq. (2.12), it is confirmed that the number of unknown is equal to the number of governing equations. Therefore, it can be said that the governing equations consist of node equations except one ($(L+1)\cdot n - 1$), base-loop equations (l), and vertical loop equations ($L \cdot p$). The relationship between the number of equations and network is tabulated in Table 2.1.

2.3.3 Determination of Flow Resistance

- Coolant channels (pipe flow)

Since the coolant channel is typical pipe flow, Darcy-Weisbach equation can be applied directly. the flow resistance for the coolant hole is expressed as Eq. (2.13).

$$
R_{CH} = \frac{fL}{2gD_{CH}A_{CH}^2} \tag{2.13}
$$

Where, D_{CH} is diameter of coolant channel and A_{CH} is area of coolant channel. In Eq. (2.13), an alternative explicit formula given by Haaland (1983) is used to calculate Darcy friction factor f as Eq. (2.14).

$$\frac{1}{f^{1/2}} \approx -1.8\log\left[\frac{6.9}{\mathrm{Re}_d} + \left(\frac{\varepsilon / d}{3.7}\right)^{1.11}\right] \tag{2.14}$$

Where, ε, d, and Re_d are the roughness of the pipe, diameter of the pipe, and Reynolds number of the fluid which flows in the pipe, respectively.

Since one fuel block has 108 coolant channels, the coolant channels in one block can be simplified by one flow path representing 108 parallel flow paths as depicted in Fig. 2.8. For the two identical parallel flow paths as described in Fig. 2.9, head losses of both end of two parallel flow path are the same as Eq. (2.15) and the total flow rate are the same of the sum of two parallel flow rates as Eq. (2.16).

$$h_{Total} = h_1 = h_2 \tag{2.15}$$

$$Q_{Total} = Q_1 + Q_2 = 2Q_1 \tag{2.16}$$

From Eq. (2.2), the relation between flow resistance and flow rate for the parallel flow is as Eq. (2.17).

$$R_{Total}\left(Q_1 + Q_2\right)^2 = R_1 Q_1^2 = R_2 Q_2^2 \tag{2.17}$$

Hence, the total flow resistance can be written as Eq. (2.18).

$$R_{Total} = \frac{R_1 Q_1^2}{\left(Q_1 + Q_2\right)^2} = \frac{R_1 Q_1^2}{\left(2Q_1\right)^2} \tag{2.18}$$

Finally, for n identical parallel flow paths, the total flow resistance can be expressed as Eq. (2.19).

$$R_{Total} = \frac{R_1 Q_1^2}{\left(nQ_1\right)^2} = \frac{R_1}{n^2} \tag{2.19}$$

For the targeted network, one flow path represents 108 coolant channels for a standard fuel block, the flow resistance should be divided to square of the number of coolant channels because coolant channels in a fuel block are parallel flow paths.

- Control rod hole / reserved shutdown hole

Control fuel block has a control rod hole of which diameter is 10.16 cm (9.53 cm for reserved shutdown hole) as described in Fig. 2.10. Since the geometry of the control rod hole is a simple pipe, it can be analyzed by Darcy-Weisbach equation like coolant hole. In this network code, since a block has only one flow path for coolant channels, a control rod hole / reserved shutdown hole should be simplified with other coolant channels in the block. And since the control hole can be clogged and opened, if the control hole is clogged and a stagnant flow is formed, it is assumed there is no flow in the control hole.

- Bypass gap

Bypass gap is modeled as a gap between the parallel plates. Head loss of the bypass gap is calculated by Darcy-Weisbach equation as well as coolant hole. Since the bypass gap is not circular pipe, the hydraulic diameter of the bypass gap is calculated by Eq. (2.20).

$$D_{BGh} = \frac{4 \times Flow\ Area}{Wetted\ Perimeter} = \frac{4 \times b\delta_{BG}}{2b} = 2 \times \delta_{BG} \tag{2.20}$$

Therefore, the flow resistance for bypass gap can be expressed as Eq. (2.21).

$$R_{BG} = \frac{fL}{2gD_{BGh}A_{BG}^2} \tag{2.21}$$

Where, A_{BG} is area of bypass gap.

- Cross gap

As aforementioned before the coolant channel is a normal pipe flow and the bypass gap is the flow path between parallel plates which can be analyzed using equations which relate the head loss or pressure loss due to friction along a given length of channel to average velocity of the fluid flow. However, the relation between the pressure loss and flow rate at the cross gap cannot be analyzed easily because of its complex geometry. To develop correlation for pressure loss of cross flow, the experimental study was carried out and the developed correlation was implemented to FastNet. The flow resistance for cross gap is written as Eq. (2.22).

$$R_{CG} = \rho \cdot \frac{0.63 / (\delta_{CG}\,\mathrm{Re}_{CG}) + 3.5}{2A_{CG}^2} \tag{2.222}$$

Where, δ is cross gap width, ρ is density of the working fluid, Re_{CG} is Reynolds number at the cross gap opening and A_{CG} is the area of the cross gap opening. The detailed information of experimental study will be presented in Chapter 3.

- Hydraulic resistance for sudden area change

If the bypass gap width varies for each layer, sudden area change of the bypass gap makes sudden contraction/expansion effect at the bypass gap and converging flow at the coolant channel as illustrated in Fig. 2.11. For the bypass gap (red stream line), sudden contraction effect was modeled by using Eqs. (2.23) and (2.24).

$$h_L = \frac{\left(V_1 - V_2\right)^2}{2g} \tag{2.233}$$

And

$$K_L = \left(1 - \frac{V_2}{V_1}\right)^2 \tag{2.244}$$

On the other hand, as shown in Fig. 3.20, for the coolant channel (blue streamline), converging flow was modeled using Eq. (2.25) by Idelchik (1996).

$$K_s = \frac{\Delta h_s}{\frac{V_s^2}{2g}} = \frac{K_{c,s}}{\left(1 - \frac{Q_b}{Q_c}\right)^2} \quad \text{where,} \quad K_{c,s} = \frac{\Delta h_s}{\frac{V_c^2}{2g}} = 1.55\frac{Q_b}{Q_c} - \left(\frac{Q_b}{Q_c}\right)^2 \tag{2.255}$$

In addition, sudden expansion occurs at the end of pipe, which leads to pressure recovery. The pressure recovery was modeled using Boarda-Carnot equation as Eq. (2.26).

$$\Delta h = -\frac{1}{g}\frac{A_1}{A_2}\left(1-\frac{A_1}{A_2}\right)V_1^2 \qquad (2.266)$$

Table 2.1 The relation between 3-D network and the number of equations

Layers	L
Base nodes	n
Base loops	l
Base pipes	$p\ (= n - 1 + l)$
Total nodes	$(L + 1) \cdot n$
Total loops	$(L + 1) \cdot l + L \cdot p$
Total pipes	$(L + 1) \cdot p + L \cdot n$
Total equations	$(L + 1) \cdot n - 1 + l + L \cdot p$

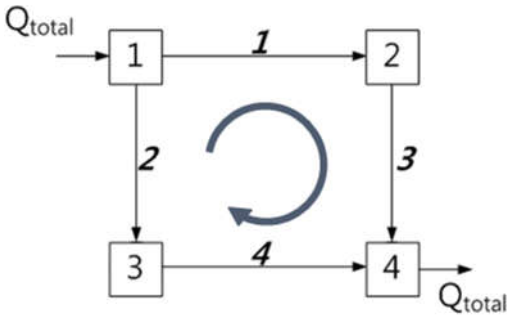

Figure 2.1 Flow network with 1 loop and 4 pipes

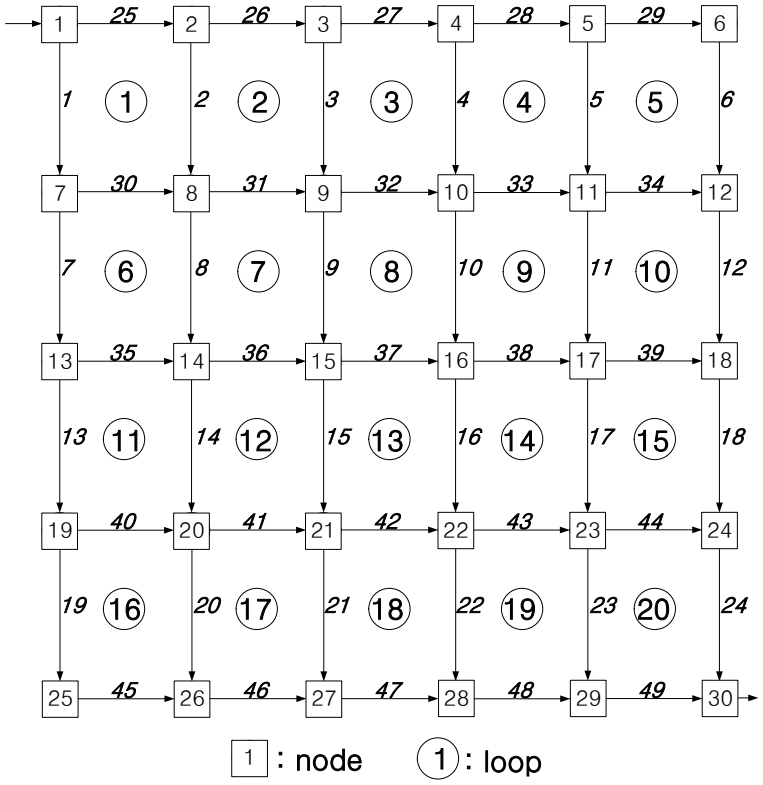

Figure 2.2 Flow network with 20 loops and 49 pipes

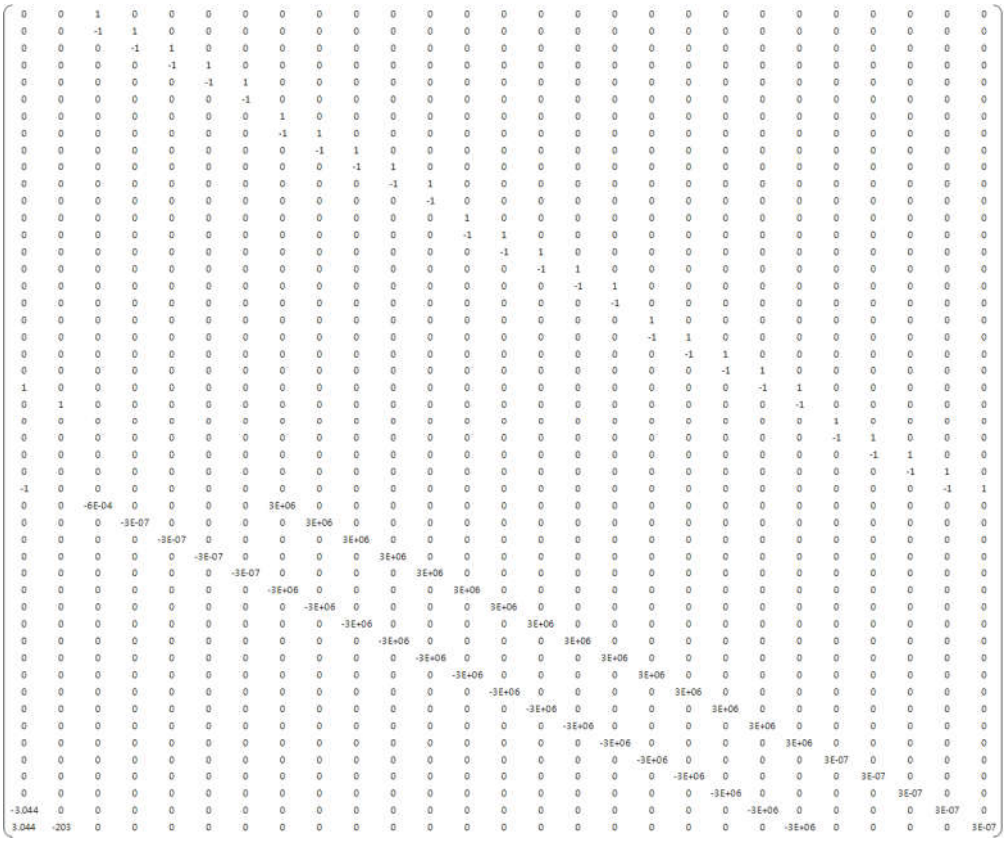

Figure 2.3 Matrix form of the network with 20 loops and 49 pipes

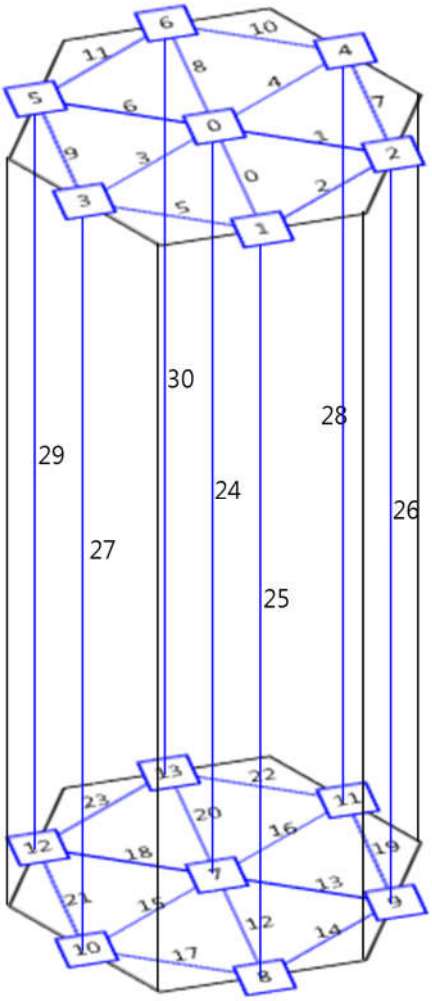

Figure 2.4 Targeted 3-D network for one fuel block

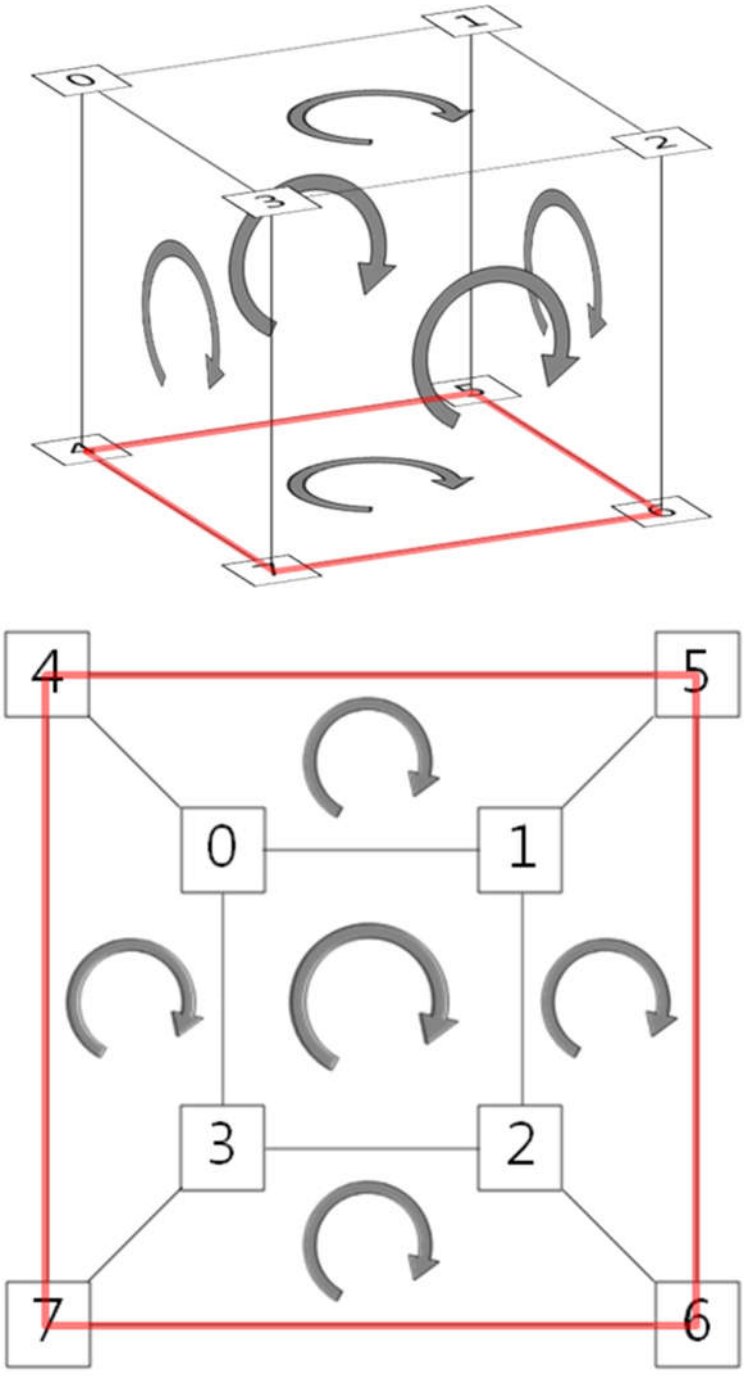

Figure 2.5 Simple 3-D network of a cube and converted 2-D network for a cube

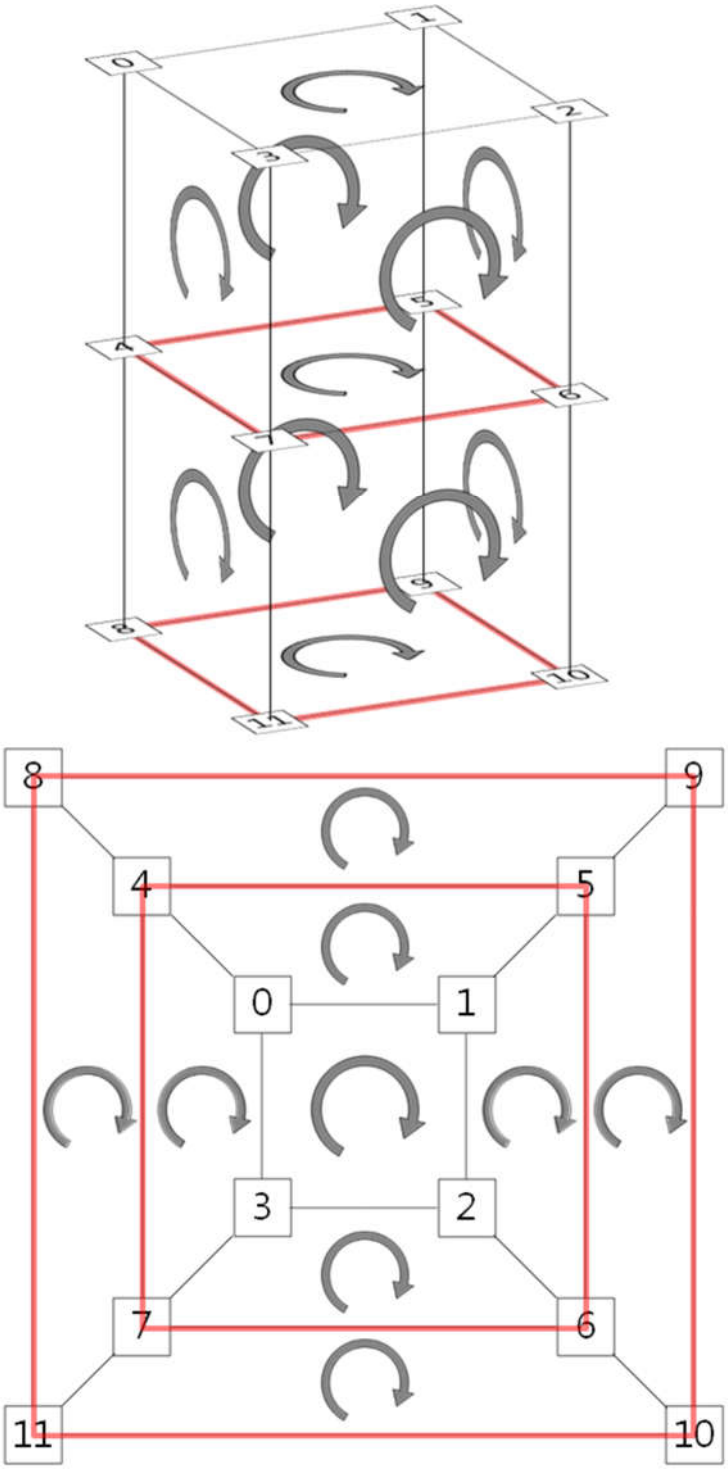

Figure 2.6 3-D network for a 2-layer cube and 2-D network for a 2-layer cube

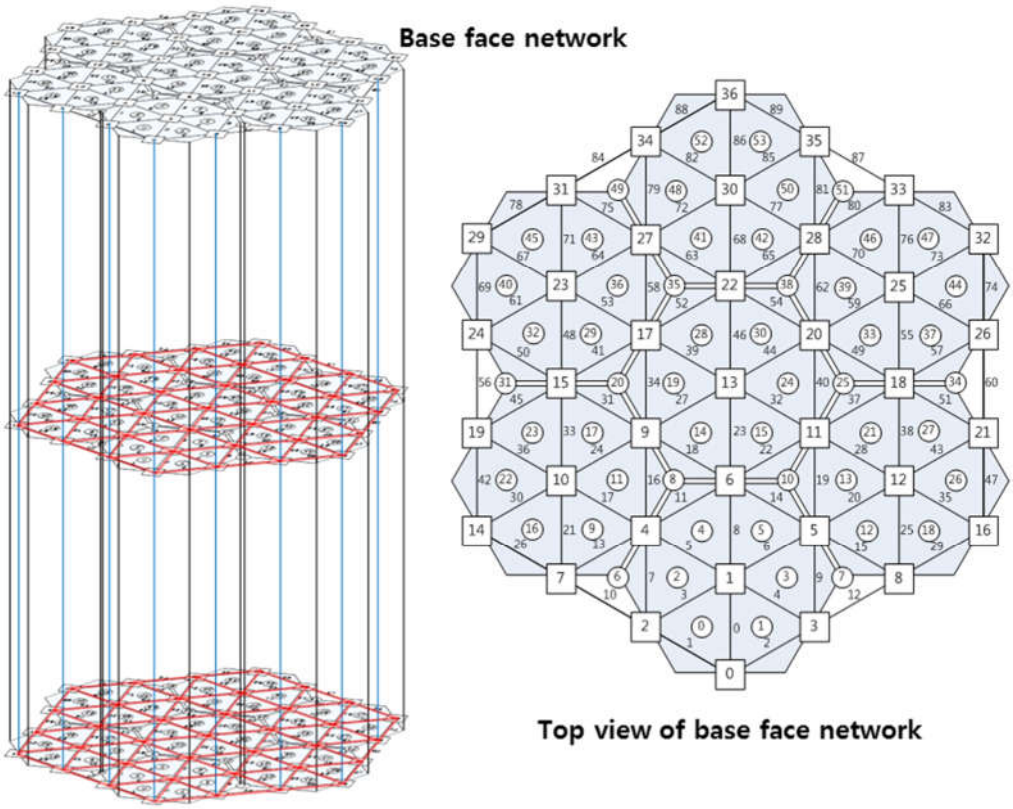

Figure 2.7 Targeted network for the network analysis of prismatic VHTR core

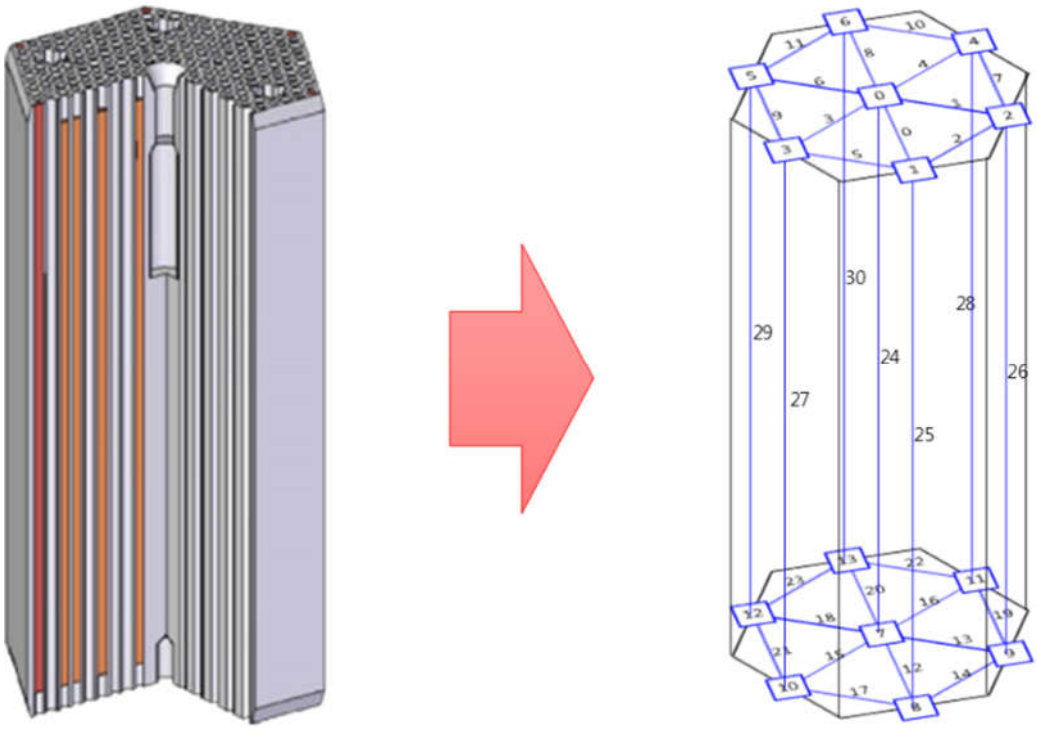

Figure 2.8 Coolant channels in fuel block and the representative flow path for the network analysis

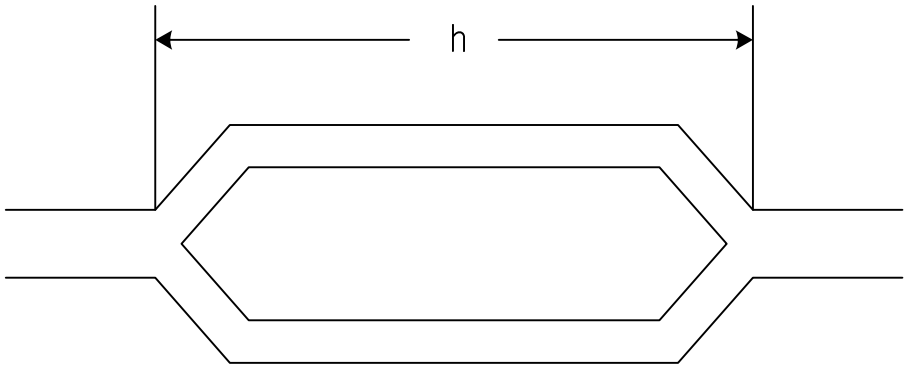

Figure 2.9 Two identical parallel flow paths

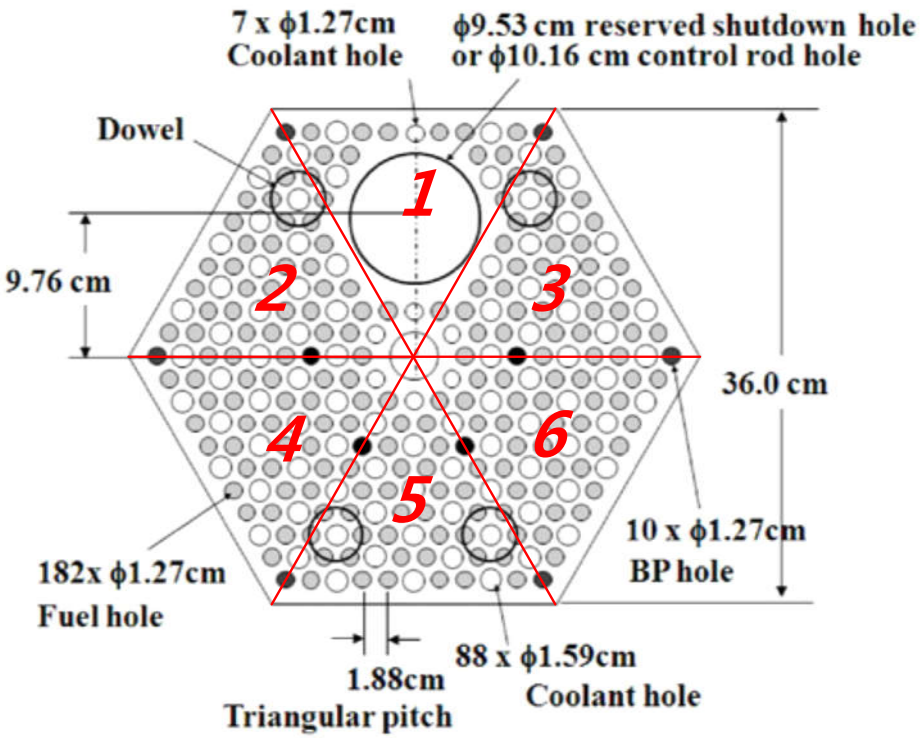

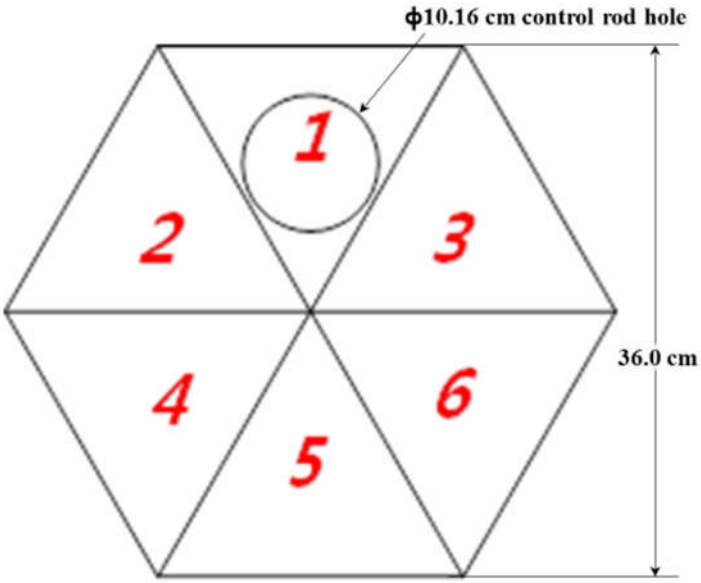

Figure 2.10 Control rod fuel block and control rod reflector block solid cell (red line) for FastNet

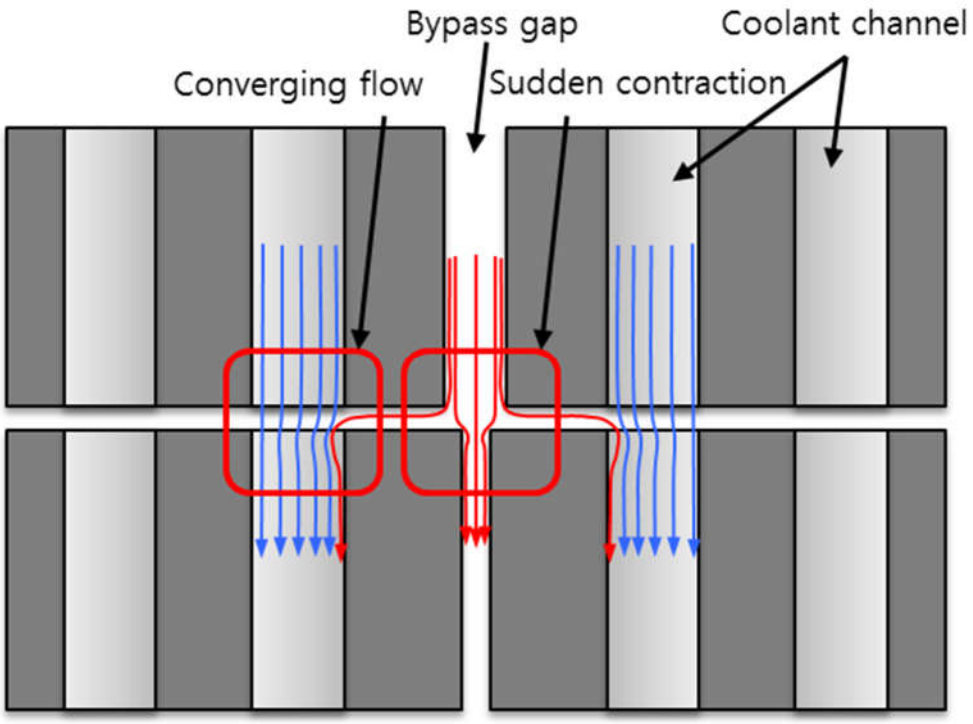

Figure 2.11 Pressure loss for sudden area change; sudden contraction at bypass gap and converging flow at the coolant channel

Chapter 3

Cross Flow Experiment

In the modeling, the cross flow is often considered as a leakage flow through the horizontal gap between stacked fuel blocks, which complicates the flow distribution in the reactor core by connecting the coolant channel and the bypass gap. On the other hand, the cross flow could lead to uneven coolant distribution and consequently cause superheating of individual fuel element zones with increased fission product release. Since the core cross flow has a negative impact on safety and efficiency of VHTR (INEEL, 2004), core cross flow phenomena have to be investigated to improve the core thermal margin of the VHTR. Although there have been some investigations on the core bypass and cross flow in the VHTRs, few studies have been conducted on the GT-MHR core. Especially, since the bypass and cross flow have very large geometrical dependency, the previous studies are not directly applicable to the GT-MHR core. Thus, the objectives of experimental study are to provide experimental data for the cross flow rate in the GT-MHR core, to evaluate the pressure loss coefficients of the cross flow, and, finally, to develop a correlation of cross flow loss coefficients for GT-MHR core. For this purpose, an experimental facility which has two stacked full-scale fuel blocks was constructed to represent the cross flow phenomena. Between the fuel blocks, two types of cross gap, the wedge-shaped gap and parallel gap, were simulated and cross flow was

induced and measured. After that, a commercial computational fluid dynamics code, ANSYS CFX was validated to confirm its applicability to the cross flow phenomena by comparing the experimental data of the cross flow rates with the predicted ones. From the validated CFD analysis results, the pressure loss coefficients for the cross gap were evaluated. In order to figure out the characteristics of loss coefficient, previous studies on cross flow were reviewed. Finally, based on previous studies and present work, a new correlation of the cross flow loss coefficient for GT-MHR core was proposed.

In the present study, the characteristics of cross flow were discussed with experimental and CFD results and then, the existing studies on cross flow were reviewed. Finally, the correlation for cross flow loss coefficient for GT-MHR core was obtained and the results were compared with well-known correlations, Groehn (1982), and Kaburaki (1990).

3.1 Review of Existing Studies on Cross Flow

In order to understand the cross flow loss coefficient, previous studies were reviewed in this section. There are two major experimental studies on cross flow loss coefficient. One is Groehn's experimental study in Germany and the other is Kaburaki's experimental and numerical study in Japan. In these two existing studies, the characteristics of cross flow were investigated and the correlations for the cross flow loss coefficient were developed. Even though, because of the geometrical difference, the correlations cannot be applied directly to GT-MHR of which fuel block type is targeted fuel block model, the experimental methodology and the approach became references of the present study.

3.1.1 Groehn's Experimental Study

Groehn (1982) studied the effect of cross flow on the main coolant flow at a two block test section. The cross flow was introduced through a wedge-shaped gap located between the two stacked fuel blocks. Air at ambient conditions was used as fluid. The full size fuel block models were used. Reynolds numbers in the coolant channel rages from 42,000 to 160,000, which are evaluated to be ranged between 0.77 and 2.91 kg/s in mass flow rate. The widths of the cross gap sizes were 1.85, 3.75, and 6 mm as presented in Fig. 3.1. From the experimental study, a correlation for cross flow loss coefficient was developed as

$$K_{Gr} = \left(\frac{A_{CG}}{A_{CH}} \right)^2 \left[3.58 \left(\frac{\delta}{D} \right)^{-2.3} \cdot 6.33 \left(\frac{A_{CG}}{\delta \cdot a} \right)^{-1.68} \right], \tag{3.1}$$

where A_{CG} and A_{CH} are the cross gap area and the coolant channel area, respectively and δ, D, and a are the cross gap size, the coolant diameter, and side length of the gap, respectively. The Groehn's correlation shows only the relationship between loss coefficient and geometrical information. It implies the flow rate doesn't affect the loss coefficient. However, since the experiment was conducted only turbulent region, it is hard to apply to laminar condition.

3.1.2 Kaburaki's Experimental and Numerical Study

Kaburaki (1990) conducted the experimental and numerical study on cross flow.

Two-block cross flow experiments were carried out and a numerical model were proposed to predict cross flow rate. The shapes of the fuel block, which were used in the experiment, are shown in Fig. 3.2. Parallel and wedge-shaped gaps were simulated. Air at room temperature and at atmospheric pressure was used as a working fluid. The width of the cross gap sizes range from 0.08 to 2.0 mm and the flow rate conditions cover the laminar region and turbulent region at the cross gap. Kaburaki found out the cross flow rate varies linearly with the pressure difference, ΔP, and the third power of the gap size, δ, in the low Reynolds number region, which is laminar flow region. From this relation, the dependence of the cross flow loss coefficient on the Reynolds number is expressed as,

$$K = \frac{A_{CG}^2 C_1}{\delta^2 \mathrm{Re}_{CG}} . \tag{3.2}$$

In the high Reynolds number region, most of the pressure drop is due to the contraction at the inlet of the cross flow path. Then the cross flow loss coefficient factor is described as,

$$K = \frac{A_{CG}^2 C_2}{\delta^2} \tag{3.3}$$

C_1 and C_2 are constants, which depend on the shape of the block interface. The cross flow loss coefficient, K, varies with the gap width, δ. From this study, the empirical correlation over the entire Reynolds number region was obtained as,

$$K_{Ka} = \left(\frac{A_{CG}}{\delta} \right)^2 \left(\frac{C_1}{\delta \mathrm{Re}_{CG}} + C_2 \right) \tag{3.4}$$

where A_{CG}, δ, and Re_{CG} are the cross gap area, the cross gap size, and Reynolds number at the cross gap respectively. C_1 and C_2 are the experimental constants determined by fitting Eq. (3.4) to the experimental data. The determined constants of the parallel gap for the type I, II, and III fuel blocks are summarized in Table 3.1. The Kaburaki's correlation includes the geometrical information and the flow information. It means the loss coefficient can be affected by the flow rate at the cross gap and the determined constants varies with the type of the fuel block. As aforementioned before, since the type of the fuel block and its geometry is different from that of GT-MHR, it cannot be applied directly to present study.

3.2 CFD Analysis and Assessment for Cross Flow Phenomena with Groehn's Experiments

3.2.1 Description of Groehn's Experimental Study

Groehn's study placed two blocks in the test section; one block on the upper side named as an upstream block and the other block on the lower side named as a downstream block. The main coolant flow passes through the test section from the upstream block to the downstream block during the experiment. Sizes of the open cross gap were designed to be adjusted between 1.85, 3.75, and 6 mm. The velocity distribution over the cross section of the fuel blocks and the pressure loss over the

gap were measured during the test. Groehn's study is a well-designed experiment, which can represent the multi-hole type prismatic core adopted by GT-MHR by allowing complicated cross flow phenomena in the VHTR core channels and gaps. The following sections will describe more details about the Groehn's experimental results by comparisons with the CFD predictions.

3.2.2 CFD Modeling

In order to analyze the Groehn's experiment, this study used CFX-12 (ANSYS Inc, 2009), which is a commercial CFD code. Figure 3.3 shows a computational domain and the mesh structure of gap width 6 mm case. In present simulation, GAMBIT 2.2.30 (Fluent Inc, 2004) was used for generating geometry and mesh grid. Four million nodes of hexahedra mesh were finally generated and fine mesh was adopted near the cross gap. Wall y+ value was approximately estimated to be 58. The working fluid was selected to be air at ambient temperature and atmospheric pressure. The Shear Stress Transport (SST) model of Menter (1994) with an automatic wall treatment based on the Reynolds Averaged Navier-Stokes (RANS) equation was adopted for turbulence modeling. The SST model is an eddy-viscosity model which combines the advantages of the k-ε model for the inner boundary layer and k-ω model for the outer region and outside of the boundary layer (Menter, 2003). According to the literatures, the SST model gives more accurate results than other eddy viscosity models with strong adverse pressure gradients and separation (BARDINA, 1997), which can be shown in the current study. In this study, 2^{nd} order upwind scheme was implemented for the convective terms. Residual for convergence criteria of iteration was set under 10^{-4} for mass, momentum, energy,

and turbulence variables. The calculation conditions were determined to be the same as the Groehn's experimental conditions as follows. Widths of the cross gaps were selected to be 1.85, 3.75, and 6 mm. Outlet flow rates were selected to be 0.4, 0.6, 0.8, 1.0, 1.2, and 1.6 kg/s which are evaluated to be $22{,}200 \leq Re_K \leq 88{,}600$ in Reynolds numbers. These conditions are summarized in Table 3.2.

3.2.3 CFD Analysis Results

- Effect of Cross Flow

In this session, the characteristics of the cross flow, especially effects of flow rate and gap size on cross flow, were investigated using CFD modeling. Figure 3.4 shows the velocity streamlines at the cross gap in radial direction at 1.0 kg/s in flow rate. This figure shows that as the cross gap width is increased, the cross flow penetrates more deeply. The average and maximum velocities of the flow in the cross gap are summarized for different gap sizes in Table 3.3. As shown in this table, variation of the velocities among the cases is not significant compared to that of the flow rates for different gap sizes shown in Table 3.4. In the flow rate of 1.0 kg/s cases, the maximum velocity and the average velocity in the cross gap are 70 m/s and 29 m/s for 6 mm gap size and the maximum velocity and the average velocity are 66 m/s and 25 m/s for 1.85 mm gap size. However, Table 3.4 does not show any noticeable difference in the ratio of cross flow to the main flow for different main flow rates. Furthermore, the ratio of gap size 3.75 mm to 6 mm is 0.625 and 1.85 mm to 6 mm is approximately 0.308 and that of cross flow rate is approximately 0.66 and 0.33, with standard deviation 0.001 and 0.007, respectively. Therefore, it gives us good insight that the cross flow rate is affected more by the size of cross

gap rather than the main flow rate.

The pressure contours at the cross gap in radial direction is plotted in Fig. 3.5. In the case of gap width 1.86 mm, the pressure distribution in the cross gap is almost uniform. However, as the cross gap size increased, the significant pressure difference occurs. In addition, for narrower cross gaps, pressures at the coolant channels are close to each other. But, for wider cross gaps, difference of pressures between the coolant channels is quite noticeable. Table 3.5 summarizes the calculated pressures at the coolant channels near the gap opening and closing in the cross gap for the flow rate of 1.0 kg/s. According to this table, the ratios of pressure difference are 25% for 6mm gap size and 13% for 1.85 mm gap size.

The velocity contours in axial direction is shown in Fig. 3.6. In the cross gap size 6 mm case, variation of the velocity is serious. The velocity difference of the coolant channels between the upstream and downstream blocks is also significant. This observation could be interpreted by relating the pressure contours in Fig. 3.5. In the small gap case, the pressure of the coolant channel at the cross flow is preserved. Hence, the velocity at the upstream block could be also preserved. On the other hand, when the gap is wide, pressure of the coolant channel at the cross flow is not preserved. As a result of this pressure loss, the velocity distribution at the upstream block could be uneven. Furthermore, velocity difference between upstream block and downstream block increases. This increase of the velocity difference could lead to an overheating of the fuel block. At the coolant channel near cross gap opening, flow separation occurs by the cross flow. This can induce a local overheating at the fuel block.

The flow velocity values in the coolant channel of the downstream block and upstream block are tabulated in Table 3.6. The values show that the downstream

block is not affected by cross flow. It means the amount of cross flow rate is equivalent to the amount of main coolant flow rate loss at the upstream block.

- Comparison with Experimental Results

In this section, the CFD simulation results are compared to the Groehn's experimental data. Fig. 3.7 shows the calculated velocity distribution at the upstream block and the downstream block under the cross flow for flow rate of 1.6 kg/s and for 6 mm gap size. As aforementioned, the downstream block is not affected by the cross flow. However, the cross flow reduces the main coolant flow of the upstream block. In Fig. 3.8, the CFD results were compared with Groehn's experimental results (Groehn, 1982). It shows the distribution of the velocity difference between upstream block and downstream block under cross flow for flow rate 1.6 kg/s and 6 mm gap size. The vertical axis of the graph indicates the dimensionless magnitude of the velocity difference between the upstream block and the downstream block. The CFD predicted the velocity difference at the coolant channel near the gap opening is 2.6 times more than averaged velocity difference. Near the gap opening, CFD results and experimental results show good agreements. However, at the inner coolant channel, the narrow flow path in the cross gap, CFD is likely to overestimate the velocity difference. At the narrow flow path, the roughness condition of the wall and the calculation error for turbulence-laminar transition could possibly explain the disagreements. At the narrow flow path, the wall effect to the flow is great, so the wall treatment should be treated carefully. However, since the wall roughness of the Groehn's experiment was not informed, the surface roughness condition in the CFD simulation was assumed to be the smooth wall. This assumption could also possibly be one of the reasons for the

disagreement. The turbulence modeling can be another reason of the error. As shown in Figs. 3.4 and 3.5, for pressure and velocity profile in the cross gap, the flow regime transited from turbulent to laminar. Therefore, it can be interpreted that the application of the turbulent model to the transitional flow regime, which is not valid for general turbulence models, can cause the calculation error. Hence, in future study, the sensitivity test for the turbulent models and numerical treatment to solve the transitional flow should be investigated.

Fig. 3.9 compares the results for the loss coefficient at the cross gap. The loss coefficient can be expressed as

$$K = \frac{\Delta P}{\frac{1}{2}\rho V_{KB}^2} \tag{3.5}$$

ΔP is the pressure drop between the atmosphere and downstream from the block. V_{KB} is the velocity due to cross flow only. Although CFD overestimate the flow in the small gap cases, the possible explanations are mentioned earlier, the overall values of loss coefficient are in good agreements with the experimental data. Hence, the ability of predicting the cross flow phenomena was confirmed to be quite reliable. Finally, validation of the CFD analysis was carried out in order to apply the CFD method to simulating the cross flow phenomena in the VHTR core.

3.3 Cross Flow Experiment for the Core of GT-MHR

The reference reactor of the test facility is GT-MHR (General Atomics, 1994),

under development by a group of Russian enterprises, General Atomics in USA, Framatome in France and Fuji Electric in Japan. GT-MHR is a helium cooled, graphite moderated reactor that adopted the prismatic fuel block type as a promising candidate reactor for hydrogen generation. The height and the flat-to-flat width of the standard fuel block are 793 mm and 360 mm, respectively, and it has 108 coolant holes, as depicted in Fig. 3.10.

The test facility simulates two full-scale stacked standard fuel blocks. A schematic diagram of the experimental apparatus, which consists mainly of inlet pipes, a test section with an upstream block and a downstream block, outlet pipes, and a blower, is presented in Fig. 3.11. The blower is installed at the lower end of the experimental apparatus, and the suction component of the blower is connected to the outlet pipe of the test section. The air flows into the test section from the top of the inlet pipes, which are long enough to fully develop the flow, and the cross flow is induced between the two blocks. The air then flows through the test section from the upstream block to the downstream block and discharges through the outlet pipes and the blower.

In the present study, two types of gaps—a wedge-shaped gap and a parallel gap—were examined by replacing the adjustable plate between the two fuel blocks. The types of gaps that were tested in this study are illustrated in Fig. 3.12. The sizes of the gaps, δ, were set to be 0.5, 1, 2, 4, and 6 mm. The maximum size of the gap was selected to be 6 mm base on the maximum gap size of the previous experimental studies (Groehn, 1982; Kaburaki and Takizuka, 1990), and the minimum size of the gap was selected to be 0.5 mm in consideration of the measurement and fabrication precision capabilities.

The working fluid used in the experiment is air at ambient pressure and

temperature. Because the coolant of the reference model is high-temperature and high-pressure helium, a scaling analysis was conducted to maintain the correspondence between the reference model and the test facility. In this study, the Reynolds number and Euler number in the coolant channel were preserved so that the dynamic similarity could be achieved. The conditions of the experiments were set to represent the normal operating conditions of GT-MHR core so as to preserve sufficient similarity. The main variables used for scaling analysis are summarized in Table 3.7.

The outlet flow rates are set to be between 0.1 and 1.35 kg/s, which are evaluated to maintain the Reynolds number at the coolant channel in the range from 4,000 to 54,000. Because the Reynolds number at the coolant channel under the normal operating condition of GT-MHR is known to be approximately 23,000, the test conditions sufficiently represent the normal operating condition of the reference model. The test matrix is summarized in Table 3.8, showing the series of experiments conducted for 355 test conditions, varying the shape and size of the gap and main flow rate.

In the experiment, the measured variables are the inlet mass flow rate of the upstream block, the outlet mass flow rate of the downstream block, the static pressures in the coolant channels, and the pressure distribution in the cross gap. The cross flow rate is evaluated from the difference between the measured inlet and outlet mass flow rate. The measuring instruments and the variables are listed in Table 3.9.

To measure the inlet and outlet mass flow rate, averaging Pitot tube flow meters are installed. Pressure transmitters are used to measure static pressures in the coolant channels and in the cross gap. The uncertainties of the measured variables

are summarized in Table 3.10.

To illustrate the cross flow phenomena, the absolute value of the cross flow rate and the ratio of the cross flow rate to the main flow rate are plotted in Fig. 3.6. The Cross flow Ratio (CR) of the cross flow rate to the main flow rate can be expressed as in Eq. (3.6).

$$CR = \frac{m_{cross}}{m_{main}} \tag{3.6}$$

Where m_{cross} is the mass flow rate of the cross flow and m_{main} is the main flow rate, referring to the outlet mass flow rate of the downstream block. The absolute value of the cross flow rate increases with an increasing main flow rate, as plotted in Figs. 3.13(a) and (b), and the CR maintains an almost constant value along the main flow rate, as seen in Figs. 3.13(c) and (d). On the other hand, the CR varies significantly with the gap size and the shape of the gap, and this implies that the crucial factors influencing the CR are the size and shape of the gap.

3.4 CFD Simulation of Cross Flow Experiment

Although the local data in the test section was measured, it was hard to analyze the flow characteristics around the cross gap because of the limitations of the measurement instrumentation. In order to determine the pressure loss coefficient, the required variables are the average velocity of the cross flow and the average value of the pressure difference between the outside of the cross gap and the inlet of the downstream block coolant holes. It was not possible to obtain accurate values of the pressure at the inlet of the downstream block coolant holes from the

experiment because of sudden contractions and vena contracta phenomena. Therefore, the present study validated the applicability of CFD analysis to the cross flow, as described in this section, and from the CFD analysis results, the pressure loss coefficient was obtained.

3.4.1 Kaburaki's Experimental and Numerical Study

Fig. 3.14 presents the computational domain and mesh structure of the experiment for the case of a wedge-shaped gap with a width of 6 mm. Approximately 9 million hexahedra mesh are used for the present simulation and the wall y+ value is approximately 20. The working fluid used in the simulation is set to be air at 25˚C, as in the experiment. Because the simulation is conducted without heat transfer, and the pressure drop through the two fuel blocks is under 5,000 Pa at the maximum flow rate condition, the properties of the fluid are set to be constant. CFD simulations are performed with a steady state incompressible Reynolds Averaged Navier-Stokes (RANS) equation. The maximum residual reduction for iteration convergence criteria is set to be under 10^{-5}. The Shear Stress Transport (SST) model from Menter (1994) with an automatic wall treatment was employed for the turbulence closure. Because it is highly possible that flow separation near the cross gap occurs because of the cross flow, the local flow separation should be predicted accurately. It is known that the SST model is an effective model for predicting various flow separations. Furthermore, the transitional Gamma-Theta model was used to obtain better results for the transitional turbulence (Langtry and Menter, 2005). Details of the simulation conditions are presented in Table 3.11.

In order to confirm the grid sensitivity of the present simulation, a grid convergence study is conducted, comparing four different grid cases for the case of the 6 mm wedge-shaped gap and using a 1 kg/s outlet flow rate condition. The number of cells and the compared variables of the flow rate at the cross gap and the pressure drops are listed in Table 3.12. The extrapolate solution, ϕ, is obtained using the Richardson Extrapolation method (Richardson, 1910; Richardson and Gaunt, 1927). From these grid sensitivity tests, that case of mesh 4 in Table 3.12 was selected for the calculation discussed below.

3.4.2 Results of the CFD Calculation Validation

In order to verify the prediction capability of the CFD code, the calculation results are compared with the experimental results, as shown in Fig. 3.15. The gap Reynolds number is defined as in Eq. (3.7).

$$\mathrm{Re}_{CG} = 4\frac{m_{cross}}{\mu P} \tag{3.7}$$

Where μ is the dynamic viscosity of the air, and P is the wetted perimeter, which is expressed by Eq. (3.8):

$$\begin{aligned} P_{wedge} &= 10a \\ P_{parallel} &= 12a \end{aligned} \tag{3.8}$$

Where a is the length of one edge of the hexagonal interface at the cross gap.

The CFD analysis data shows good agreement with the experimental data. In particular, the CR's decreasing trend for larger gap sizes and increasing trend for smaller gap sizes were observed as in the experiment. When the gap size is 6 mm, the CR decreases slightly as the main flow rate increases, whereas it increases when the gap size is 0.5 mm. As seen in Fig. 3.15, the range of the gap Reynolds number for each case is different. For the case of the 0.5 mm cross gap size, the gap Reynolds number is in a range under 3,000, representing a mainly laminar flow regime. On the other hand, when the gap size is 6.0 mm, the range of the gap Reynolds number is from 1,000 to over 20,000 in both wedge-shaped and parallel gap cases, representing a mainly turbulent flow regime. It can be understood that for fully laminar or turbulent regions, the cross flow phenomena show different characteristics, and the present CFD analysis reproduced the phenomena reasonably well. However, slight discrepancies are observed when the gap size is in the range between 1 and 2 mm. It is known that the accuracy of the CFD calculation at the transitional flow region is relatively lower than at fully laminar or turbulent regions, and the ranges of gap Reynolds number of the 1 and 2 mm cases are in the transitional flow region. Nevertheless, the disagreement between the CFD analysis and the experimental results is within 2% in terms of the absolute value of the CR, as plotted in Fig. 3.16. Considering that the uncertainty of the experimental data is 2.4% at the maximum flow rate condition, the discrepancies between the experiment and the CFD analysis can be considered acceptable. Therefore, it can be concluded that the CFD simulation results can be used to analyze the cross flow phenomena and pressure loss coefficient.

3.4.3 Pressure Loss Coefficient

In order to analyze the flow distribution of the prismatic VHTR core in a stochastic manner, a flow network code is a very useful tool. As aforementioned, the coolant channel and the bypass gap can be analyzed using equations that relate flow velocity to the head loss or pressure loss due to friction along a given length of channel. However, because of the geometrical complexity, it is hard to analyze the cross flow directly. In order to analyze the flow distribution of the prismatic VHTR core with flow network codes, an equation for the pressure loss coefficient is required that provides information on the relationship between flow rate and pressure difference.

The valid form loss coefficient is of crucial importance to ensure the bypass prediction capability of a flow network analysis code. In this study, the variables from the CFD analysis discussed above are used to obtain the pressure loss coefficient, K, defined as in Eq. (3.9).

$$K = \frac{\Delta P}{\frac{1}{2}\rho V^2} \tag{3.9}$$

where ΔP is the pressure drop between the outside of the cross gap and the inlet of the downstream fuel block at the cross gap, and V is the average velocity of the cross flow at the cross gap opening. The average value of pressures over the entire length of all coolant channels and the mean velocity of the cross flow at the cross gap opening are used to obtain the loss coefficients.

The trend of the cross gap loss coefficients follows general friction factors such

as the Darcy friction factor or that from the Moody chart (Moody, 1994). When the Reynolds number is low, the loss coefficient shows an inversely proportional relation with the Reynolds number, but it becomes almost constant when the Reynolds number is sufficiently high, as presented in Fig. 3.17. The trend of CR can be interpreted using these characteristics. Because the loss coefficient decreases with increases in the gap Reynolds number in the low Reynolds number region, the CR could increase, as seen in the graphs of the 0.5 mm gap size shown in Fig. 3.15.

3.5 Correlation of Cross Flow Loss Coefficient for GT-MHR Core

When viewed in light of Kaburaki's study and the present work on cross flow for the core of GT-MHR, the correlation should include not only the geometrical information but also the flow information, which implies that Groehn's correlation would be inaccurate in the low Reynolds number region. For this reason, the Kaburaki's correlation form is selected as the reference correlation for the cross flow loss coefficient of the core of GT-MHR. In this study, however, the configuration of the fuel block is identical with the prototype, and the geometry factor A_{CG} over δ in Eq. (3.4) has a constant value. Therefore, the factor can be included in the determined constants, C_1 and C_2, and a new correlation form for the core of GT-MHR fuel block geometry can be suggested, represented by Eq. (3.10).

$$K_{PMR200} = \frac{C_1}{\delta \mathrm{Re}_{CG}} + C_2 \tag{3.10}$$

In order to determine specific constant values, C_1 and C_2, for PMR200, the pressure loss coefficient is plotted as a function of δRe in Fig. 3.18, confirming that the experimental data in the low Reynolds number region converged on a line comparing to the graphs shown in Fig. 3.17. From these results, the constant values for the core of GT-MHR can be obtained; C_1: 0.63 and C_2: 3.5.

In order to confirm the suitability of the correlation, it is compared with Groehn's correlation and Kaburaki's correlation. As shown in Fig. 3.18, the loss coefficient from Groehn's correlation is constant at each gap size and the larger gap size has a smaller loss coefficient value. However, because of the geometrical difference between Groehn's fuel block model and that of GT-MHR, the loss coefficient from Groehn's correlation shows lower values even in the high Reynolds number region. Moreover, as aforementioned, because there is no flow information in the correlation, the results show significant difference in the low Reynolds number region. In Kaburaki's correlation, because the shape of the fuel block Type III is the most similar with that of the PMR200 fuel block, the determined constants, C_1 and C_2, for Type III in Table 3.1 are selected to compare the results. Kaburaki's correlation shows tendencies similar to the correlation proposed here; however, there are slight differences in the turbulent region and significant over-estimation in the laminar region, perhaps caused by the geometrical differences between Kaburaki's fuel block configuration and that of GT-MHR. Although Kaburaki's fuel block model has a larger diameter and a smaller number of coolant channels (Kaburaki's model: 33 coolant channels / 42 mm of diameter; PMR200: 108 coolant channels / 16 mm of diameter), it has an annular shape because of a fuel pin placed in the center of the channel, and thus the total flow area in Kaburaki's fuel block is smaller than that of PMR200 (Kaburaki's model: 0.0158 m^2; PMR200: 0.0217 m^2).

The annular shape and the total area of the coolant channel might increase the loss coefficient in the low Reynolds number region. Therefore, it can be concluded that the accuracy of the new correlation is an improvement on Kaburaki's correlation not only in the turbulent region but also in the laminar region, as shown in Figs. 3.18 and 3.19.

In this experimental study, in order to investigate the cross flow phenomena in the core of GT-MHR, a series of experiments was analyzed. Two different types of cross gaps—a wedge-shaped gap and a parallel gap—were used for the experiments and the cross flow rates were measured for varying gap sizes and flow rates. In addition, the experimental results were compared with CFD analysis and the prediction capability of the CFD code was confirmed. From the CFD analysis results, the loss coefficient for GT-MHR was obtained. Finally, in order to obtain the correlation of cross flow loss coefficient for GT-MHR, existing studies on cross flow were reviewed, a new correlation was obtained, and the new correlation was compared with existing correlations from Groehn (1982) and Kaburaki (1990).

Conclusions from this study can be summarized as follows:

- The cross flow experimental data were reproduced by CFD analyses of both the wedge-shaped gap and parallel gap.
- The results of the CFD analysis and the experimental data were in good agreement.
- The pressure loss coefficient for the cross gap between the fuel blocks of PMR200 was obtained. The loss coefficient is nearly constant in the high Reynolds number region, whereas it varies with the gap size in the low Reynolds number region.
- A new correlation of the cross flow loss coefficient for GT-MHR was

proposed, and it shows improved results for a wide range of Reynolds numbers, compared with existing correlations.

Table 3.1 Empirically determined constants, C_1 and C_2, in Eq. (3.4)

	Parallel gap		Wedge-shaped gap	
	C_1	C_2	C_1	C_2
Type I	0.67	3.13	2.144	12.52
Type II	0.90	2.0	2.7	8
Type III	0.78	1.7	2.418	6.8

Table 3.2 Conditions of CFD modeling

y+	58
Turbulence model	SST based on RANS
Convective terms	2^{nd} order upwind scheme
Residual of iteration	Under 10^{-4}
Cross gap size (mm)	1.85, 3.75 and 6
Outlet flow (kg/s)	0.4, 0.6, 0.8, 1.0, 1.2 and 1.6

Table 3.3 Average velocity and maximum velocity in the cross gap (flow rate 1.0 kg/s)

Gap size (mm)	Average velocity (m/s)	Maximum velocity (m/s)
6 mm	29 m/s	70 m/s
3.75 mm	28 m/s	69 m/s
1.85 mm	25 m/s	66 m/s

Table 3.4 Cross flow rate

Case	Cross gap 6 mm		Cross gap 3.75 mm		Cross gap 1.85 mm	
Main flow rate (kg/s)	Cross flow rate (kg/s)	Main flow to cross flow ratio	Cross flow rate (kg/s)	Main flow to cross flow ratio	Cross flow rate (kg/s)	Main flow to cross flow ratio
0.4	0.06657	0.166425	0.043898	0.109745	0.021703	0.054258
0.6	0.098474	0.164123	0.065032	0.108387	0.032373	0.053955
0.8	0.130105	0.162631	0.085979	0.107474	0.042948	0.053685
1	0.161549	0.161549	0.106803	0.106803	0.053463	0.053463
1.2	0.19286	0.160717	0.12753	0.106275	0.06394	0.053283
1.4	0.22406	0.160043	0.14819	0.10585	0.07438	0.053129
1.6	0.25518	0.159488	0.16878	0.105488	0.0848	0.053

Table 3.5 Pressure values at the coolant channels in cross gap
(flow rate 1.0 kg/s case)

	6 mm	3.75 mm	1.85 mm
Pressure at the coolant channel near gap opening	-2636.5 Pa	-2855.71 Pa	-3108.93 Pa
Pressure at the coolant channel near gap closing	-3512.94 Pa	-3559.51 Pa	-3567.34 Pa

Table 3.6 Flow velocity at the coolant channel of upstream block and downstream block

Flow rate (kg/s)	Block	Velocity (m/s)		
		Gap 6 mm	Gap 3.75 mm	Gap 1.85 mm
0.4	Upstream	15.3847	16.4308	17.455
	Downstream	18.4596	18.4593	18.4592
0.6	Upstream	23.1413	24.6844	26.1913
	Downstream	27.6894	27.689	27.6889
0.8	Upstream	30.9105	32.9465	34.932
	Downstream	36.9193	36.9187	36.9186
1	Upstream	38.6883	41.2142	43.6755
	Downstream	46.1491	46.1484	46.1482
1.2	Upstream	46.4723	49.4864	52.4208
	Downstream	55.379	55.3781	55.3779
1.4	Upstream	54.2612	57.7619	61.1676
	Downstream	64.6089	64.6078	64.6076
1.6	Upstream	62.0541	66.04	69.9155
	Downstream	73.8388	73.8375	73.8373

Table 3.7 Main variables for scaling analysis

	PMR200 normal operation	Experiment	Degree of similitude
Working fluid	Helium at 7 MPa	Air at ambient pressure	-
Density (kg/m^3)	3.868	1.185	0.31
Viscosity (Pa·s)	4.111×10^{-5}	1.841×10^{-5}	0.45
Mass flow rate (kg/s)	1.192	0.565	0.47
Velocity (m/s)	15.26	22.3	1.46
Pressure drop in one fuel block (Pa)	578.6	378.7	0.65
Reynolds number	22793	22795	1
Friction factor	0.02572	0.02572	1
Euler number	0.6423	0.6423	1

Table 3.8 Test matrix

Gap Shape	Gap width (mm)	Flow rate (kg/s)	Number of test cases	Temperature (℃)
Wedge	0.5	0.1 – 1.35	35	19
	1.0	0.1 – 1.35	35	18
	2.0	0.1 – 1.35	43	17
	4.0	0.1 – 1.35	35	16
	6.0	0.1 – 1.35	32	18
	Total		180	
Parallel	0.5	0.1 – 1.35	35	20
	1.0	0.1 – 1.35	35	21
	2.0	0.1 – 1.35	35	22
	4.0	0.1 – 1.35	35	23
	6.0	0.1 – 1.35	35	22
	Total		175	

Table 3.9 Measuring instruments

Variable	Measuring instrument	Error
Flow rates	FCO68 / Furness Controls	0.1% of reading
Pressure transmitters for flow rate	Rosemount 3051 / Rosemount	0.04% of span
Static pressures	VPRN-A2-(5- -10)KPa-4C / Valcom	0.1% of reading

Table 3.10 Uncertainties of the measured variables

Variable	Uncertainty	
	Min. flow rate condition (m_{main} = 0.1 kg)	Max. flow rate condition (m_{main} = 1.35 kg)
ΔP	2.01 Pa (20.1%)	43.2 Pa (2.51%)
P	0.16%	0.16%
T	0.75%	0.75%
m_{main}	0.01 kg/s (10%)	0.023 kg/s (1.67%)
m_{cross}	0.014 kg/s (14% of m_{main})	0.032 kg/s (2.4% of m_{main})
CR (Cross flow Ratio)	17.5%	2.90%

Table 3.11 CFD simulation conditions

Mesh	9 million hexahedra
y^+	20
Working fluid	Air at 25˚C
Maximum residual	Under 10^{-5}
Turbulence closure.	SST with an automatic wall treatment
Transitional turbulence	Transitional Gamma-Theta model
Turbulence numeric	High resolution scheme
Entrance of the upstream block and Cross gap between two blocks	Opening boundary condition Mass and Momentum – Opening Pres. And Dirn with a Relative Pressure of 0 Pa
Outlet of the downstream block	Mass flow rate boundary condition
Wall	Wall boundary condition No slip wall and smooth wall

Table 3.12 Grid convergence test results

Case	Total number of elements	Flow rate at the cross gap [kg/s]	Error of cross flow rate	Pressure drop at the outlet [Pa]	Error of pressure drop
Mesh 1	806,945	0.161357	6.09 %	4202.3	9.18 %
Mesh 2	1,772,025	0.157865	3.79 %	3954.3	2.73 %
Mesh 3	3,983,165	0.153901	1.18 %	3906.5	1.45 %
Mesh 4	8,761,490	0.152674	0.38 %	3872.5	0.61 %
Richardson solution, ϕ	-	0.1521	-	3849.1	-

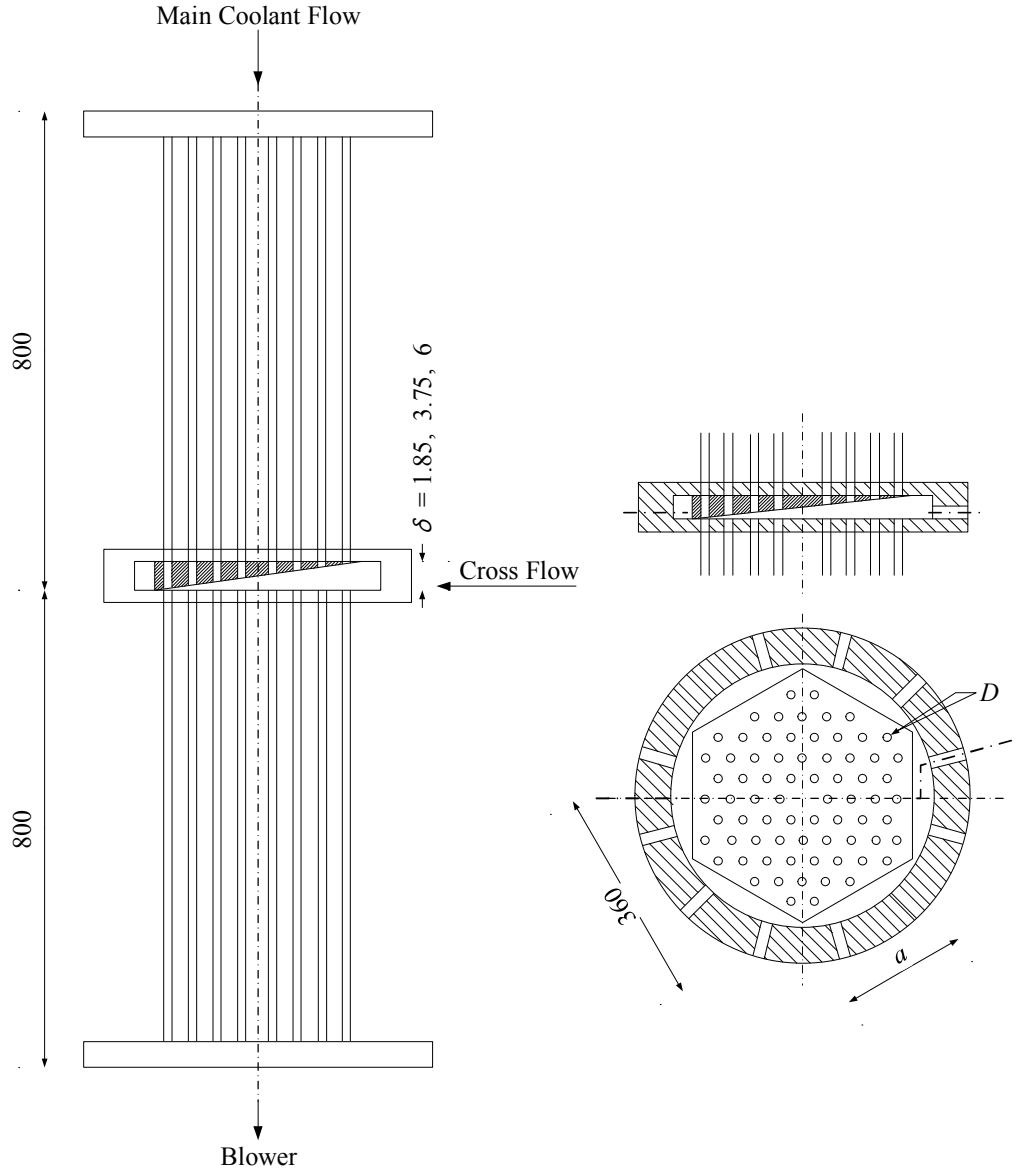

Figure 3.1 Groehn's experimental setup (Groehn, 1982)

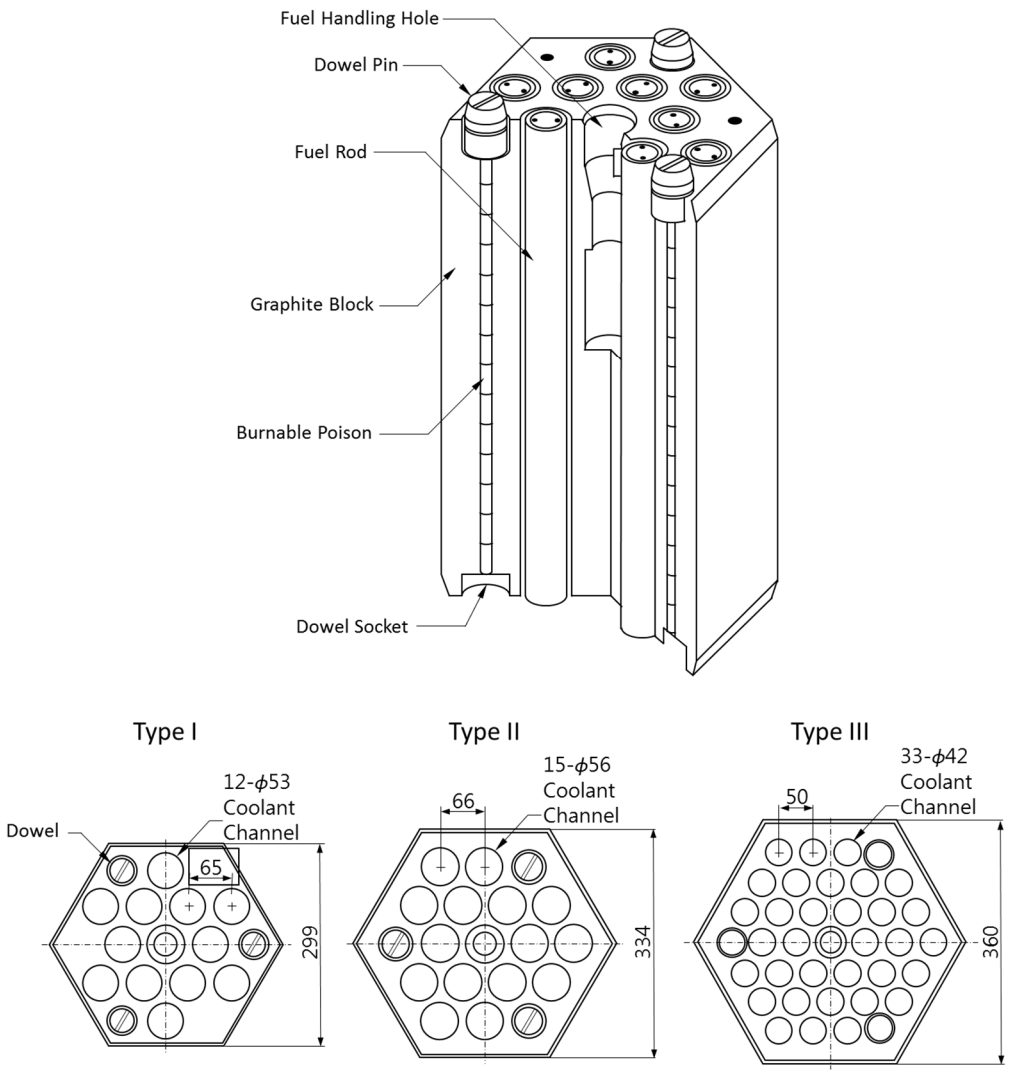

Figure 3.2 Fuel block model of Kaburaki's study (Kaburaki, 1990)

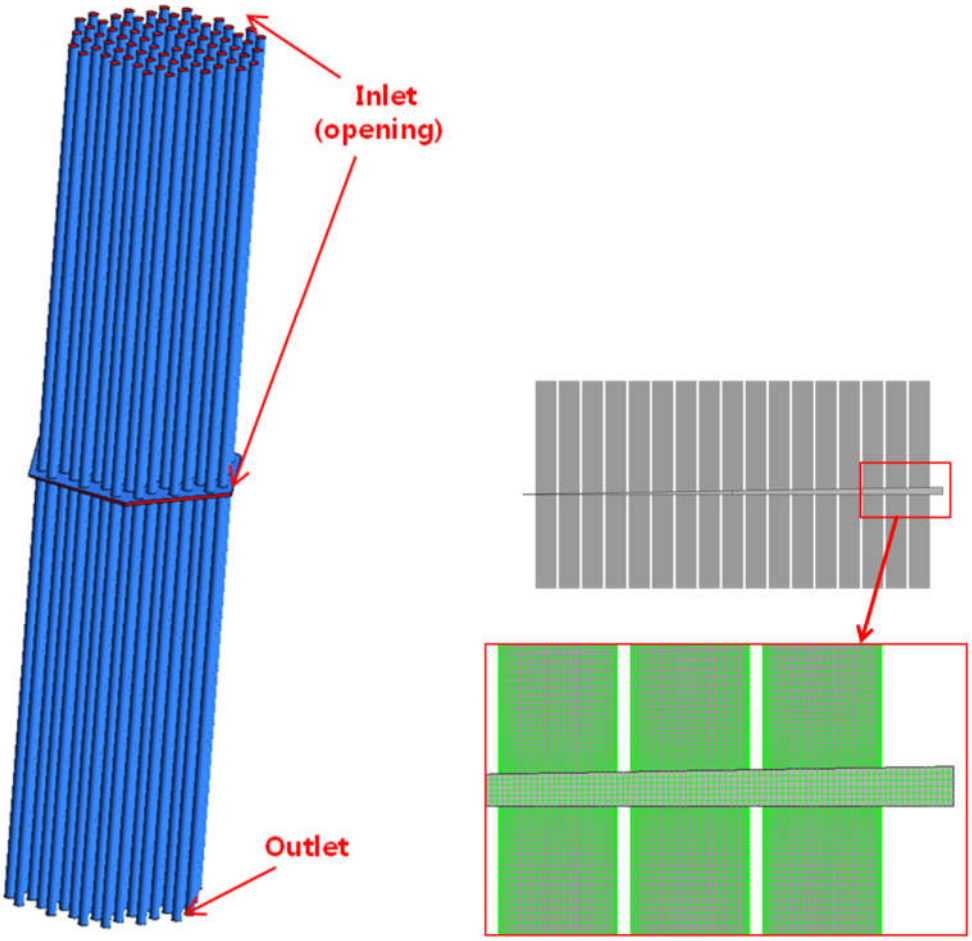

Figure 3.3 Computational domain and mesh structure of cross gap (gap size 6 mm case)

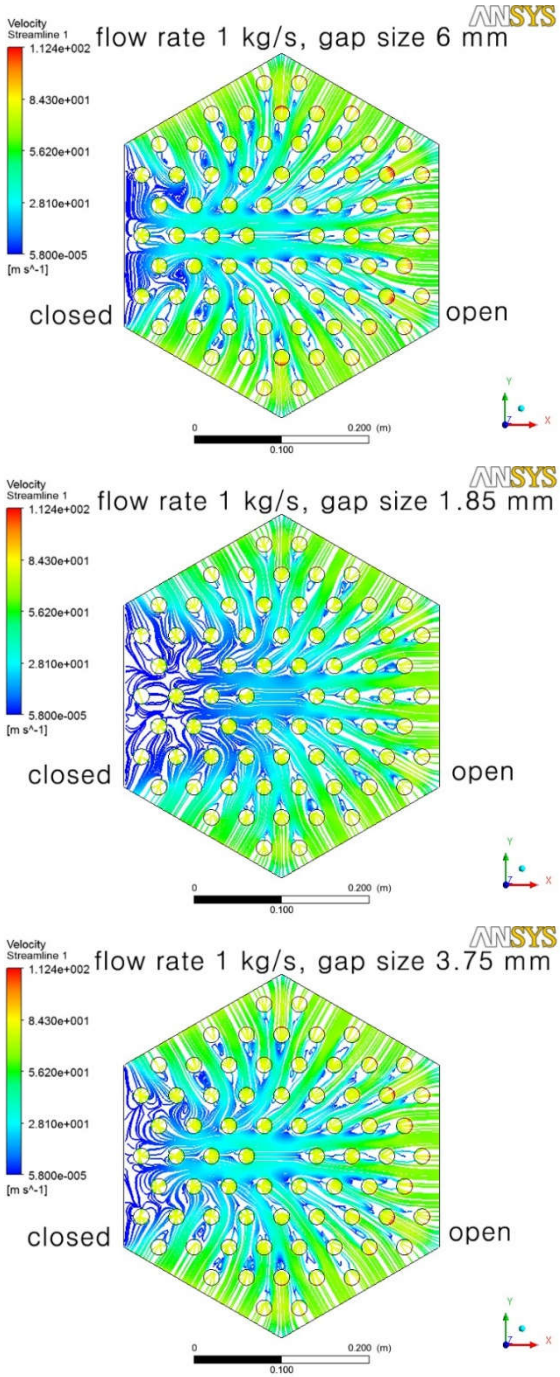

Figure 3.4 Velocity streamlines at the cross gap in radial direction (flow rate 1 kg/s and cross gap widths 1.85, 3.75 and 6 mm in sequence order)

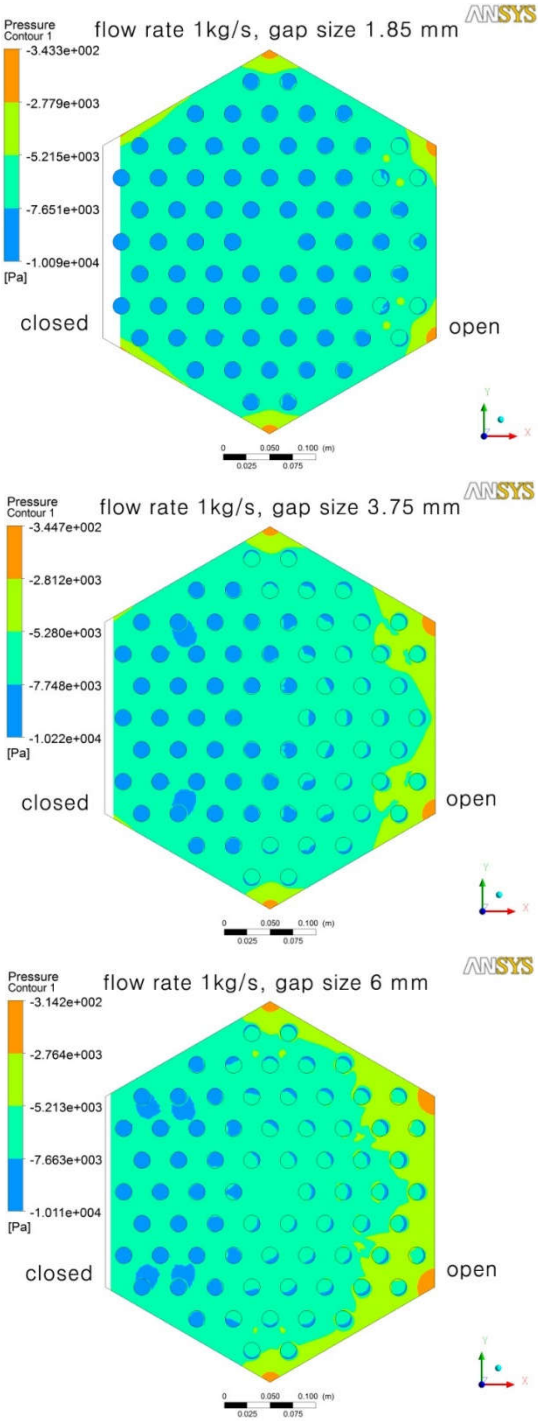

Figure 3.5 Pressure contours at the cross gap in radial direction (flow rate 1 kg/s and cross gap widths 1.85, 3.75, and 6 mm in sequence order)

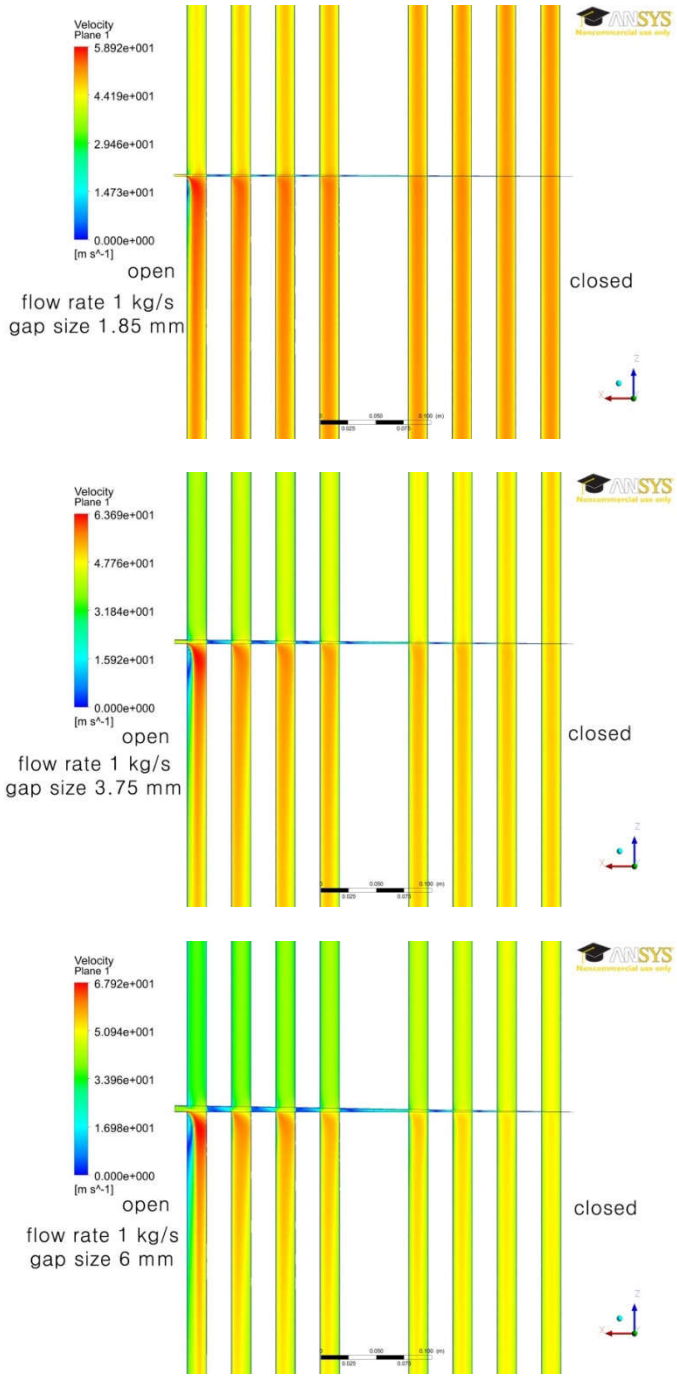

Figure 3.6 Velocity contours in axial direction
(flow rate 1.0 kg/s and cross gap widths 1.85, 3.75, and 6 mm in sequence order)

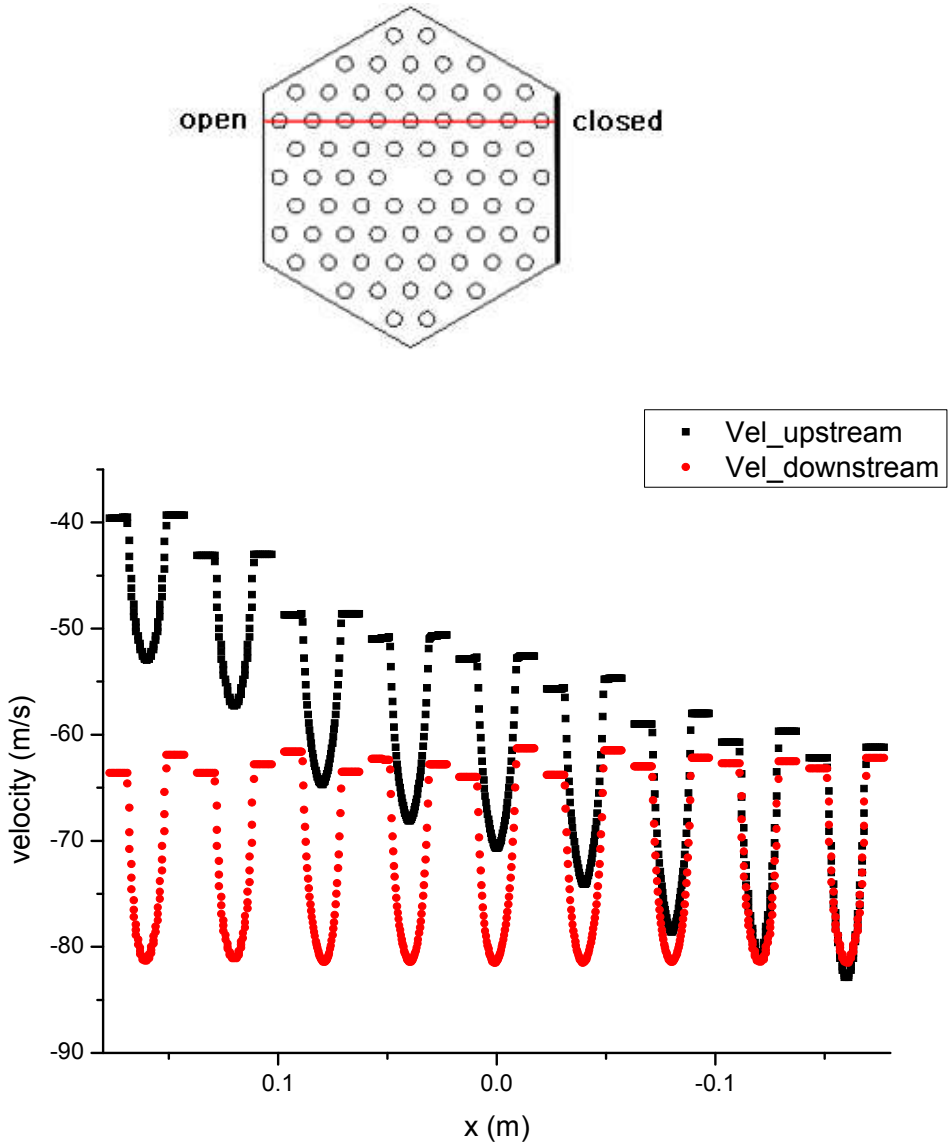

Figure 3.7 Flow velocity distribution under cross flow (flow rate 1.6 kg/s and for cross gap 6 mm)

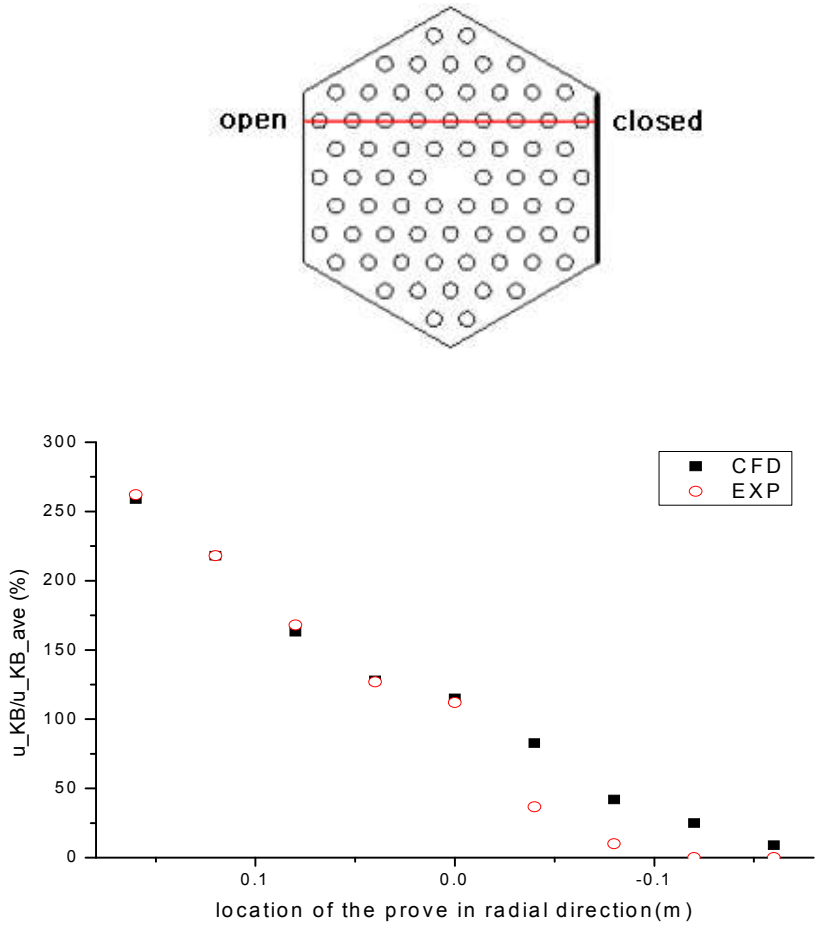

Figure 3.8 Distribution of velocity difference between upstream block and downstream block under cross flow (flow rate 1.6 kg/s and for cross gap 6 mm)

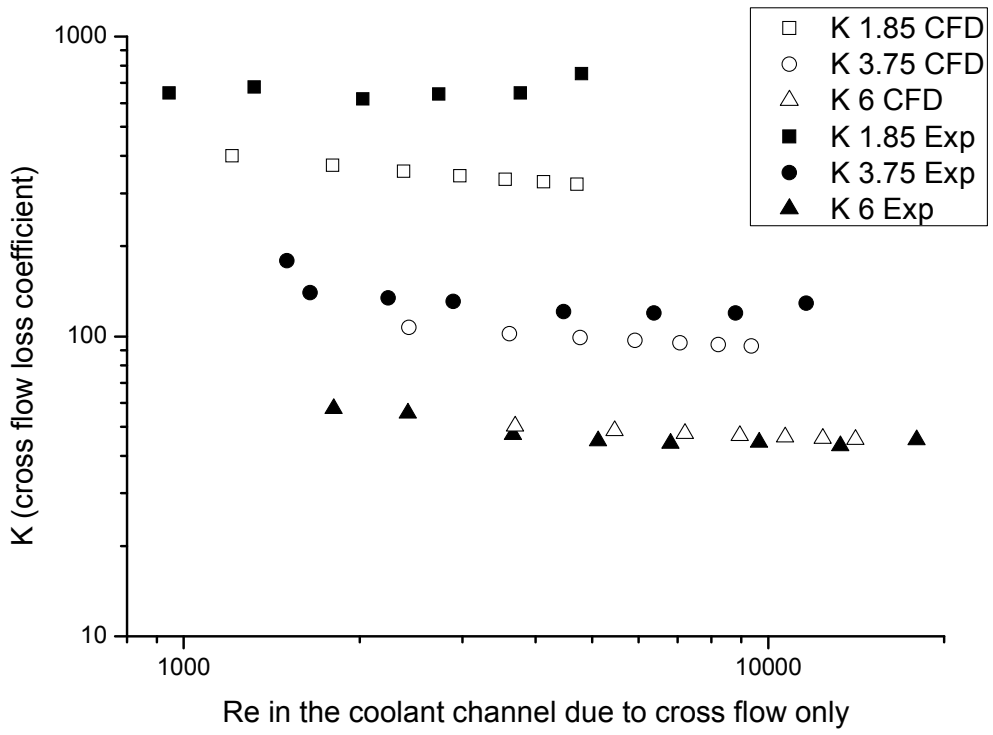

Figure 3.9 Flow loss coefficient at the cross gap

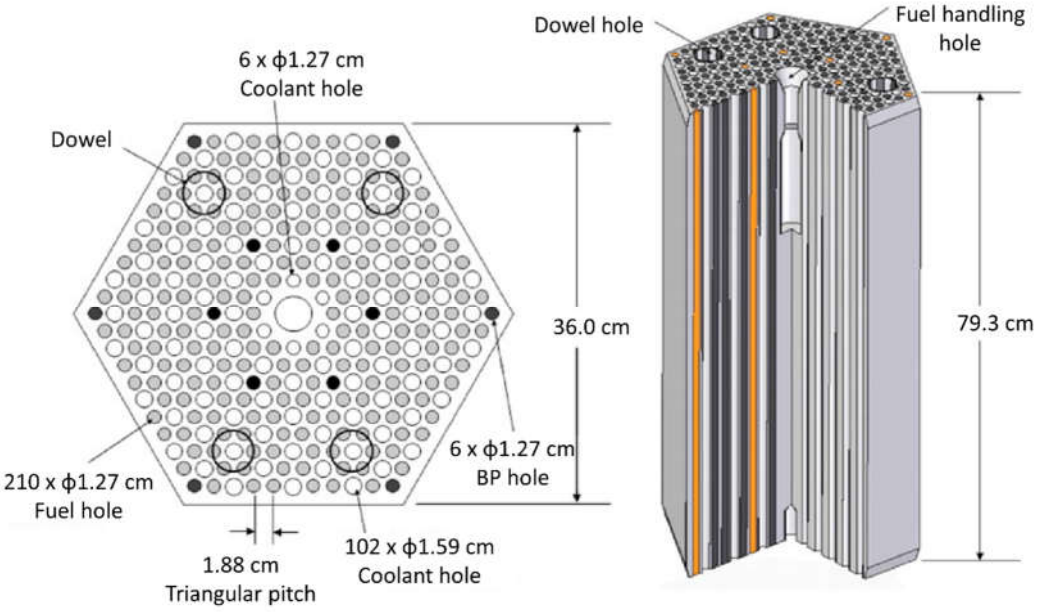

Figure 3.10 Standard fuel block of PMR200

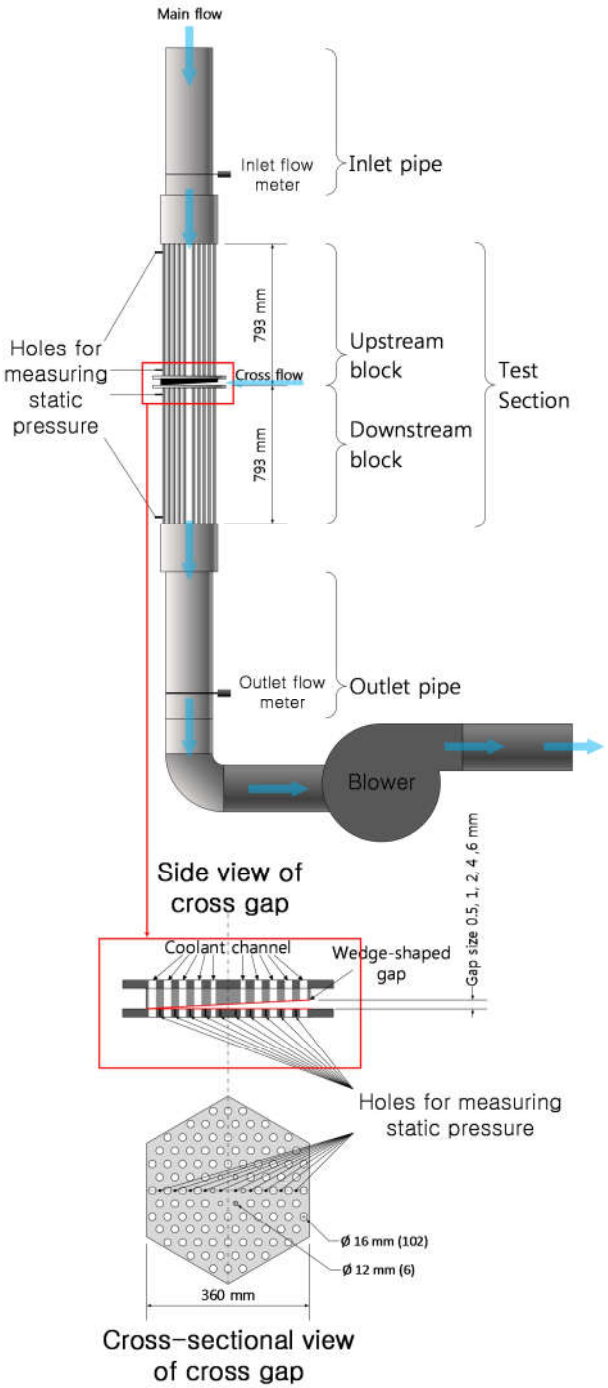

Figure 3.11 Standard fuel block of PMR200

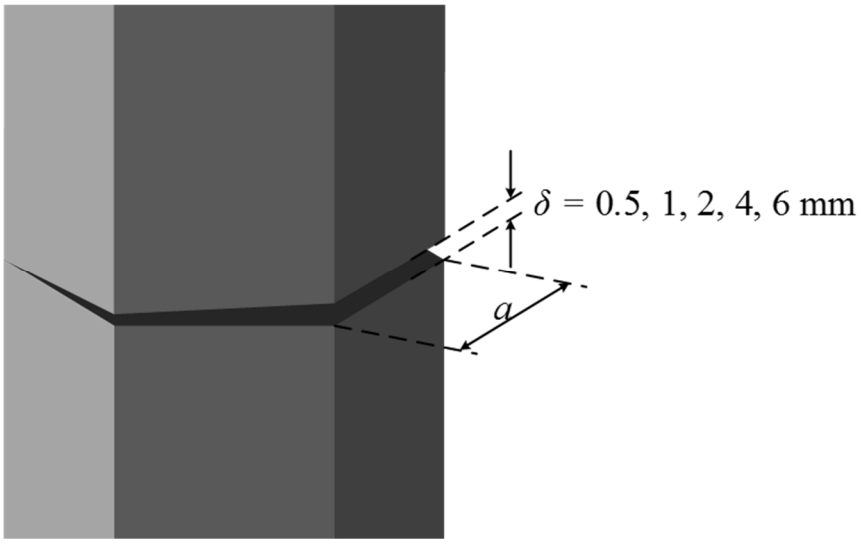

(a) Wedge-shaped gap

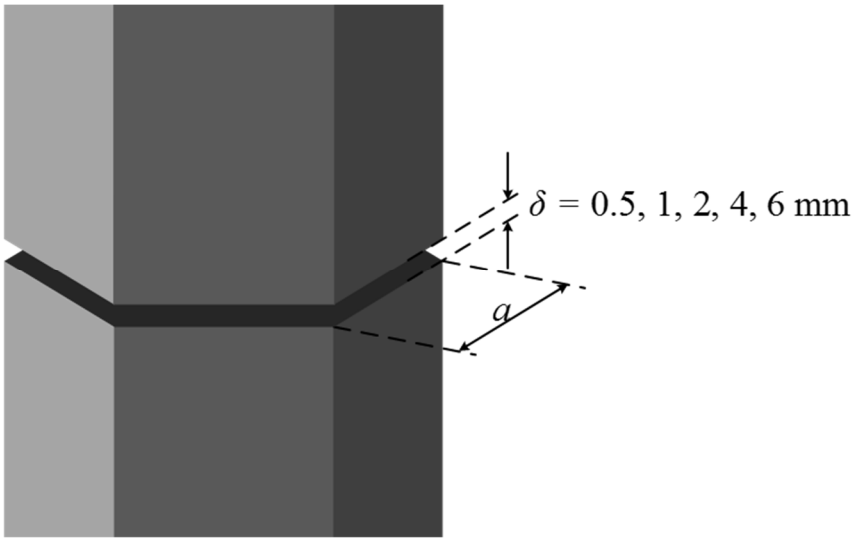

(b) Parallel gap

Figure 3.12 Standard fuel block of PMR200

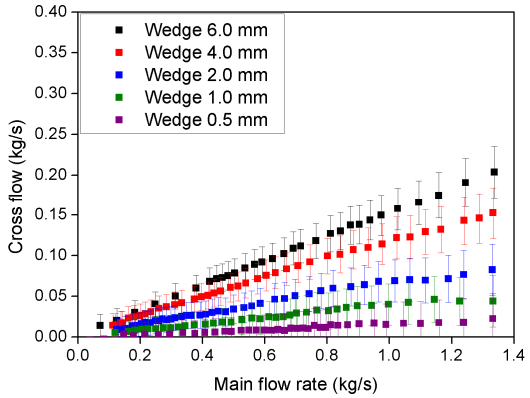

(a) Wedge

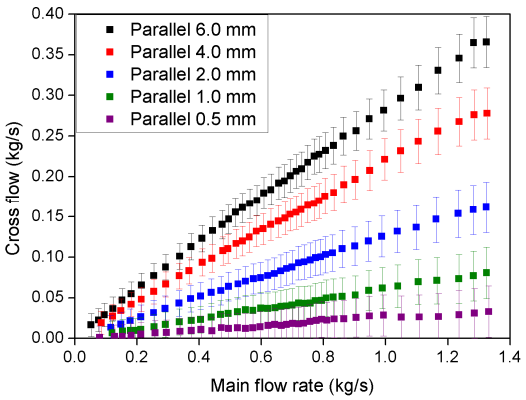

(b) Parallel

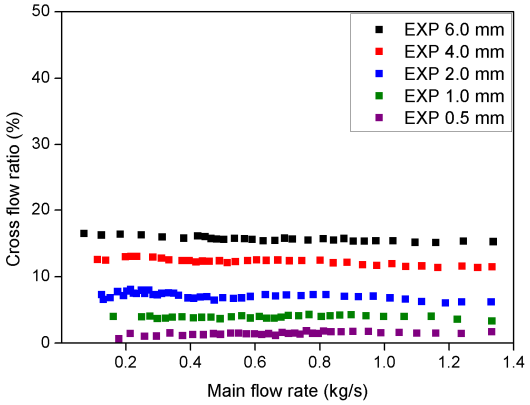

(a) Wedge

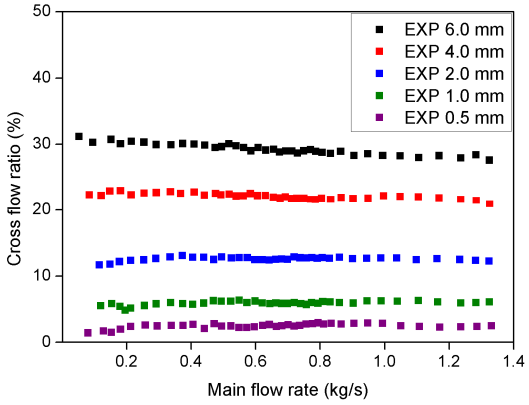

(b) Parallel

Figure 3.13 The cross flow rate and the cross flow ratio to the main flow rate

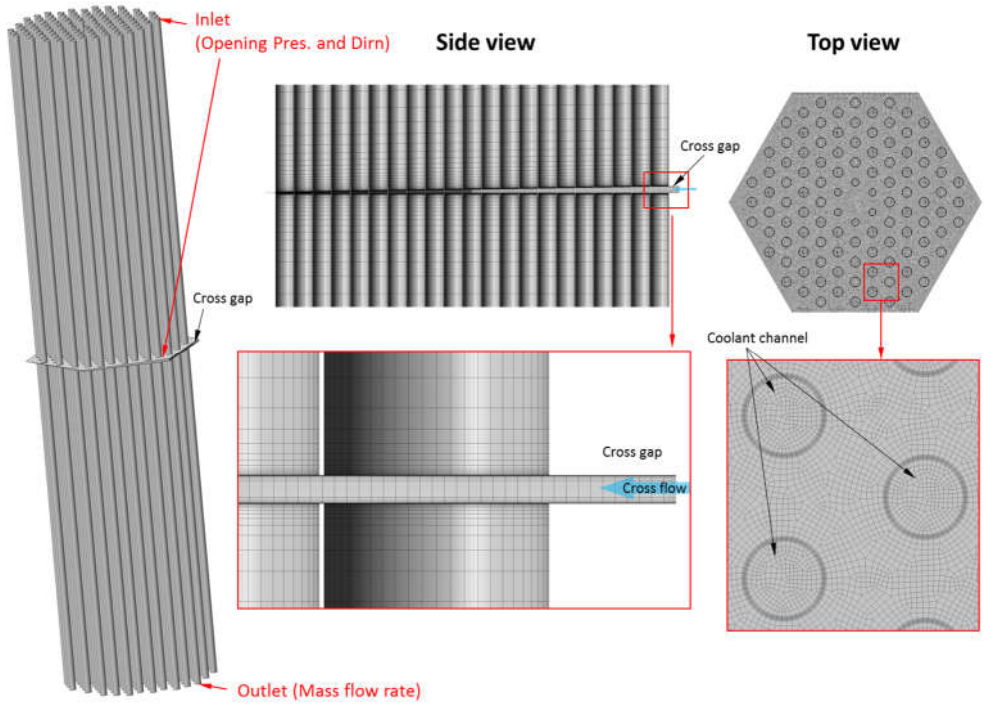

Figure 3.14 Computational domain and mesh structure

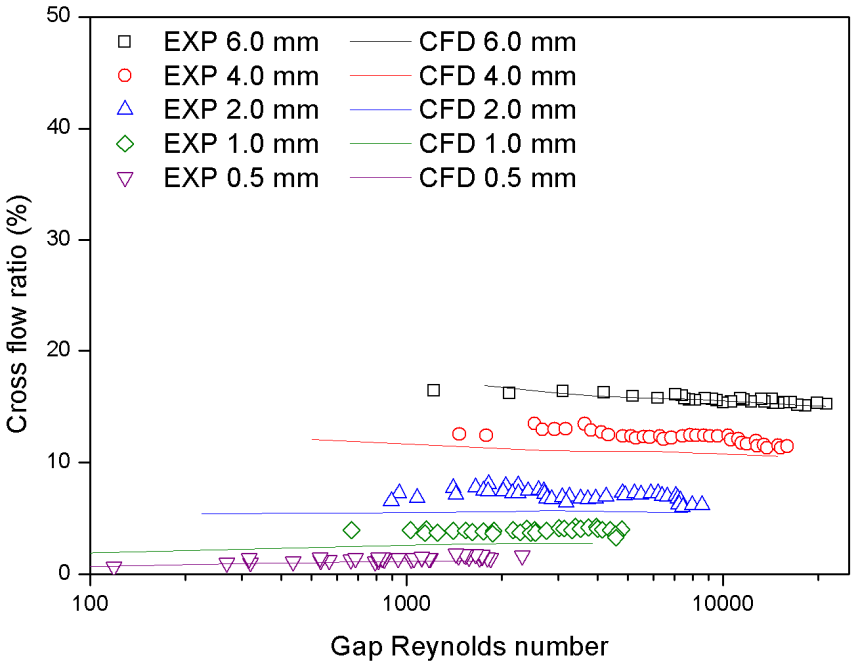

(a) Wedge-shaped gap

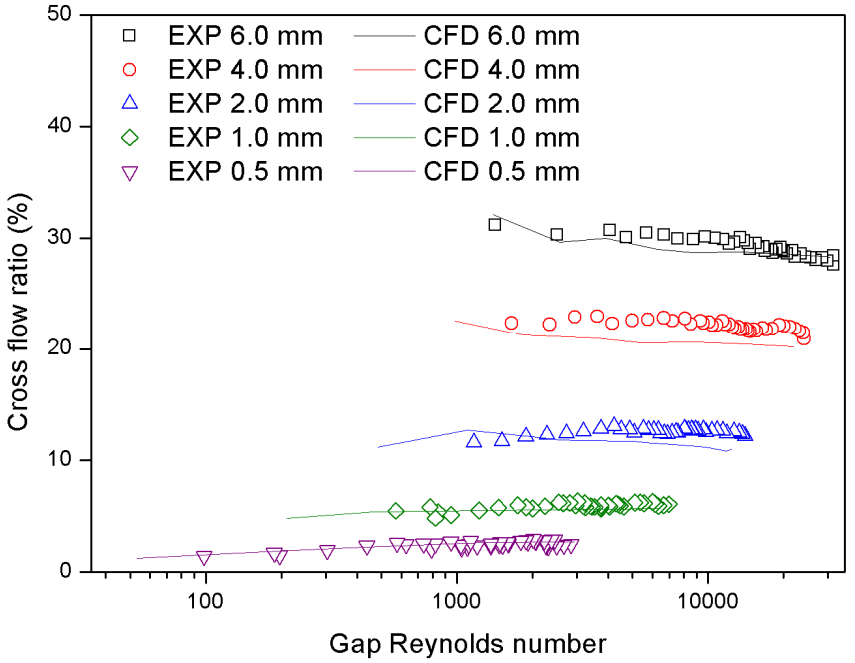

(b) Parallel gap

Figure 3.15 Comparison results for whole cases

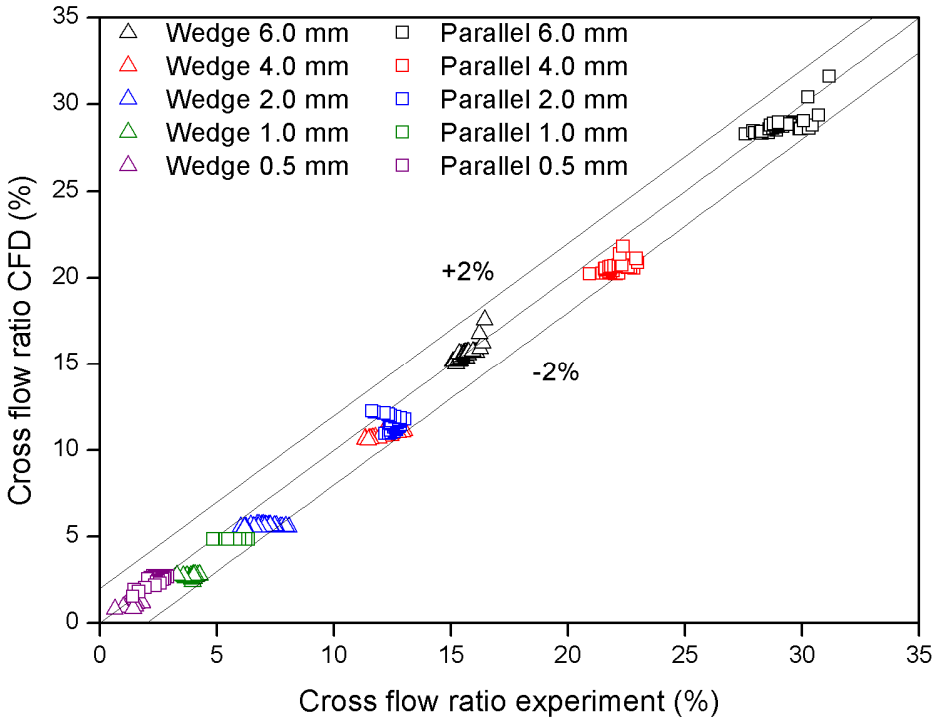

Figure 3.16 Comparison of the CFD prediction and experiments for whole cases

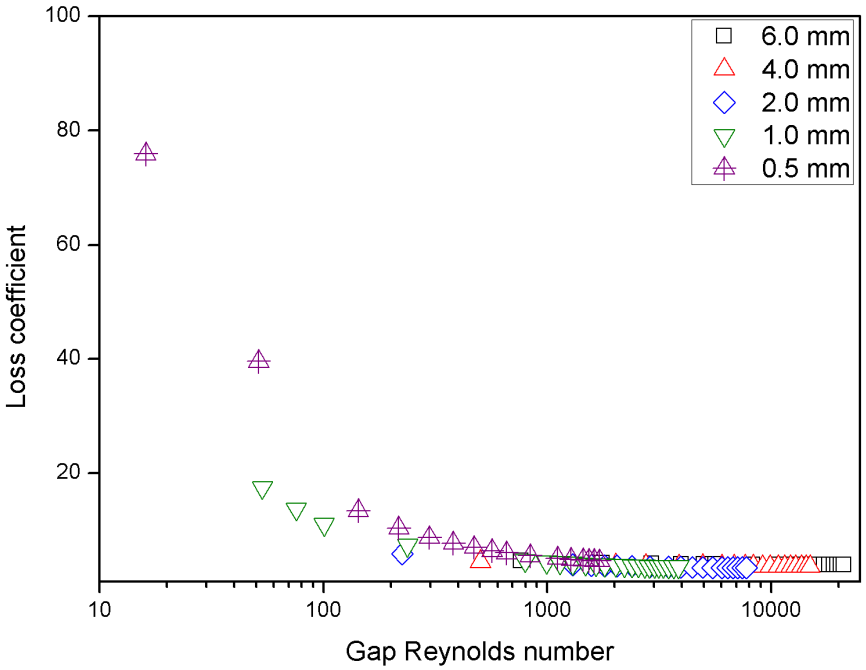

(a) Wedge-shaped gap

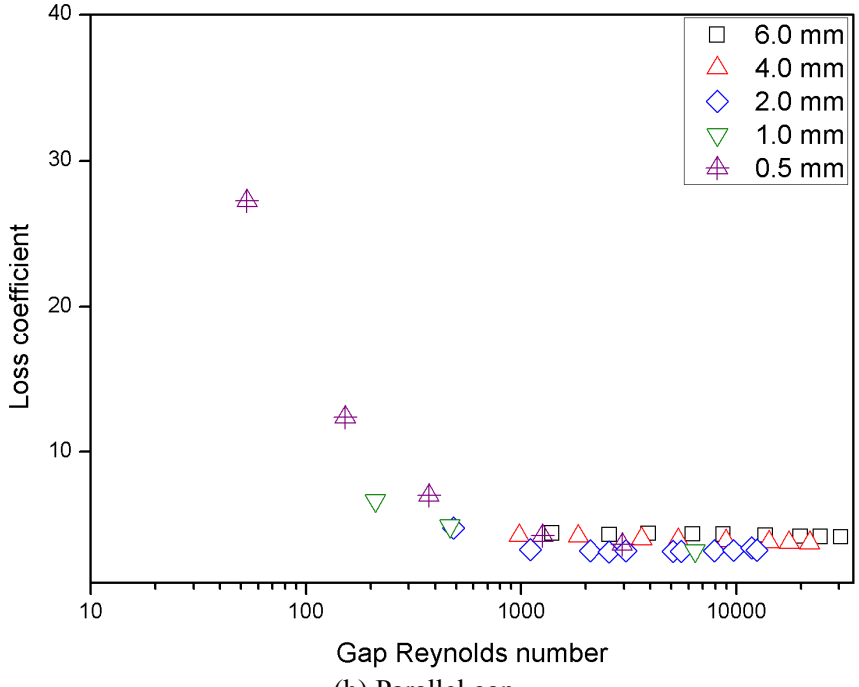

(b) Parallel gap

Figure 3.17 Pressure loss coefficient at the cross gap

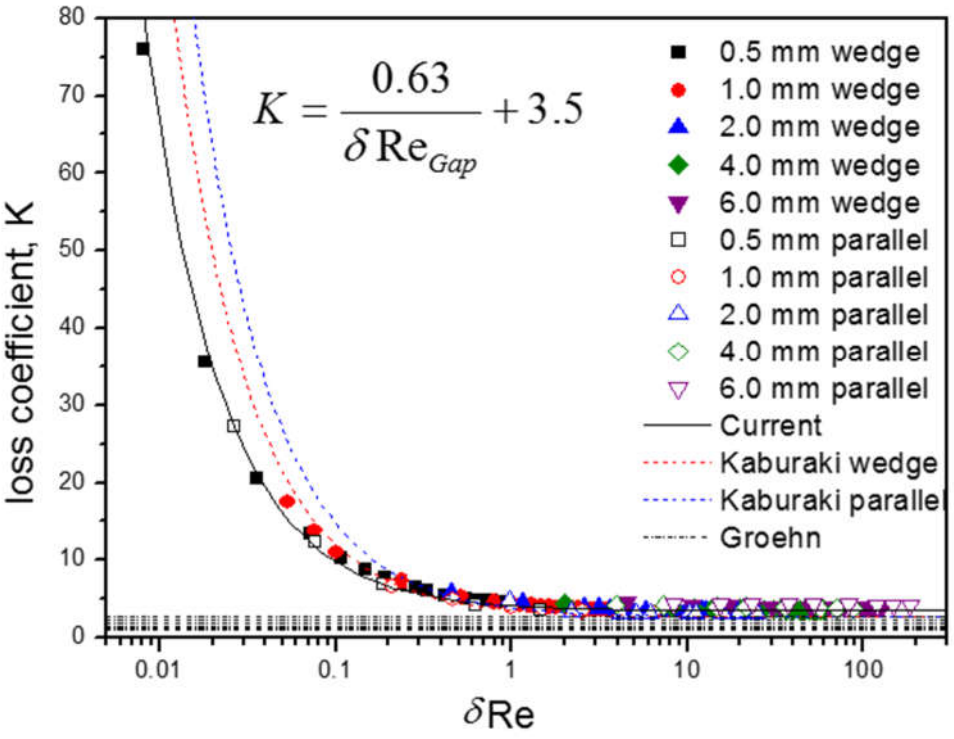

Figure 3.18 Comparison results of the loss coefficient correlations with the experimental data for whole cases

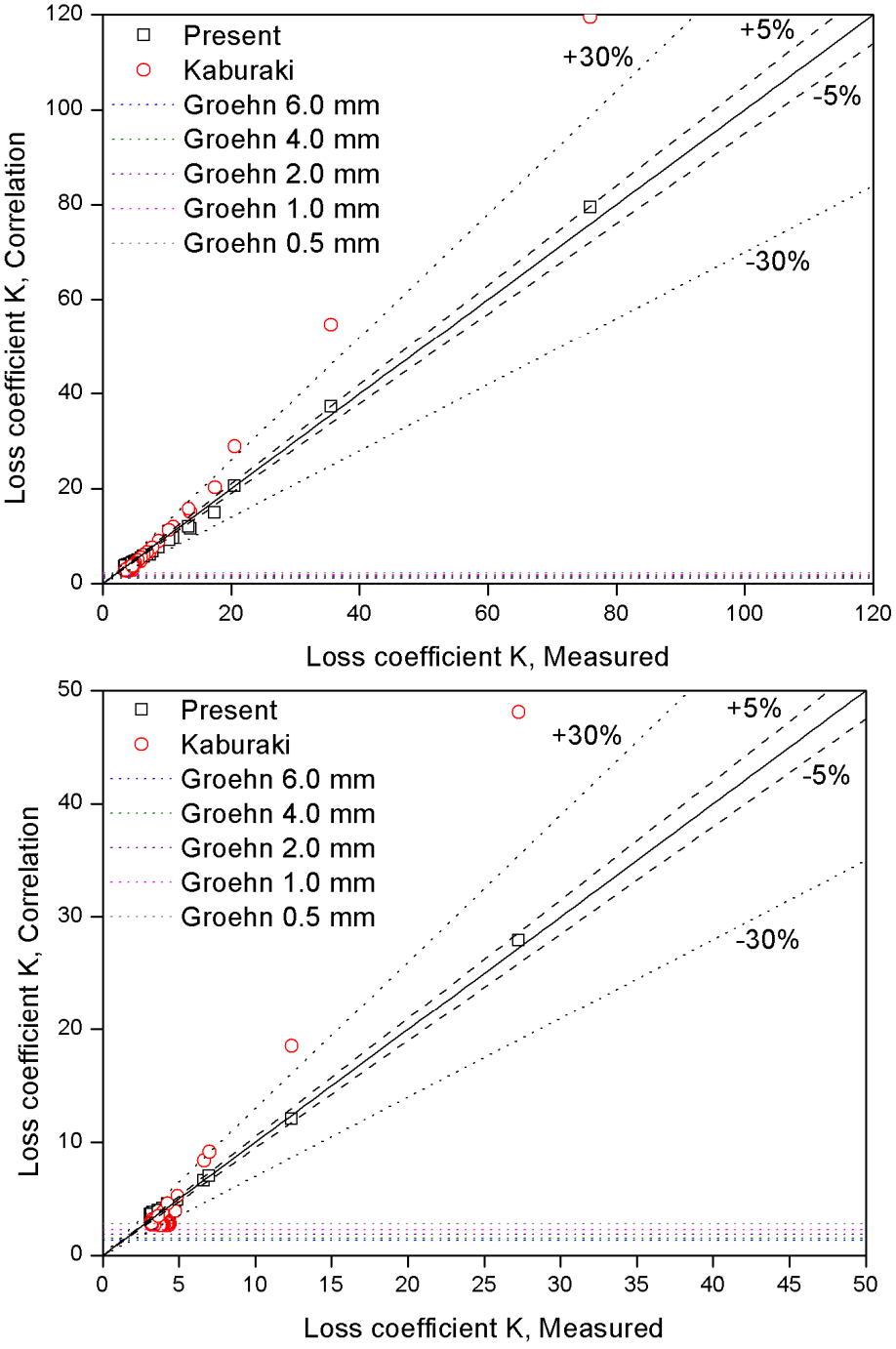

Figure 3.19 Comparison results of the loss coefficient correlations with the experimental data

Chapter 4

Heat Transfer Modeling in FastNet

4.1 Governing Equations

Heat transfer analysis in the FastNet code consists of solid conduction and fluid heat transfer analysis. The solid conduction equation can be written as Eq. (4.1).

$$k_{s,i}\frac{A_{s,i}}{\delta}\left(T_{s,P}-T_{s,i}\right)=Q_{conv,s,P} \tag{4.1}$$

Where, k, A, δ, T, and $Q_{conv,s,P}$ are thermal conductivity, surface area of the solid, distance between solid node P and solid node i, temperature, and convective heat transfer at solid node P. Subscript "*s,i*" is for solid node i and "*s,P*" is for solid node P.

The fluid energy equation can be expressed as Eq. (4.2).

$$\dot{m}_{f,i}C_p\left(T_{f,j+1}-T_{f,j}\right)=Q_{conv,f,i} \tag{4.2}$$

Where, $\dot{m}_{f,i}$, C_p, T and $Q_{conv,f,i}$ are mass flow rate at i-th flow path, specific heat,

temperature, and convective heat transfer at *i*-th flow path. Subscript "*f,j+1"* and "*f,j*" is fluid node at the ends of *i*-th flow path.

Since the FastNet code solves fluid mass and momentum equations and fluid energy equation separately, the solid-fluid connectivity equation is required as Eq. (4.3).

$$Q_{conv,s,P} = Q_{conv,f,i} = h_{f,i} A_{f,i} \left(T_{s,i} - T_{f,i} \right) \tag{4.3}$$

Where, $Q_{conv,s,P}$, $Q_{conv,f,i}$, $h_{f,i}$, $A_{f,i}$, $T_{s,i}$ and $T_{f,i}$ are convective heat transfer at solid node *P*, convective heat transfer at *i*-th flow path, heat transfer coefficient at *i*-th flow path, surface area at *i*-th flow path, temperature at solid node *i*, and temperature at *i*-th flow path.

The heat transfer coefficient is written as Eq. (4.4).

$$h = Nu \frac{k_f}{D_h} \tag{4.4}$$

The FastNet code uses a Nusselt number correlation for turbulence as Eq. (4.5)

$$Nu = 0.021 \mathrm{Re}^{0.8} \mathrm{Pr}^{0.4} \tag{4.5}$$

and for laminar flow as Eq. (4.6).

$$Nu = 4.364 \tag{4.6}$$

Where, h is heat transfer coefficient, Nu is Nusselt number, k_f is thermal conductivity of fluid, D_h is hydraulic diameter, Re is Reynolds number, and Pr is Prandtl number.

4.2 Effective Thermal Conductivity Model

Since FastNet allocates 6 cells for one fuel block, graphite block which contains multiple materials such as fuel compact, coolant hole, and fuel gap is regarded as homogeneous block which has effective thermal conductivity for radial conduction as shown in Fig. 4.1. The ETC model in FastNet is based on the Selengut relation (Selengut, 1961) which was derived by the Maxwell model. In addition, the radiation effect was applied to the form of the corresponding conductivity to the gas conductivity. Thanks to the simple form of the model, it has the advantage of saving computing resources.

For the first time in the MIT study (Han, 1989), the Selengut relation was used to determine the effective thermal conductivity. The model was introduced to evaluate the long time cooling performance of RCCS after the accident. For the simple and fast core simulation, the model was developed as a way of defining a homogeneous medium with an effective thermal conductivity. The Selengut relation is a model for obtaining the effective neutron diffusion coefficient for two different materials with different neutron diffusion coefficient (Selengut, 1961). In the MIT study, using the similarity between the neutron diffusion equation and the heat conduction equation, the effective thermal conductivity for two different materials with different thermal conductivities was obtained. The model is based on Maxwell's far-field methodology (Maxwell, 1873 and McCartney et al., 2007). The

model is expressed as Eq. (4.7)

$$k_{eff,radial} = k_{out} \frac{1 - \sum_{i=1}^{N} \alpha_i \left(\frac{k_{out} - k_i}{k_{out} + k_i} \right)}{1 + \sum_{i=1}^{N} \alpha_i \left(\frac{k_{out} - k_i}{k_{out} + k_i} \right)} \tag{4.7}$$

where, α_i is volume fraction of i-th dispersed component and k_i and k_{out} are conductivity of i-th dispersed component and conductivity of continuous component such as graphite, respectively.

Radiative heat transfer from the fuel block occurs through the fuel gap between the block fuel compact and the graphite. In the FastNet's ETC model, the radiative effect is delivered as equivalent conductivity. This methodology is suggested in Han's study (1989). The equivalent radiation conductivity k_r is added to the gas conductivity. Hence, the conductivity of fuel gap is written as Eq. (4.8).

$$k_{FG} = k_{gas} + k_r = k_{gas} + 4F\sigma\delta\bar{T}^3 \tag{4.8}$$

Where, σ is the Stefan-Boltzman constant, δ is an average distance between two materials, and $\bar{T}$ is the average temperature of two materials. The ETC model was validated against the commercial CFD code CFX-13 and experiments by Shin (2014 and 2017) in SNU.

For a standard fuel block, the volume fractions of materials can be obtained as Eq. (4.9)

$$\alpha_i = \frac{Volume_i}{Volume_{Cell}} \tag{4.9}$$

Where, i is material in the cell (graphite, coolant channel, fuel compact, and fuel gap). The volume fractions of materials for a standard fuel block, which are α_G, α_{CH}, α_{FC}, and α_{FG}, are 0.582536, 0.187219, 0.22127, and 0.008976, respectively and the volume fractions for other types of cells are summarized in Table 4.1. Figure 4.2 shows the cell numbers for types of solid cells for the control rod fuel block and the control rod reflector block.

For axial conduction, the form ETC model can be written as Eq. (4.10).

$$k_{eff,axial} = \sum_{i=1}^{N} \alpha_i k_i \tag{4.10}$$

Although the volume fractions of materials for axial conduction should be calculated without coolant channel, since the conduction of gas at the coolant channel is too small, the same values for volume fractions of materials for axial conduction as that for radial conduction are used.

4.3 Maximum Fuel Temperature Model

Since FastNet allocates 6 cells for a fuel block, detailed temperature distribution in the fuel block cannot be captured. The maximum fuel temperature should be predicted because the maximum fuel temperature is a key parameter of evaluating thermal margin of core of VHTR. To handle this problem, the maximum fuel

temperature (MFT) model was introduced. The MFC model predicts the temperature at fuel center using unit cell of coolant channel and fuel compact. The introduced model uses 1-D estimated conductivity for 2-D conduction problem for unit cell as described in Fig. 4.3. The wall temperature can be obtained from Eq. (4.11).

$$T_W = \frac{Q}{A_W \cdot h} + T_C = \frac{\frac{1}{6} \cdot \pi R_F^2 \cdot q'''}{\frac{1}{12} \cdot 2\pi R_C \cdot h} + T_C = \frac{R_F^2 \cdot q'''}{R_C \cdot h} + T_C \tag{4.11}$$

Where, A_W is the area of graphite's wall, h is heat transfer coefficient, T_C is the bulk temperature of the coolant, R_F and R_C are the radiuses of the fuel compact hole and coolant hole, respectively.

Then, for the graphite conduction, 1-D rectangular conduction was assumed as depicted in Fig. 4.4. The length of the rectangle is assumed as the minimum distance between coolant channel and fuel compact hole and the width of the rectangle is assumed as the length of the interface of coolant channel and graphite in the unit cell. Thus, the conduction in graphite can be expressed as Eq. (4.12).

$$T_{GS} = \frac{Q \cdot \delta_G}{A_W \cdot k_G} + T_W = \frac{\frac{1}{6} \pi R_F^2 \cdot q''' \cdot \left(L_P - R_C - R_{FG} \right)}{\frac{1}{12} \cdot 2\pi R_C \cdot k_G} + T_W \tag{4.12}$$

Where, δ_G is the distance between coolant channel and fuel compact hole and k_G is the conductivity of the graphite.

The conduction at the fuel gap is assumed as a parallel gap of which distance is the distance between graphite and fuel compact and the width is assumed as the length of the interface of fuel compact and fuel gap in the unit cell. Hence the conduction at fuel gap can be written as Eq. (4.13).

$$T_{FS} = \frac{Q \cdot \delta_{FG}}{A_{FS} \cdot k_{FG}} + T_{GS} = \frac{\frac{1}{6}\pi R_F^2 \cdot q''' \cdot \left(R_{FG} - R_F\right)}{\frac{1}{6} \cdot 2\pi R_F \cdot k_{FG}} + T_{GS} \tag{4.13}$$

Where, δ_{FG} is the distance between graphite and fuel compact, A_{FS} is the area of fuel compact wall in the unit cell, and k_{FG} is the equivalent conductivity of the helium which contains radiation effect.

The conduction in fuel compact is assumed as cylindrical 1-D conduction because of its geometry. It can be derived as follows.

$$\nabla \cdot k \nabla T\left(r\right) = -q'''\left(r\right) \tag{4.14}$$

$$\frac{1}{r}\frac{\partial}{\partial r}\left(k_F r \frac{\partial T}{\partial r}\right) = -q''' \tag{4.15}$$

$$k_F r \frac{\partial T}{\partial r} = -\frac{1}{2} q''' r^2 \tag{4.16}$$

$$T\left(r\right) = T_0 - \frac{1}{4}\frac{q'''}{k_f} r^2 \tag{4.17}$$

$$T_0 = T_f + \frac{1}{4}\frac{q'''}{k_f} r_f^2 \tag{4.18}$$

Hence, the conduction in the fuel compact can be expressed as Eq. (4.19).

$$T_{FC} = \frac{1}{4}\frac{q'''R_F^2}{k_F} + T_{FS} \tag{4.18}$$

Where, k_F is the conductivity of the fuel compact.

To verify the Maximum Fuel Temperature (MFT) model, the calculation results were compared with 2-D CFD analysis as seen in Fig 4.5. For a wide range of condition, wide heat source and fluid temperature range was assumed. Fuel compact power density was set to be 20 – 60 MW/m^3. The fuel temperature was set to be 750 – 1400 K. The heat transfer coefficient at coolant channel is set to be 1,700 W/m^2·K and the emissivity was set to be 0.85 for radiation effect.

Fig. 4.6 shows the comparison results of MFT model prediction and CFD analysis. The results of MFT model prediction and CFD analysis show good agreement. The maximum error at fuel compact center is 2.82 K.

4.3 Procedure of FastNet

The calculation procedure of FastNet consists of flow analysis, solid conduction, and flow energy analysis. The flow chart of FastNet is presented in Fig. 4.7. First, the input data and the information of initial geometry and flow condition are read. The Fig. 4.8 is the example of meshes for flow network analysis and solid conduction calculation for FastNet. FastNet uses different meshes for fluid analysis and solid conduction analysis and the information of two calculation is connected by using location information of the mesh. Then, the flow distribution for the entire 3-D network is analyzed by looped network analysis method. The example of 3-D

mesh for looped network analysis is shown in Fig. 4.9. After that, the solid conduction analysis is progressed using ETC model. The example of calculation for solid conduction is as Eq. (4.19) and the solid mesh for this calculation is described in Fig. 4.10.

$$\begin{aligned}
&\frac{k_{eff_radial,1}+k_{eff_radial,3}}{2}A\frac{T_{s1,w}-T_{s3,w}}{\delta_{1,3}}\\
&+\frac{k_{eff_radial,5}+k_{eff_radial,3}}{2}A\frac{T_{s5,w}-T_{s3,w}}{\delta_{5,3}}\\
&+\frac{k_{eff_radial,6}+k_{eff_radial,3}}{2}A\frac{T_{s6,w}-T_{s3,w}}{\delta_{6,3}}\\
&+\frac{k_{eff_axial,3,up}+k_{ff_axial,3}}{2}A_b\frac{T_{s3,up,w}-T_{s3,w}}{H_b}\\
&+\frac{k_{ff_axial,3,down}+k_{ff_axial,3}}{2}A_b\frac{T_{s3,down,w}-T_{s3,w}}{H_b}\\
&=-h_{f,ch1}A_{ch}\left(T_{ch1}-T_{s3,w}\right)-h_{f,bh4}A_{by}\left(T_{by4}-T_{s3,w}\right)-q_{s3}
\end{aligned} \tag{4.19}$$

Next, fluid temperature rising due to solid temperature for vertical flow is analyzed and lateral mixing between layers is calculated for energy balance. The fluid temperature rising for vertical flow and the lateral fluid mixing are calculated from the top to the bottom layer by layer. The fluid temperature rising is calculated as Eq. (4.20) as seen in Fig. (4.11).

$$mC_P\left(T_{f,down}-T_{f,up}\right)=hA\left(T_s-T_f\right) \tag{4.20}$$

For the fluid temperature at the bypass gap of lower node can be expressed as Eq. (4.21).

$$T_{f,by,down} = \frac{mC_P T_{f,by,up} + hA_{by} T_{s,B1} + hA_{by} T_{s,B2} - hA_{by} T_{f,by,up}}{mC_P + hA_{by}} \tag{4.21}$$

Likewise, for the fluid temperature at the coolant channel of lower node can be calculated as Eq. (4.22).

$$T_{f,ch,down} = \frac{mC_P T_{f,ch,up} + hA_{ch} T_{s,B} - \frac{1}{2} hA_{ch} T_{f,ch,up}}{mC_P + \frac{1}{2} hA_{ch}} \tag{4.22}$$

The temperature of the fluid at the flow path is the average temperature value of upper node and lower node as Eq. (4.23).

$$T_f = \frac{1}{2}\left(T_{f,up} + T_{f,down}\right) \tag{4.23}$$

The lateral mixing for energy balance is calculated as Eq. (4.24)

$$\sum m_{in} C_P T_{in} = \sum m_{out} C_P T_{out} \tag{4.24}$$

The example calculation of the lateral mixing is as Eq. (4.25) and depicted in Fig. 4.11.

$$m_{up}C_P T_{up,7} + m_{in,0}C_P T_0 + m_{in,3}C_P T_2 + m_{in,4}C_P T_3 + m_{in,5}C_P T_4 = m_{down}C_P T_1 + m_{out,6}C_P T_1 + m_{out,8}C_P T_1 \quad (4.25)$$

Finally, the procedure is repeated until the residual reaches desired value.

Table 4.1 Volume fraction for types of solid cell

Block type	Standard	Control fuel			Control reflector	
Cell type	1	1	2,3	4,5,6	1	2,3,4,5,6
α_G	0.5825	0.4255	0.5965	0.5825	0.5801	1
α_{CH}	0.1872	0.0666	0.1766	0.1872	0	0
α_{FC}	0.2213	0.0846	0.2180	0.2213	0	0
α_{FG}	0.0090	0.0034	0.0088	0.0090	0	0
α_{CR}	0	0.4199	0	0	0.4199	0

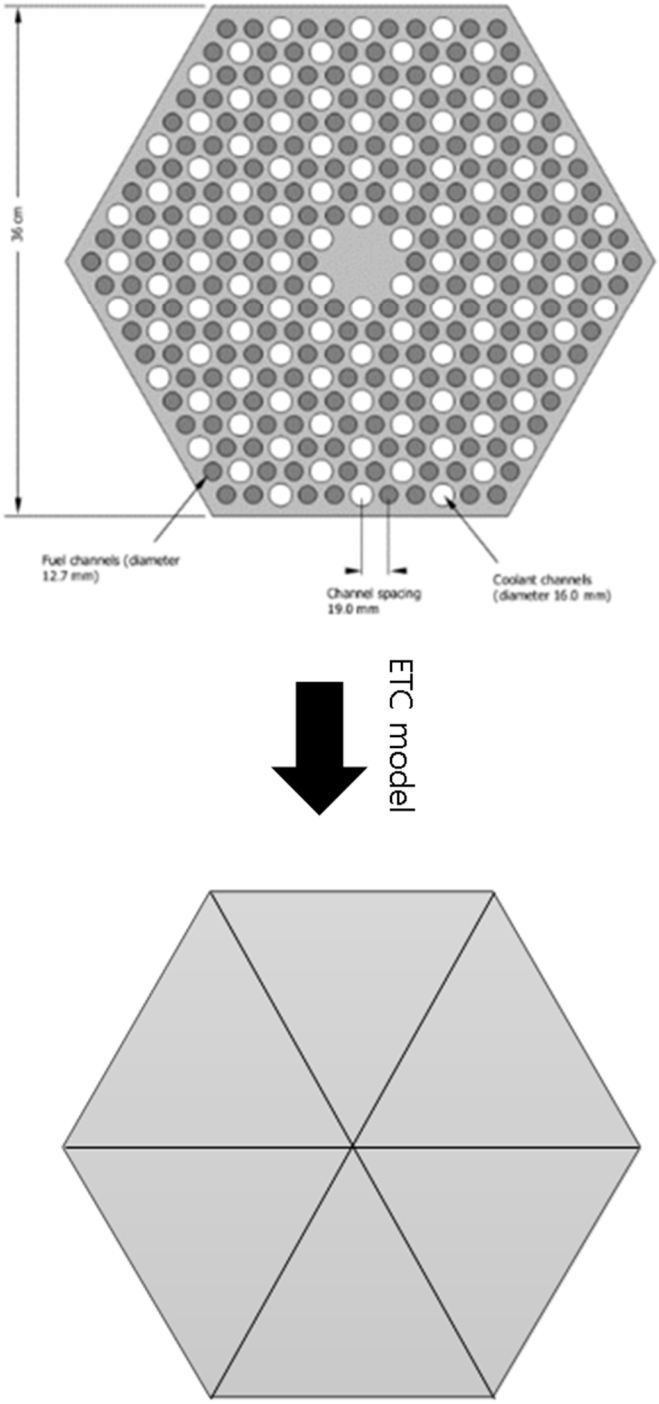

Figure 4.1 Effective Thermal Conductivity model

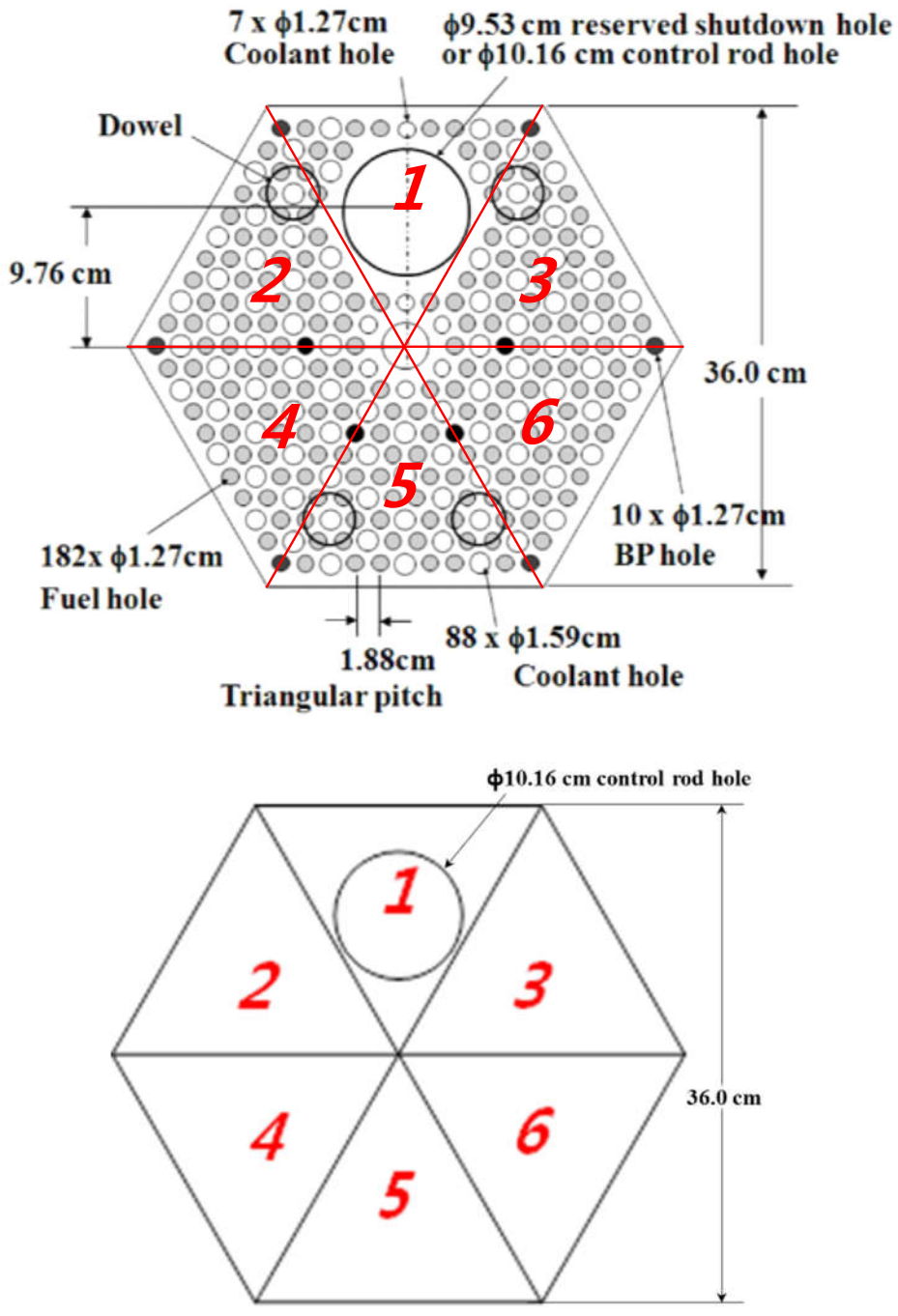

Figure 4.2 Solid meshes and cell types for the control rod fuel block and control rod reflector block

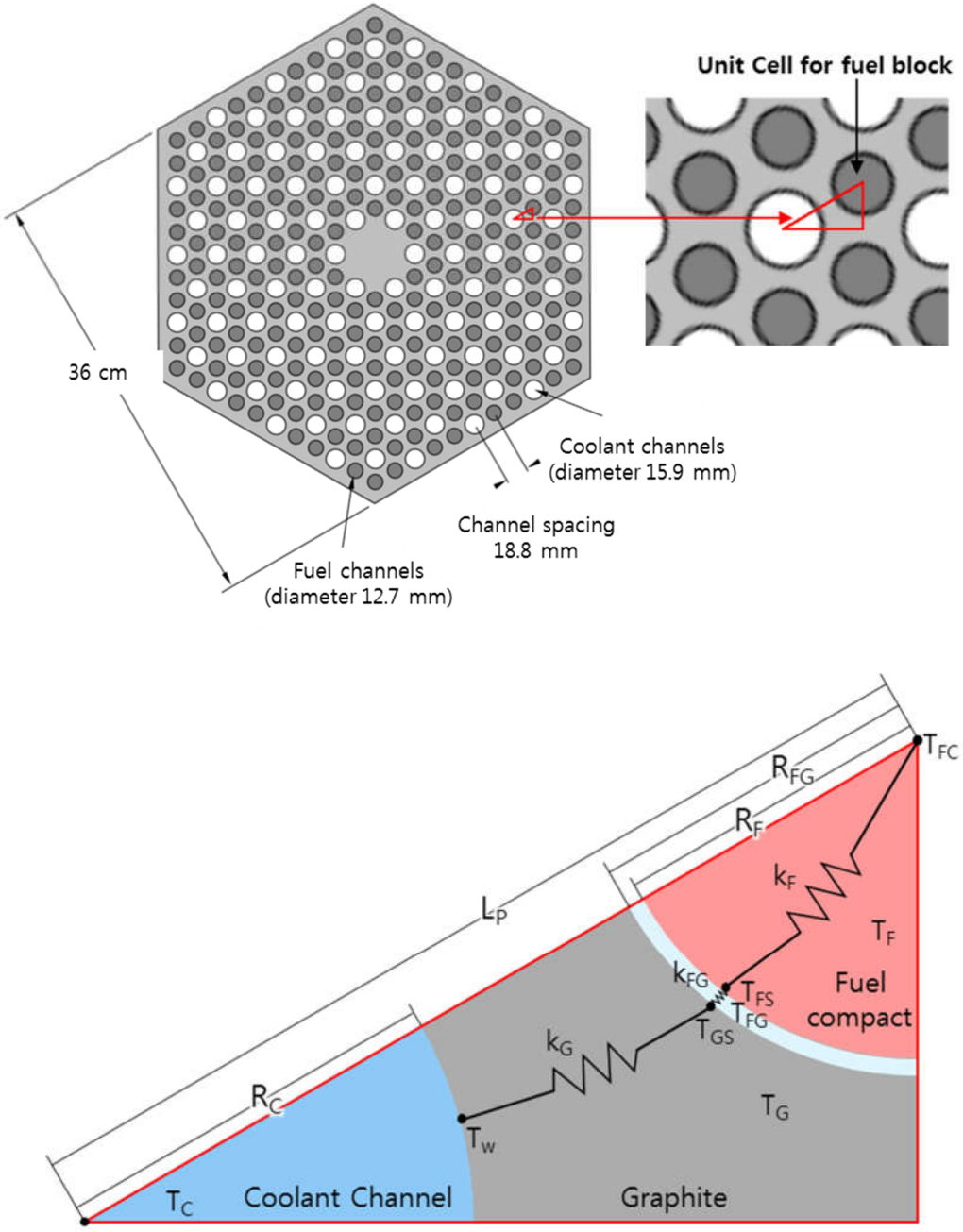

Figure 4.3 Unit cell for Maximum Fuel Temperature model

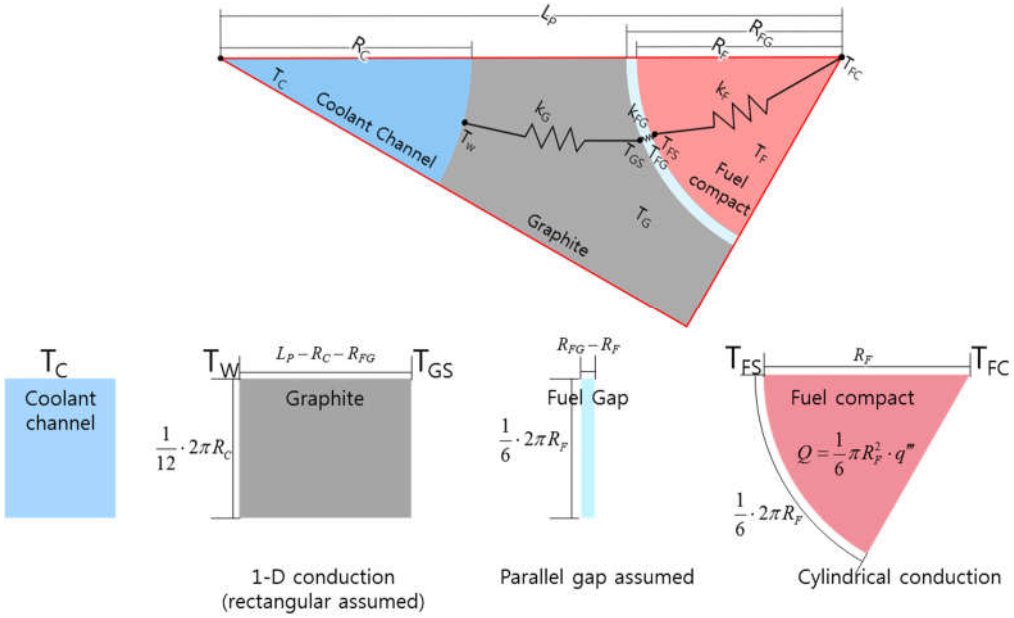

Figure 4.4 1-D estimated conduction in unit cell for predicting maximum fuel temperature

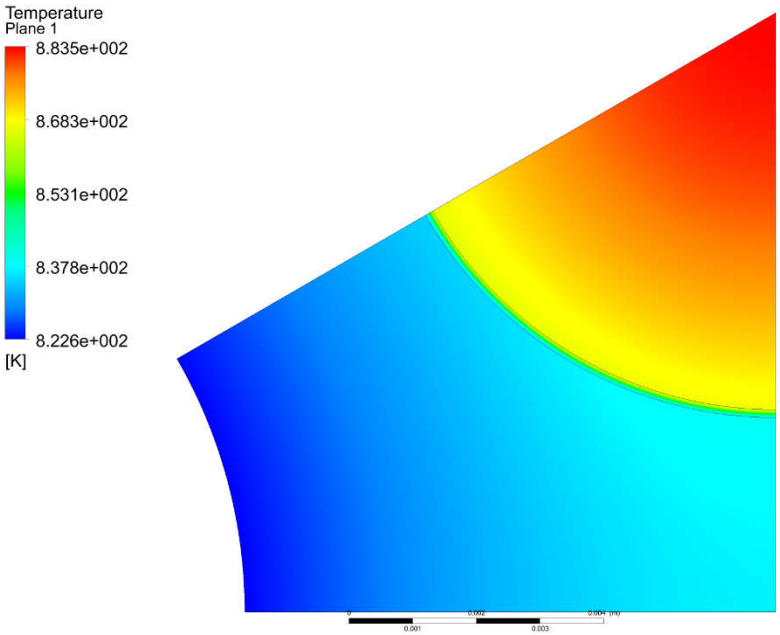

Figure 4.5 CFD analysis results for unit cell model

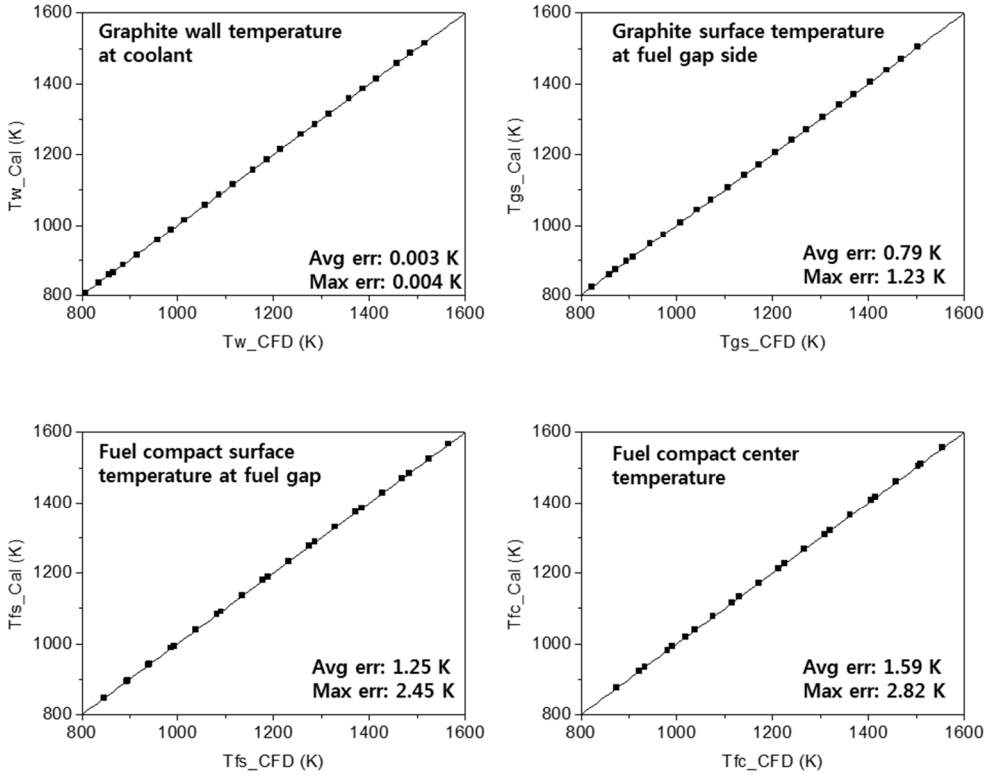

Figure 4.6 Comparison results of Max Fuel Temp model and CFD analysis

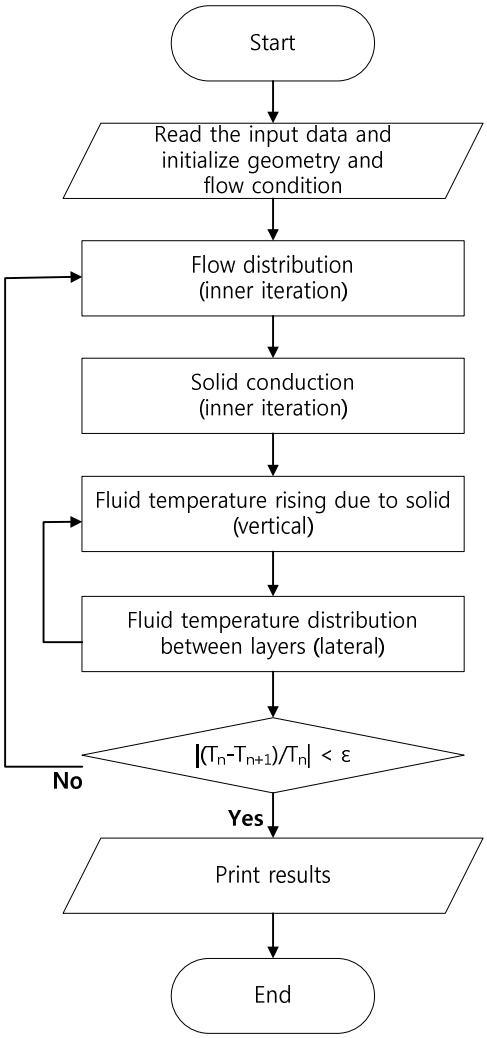

Figure 4.7 The flow chart of FastNet

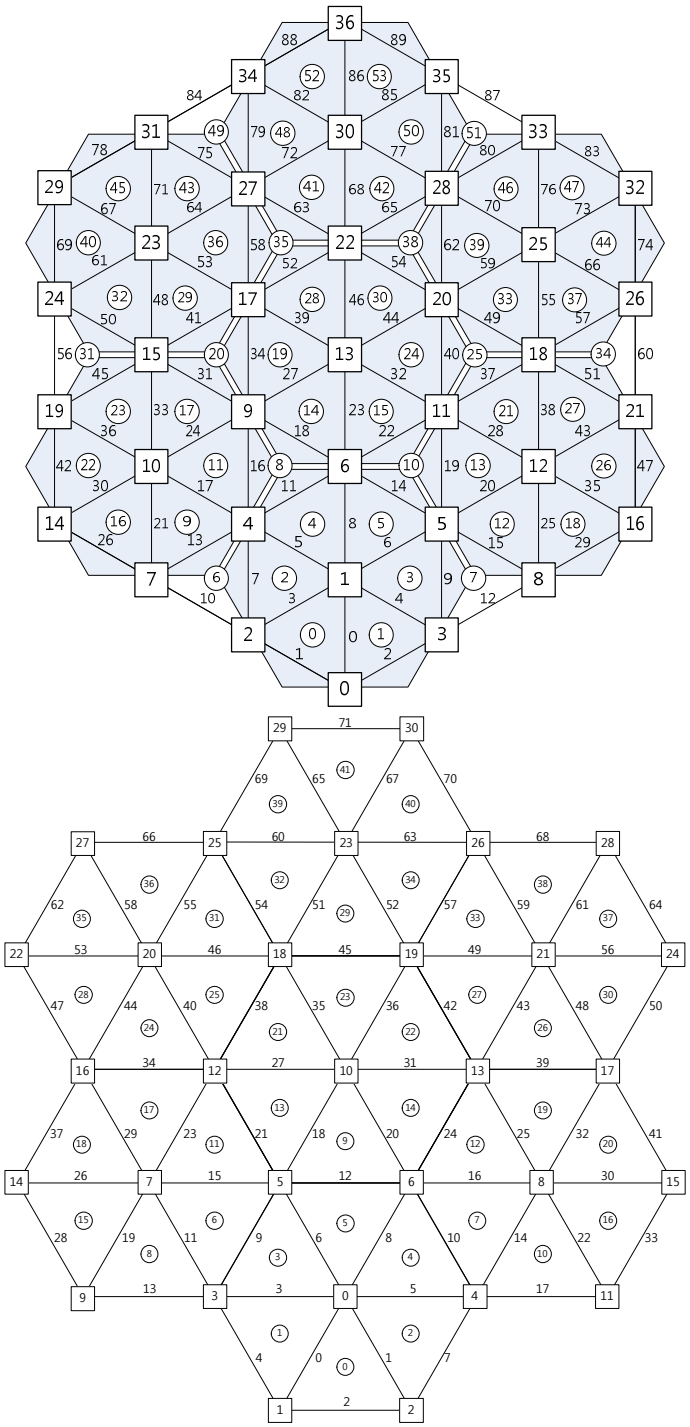

Figure 4.8 The example of meshes for flow network analysis and solid conduction analysis.

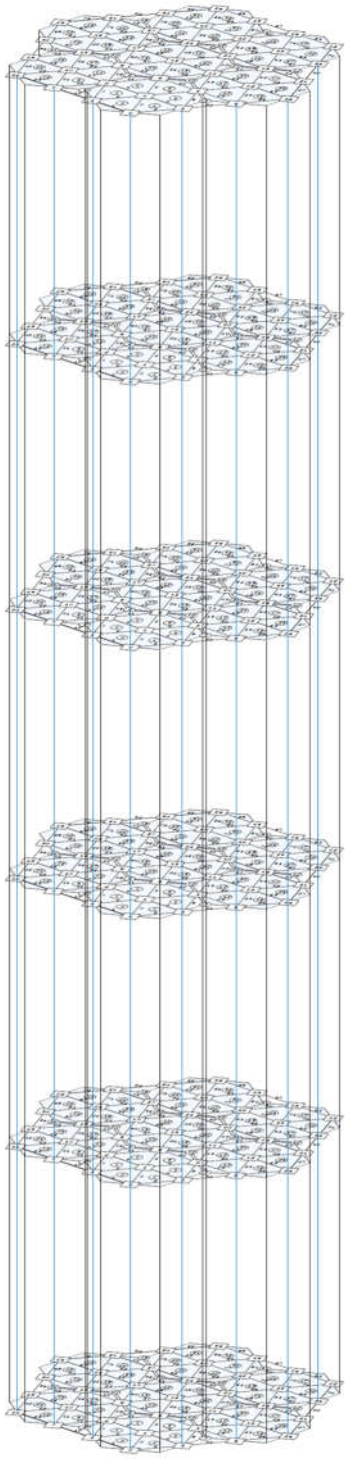

Figure 4.9 The example of 3-D mesh for looped network analysis

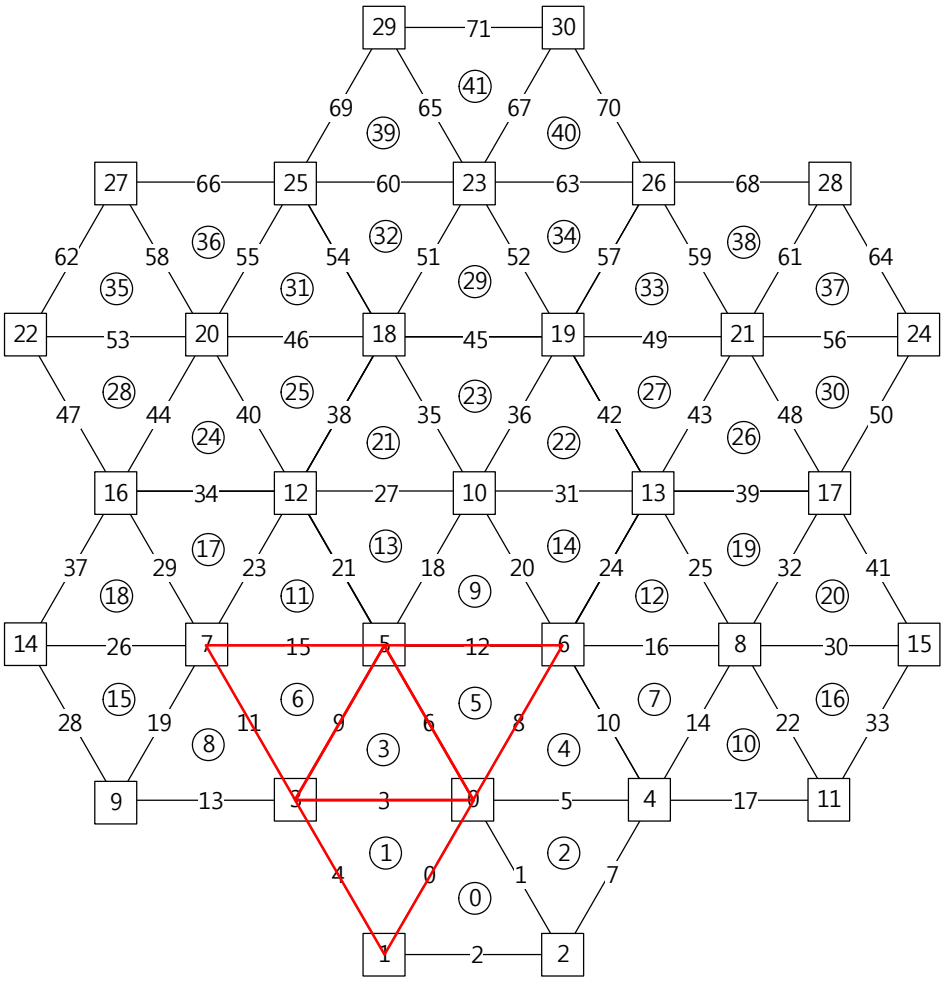

Figure 4.10 Solid mesh for the example of calculation for solid conduction

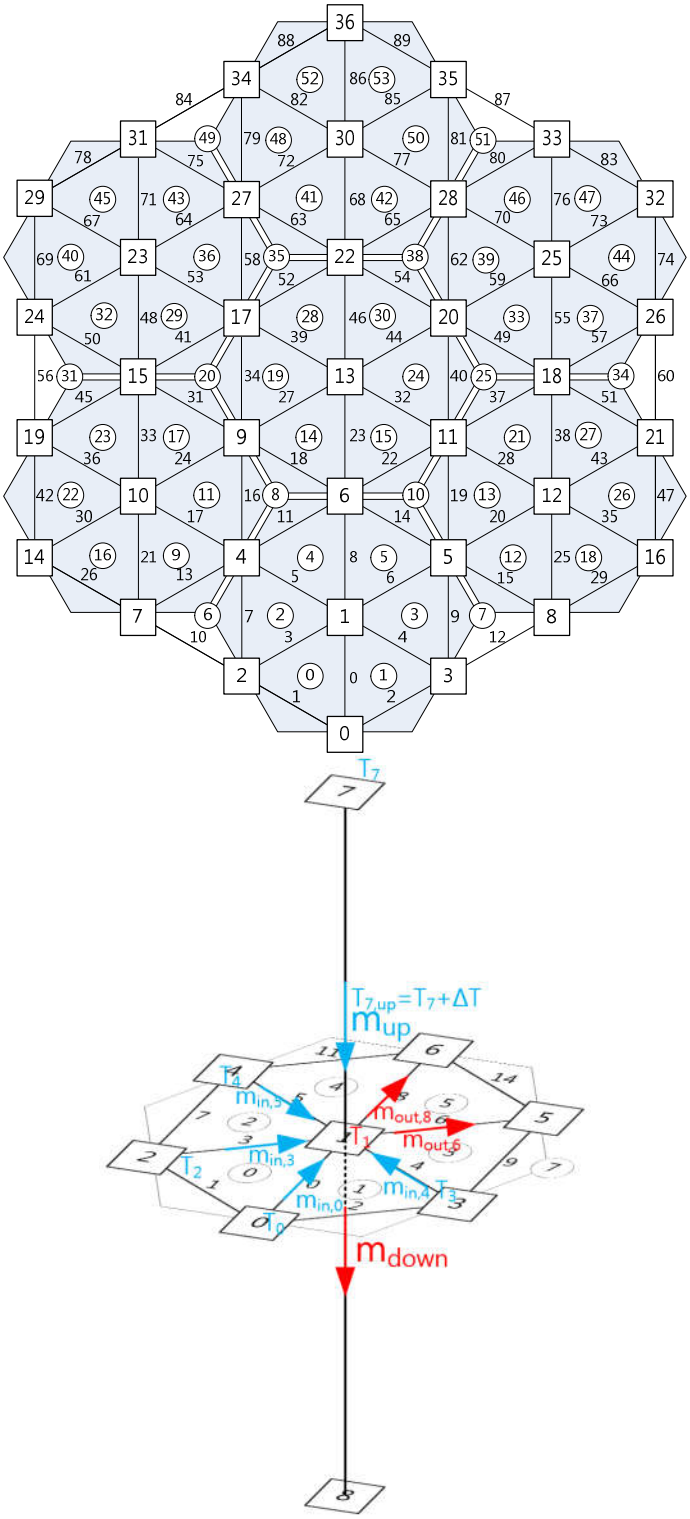

Figure 4.11 Calculation of lateral mixing for energy balance

Chapter 5

Verification and Validation of FastNet

5.1 Validation of Flow Network Model

The FastNet code was validated by the experimental and CFD simulation results for the multi-block experiment (Yoon, 2012). The experimental facility and block configuration were described in Fig. 5.1. The working fluid is air at ambient temperature and pressure. The experimental facility consists of 5 fuel block columns and 2 reflector block columns with 4 core layers and 1 transition layer. This experimental study was carried out for investigating the characteristics of the bypass flow and the cross flow.

The test conditions for code validation were uniform bypass gap cases; BG2-CG0, and BG6-CG0, and non-uniform bypass gap case: BG6242-CG2. BG2-CG0 and BG6-CG0 cases have uniform bypass gap of which size is 2 mm and 6 mm, respectively. CG0 means the size of the cross gap is 0 mm. BG6242-CG2 case means 6 mm, 2 mm, 4 mm, and 2 mm bypass gap from the top to the bottom and the 2 mm cross gap case, which allows observation of cross flow effect. Fig 5.2 shows the block configuration of each case. Figs. 5.3 and 5.4 are the comparative results of the experiments and FastNet for BG2-CG0 and BG6-CG0 case. Calculated results of the FastNet code shows a good agreement with the

experimental data. Both the pressure distribution and mass flow distribution are predicted accurately. The discrepancy of the bypass ratio is under 1% and the pressure drop graphs shows good agreement between experimental data and FastNet prediction results as shown in Figs. 5.3 and 5.4.

The comparison results for non-uniform bypass gap were plotted in Fig. 5.5. The variant bypass gap size along axial direction causes the cross flow phenomenon significantly. As seen in the left side of the Fig. 5.5, the FastNet code can capture the bypass ratio and the error was under 4%. For the pressure drop, although the calculation results of FastNet slightly underestimate over the experimental data, when considering the uncertainty of the experiment, it can be said that FastNet shows reasonable prediction. In the experiments, the exact arrangement of the blocks was difficult and also it was difficult to set the gap conditions. Moreover, as seen in Fig. 5.6, sudden pressure drop between layers (location 1.6080 m) due to sudden area change was well simulated in the FastNet code.

In addition to the experimental results, the computational capability of FastNet was evaluated through comparison with CFD analysis results. Figs. 5.7 and 5.8 show the comparative results of FastNet prediction and CFD analysis results for uniform bypass gap cases (BG2-CG0 and BG6-CG0). As seen in the graphs, the FastNet prediction results show very good agreement with CFD calculation results. Fig. 5.9 represents the comparison results for non-uniform bypass gap case between FastNet and CFD. As shown in the upper side of Fig. 5.9, the results of the FastNet prediction show good agreement with the CFD analysis results and the error was under 2%. For the pressure drop, the results of the FastNet prediction and the CFD analysis show very good agreement. Since the gap setting of the CFD code and FastNet can be controlled more precisely than the experiment, more consistent

results were obtained.

5.2 Code to Code Validation

5.2.1 Single Column Analysis

To evaluate the calculation capability of FastNet, a single column analysis was simulated and compared with CFD analysis and CORONA calculation results. 9 layers (6 fuel layers) were assumed and the bypass gap was set to 1 mm. The other main variables for calculation were summarized in Table 5.1. CFX turbulence model was selected to RNG k-ε model. Fig. 5.10 represents the calculation domain for CFD and network model of FastNet. The comparison results of axial temperature distributions at the center of the hottest fuel compact were seen in Fig. 5.11. FastNet slightly underestimates the maximum fuel temperature than CFX. A possible factor for discrepancy is parabolic temperature distribution at a fuel block. CFD codes and CORONA can capture the parabolic temperature distribution at a fuel block as described in Fig. 5.12 but FastNet cannot capture this distribution because of its coarse mesh grid. Another possible reason is convergence residual. In CFD calculation, residual of turbulence kinetic energy could not be satisfied with certain value (10^{-4}) as shown in Fig. 5.13. In general, 10^{-4} is relatively loose convergence, even though it may be sufficient for many engineering applications. The coolant outlet temperatures and maximum fuel temperatures were summarized in Table. 5.2. The most important characteristic of FastNet is calculation speed. As seen in Table 5.2, the calculation times of CFD, CORONA, and FastNet for single column analysis are 46 hours, 362 sec, and 0.5 sec, respectively as presented in Fig.

5.14. It means that the calculation speed of FastNet is 700 times faster than that of CORONA in single column analysis.

However, the underestimation of the FastNet prediction for maximum temperature is not good to evaluate the thermal margin in terms of conservatism. To overcome this problem, a model which can predict the peak temperature of the block due to the parabolic temperature distribution should be developed. The parabolic shape of the temperature distribution in the fuel block could be a function of flow rate of the bypass gap and the temperature of the bypass flow. Further work can be modeling of the prediction model of peak temperature of the fuel block.

5.2.2 Whole Core Analysis

To confirm calculation performance of FastNet, whole core analysis of 1/6 model of VHTR 350 MWth was carried out. 6 layers and 36 columns were simulated and bypass gap was set to 2 mm. Main calculation conditions are tabulated in Table 5.3. The computational domain of 1/6 core model of CFD was described in Fig. 5.14. Block configuration and fuel column indexing number with power peaking factor were presented in Fig. 5.16. As shown in Fig 5.17, the FastNet code can calculate flow distribution and temperature distribution of VHTR core. The comparison results of temperature distribution at the hot spot plane are seen in Fig. 5.18. The temperature distribution results of CFD, CORONA, FastNet are in good agreement. And the difference of maximum temperature in the fuel columns between CFX and CORONA is 48˚C while CFX and FastNet is 56˚C. Moreover the average differences of maximum temperatures are 25.55˚C for CFX and CORONA while 23.6˚C. The definition of the average difference is average value of the absolute

value of the temperature difference. Therefore, it can be said that the accuracy of FastNet for maximum temperature prediction is similar to CORONA. However, when comparing maximum temperature of FastNet with that CORONA, larger temperature difference was occurred. The reason for this discrepancy has not been clear and this reason of the error should be investigated through further studies.

Nevertheless, above all, the important strength of FastNet is the speed of calculation. The calculation time of the FastNet is about 30 seconds, whereas that of CORONA is 7,620 seconds with a single processor (i7 – 3.5GHz) calculation for whole core simulation. Even with parallel computation of CORONA, the computation time is 1,980 seconds, which is much slower than FastNet's single-core calculation as seen if Fig. 5.19. The calculation speed of FastNet over that of CORONA is tabulated in Table 5.7.

Table 5.1 Calculation conditions for single column analysis

Parameter	Value
Mass flow rate (kg/s)	1.2072
Inlet temperature (K)	763.15
Compact power density (MW/m^3)	28.4
Total power (MW)	3.538
Pressure (MPa)	7

Table 5.2 Coolant outlet temperature and maximum fuel temperature

Result variables	CFD	CORONA	FastNet	Analytic
Outlet temperature (°C)	1056	1054	1055	1055
Max temperature (°C)	1269	1258	1239	-
Calculation time	46 hour	362 sec	0.5 sec	-

Table 5.3 Coolant outlet temperature and maximum fuel temperature

Parameter	Value
Mass flow rate (kg/s)	26.245
Inlet temperature (°C)	259
Total power (MW)	33.901
Average fuel compact power density (MW/m^3)	25.67
Pressure (MPa)	7

Table 5.4 Flow distribution

Channel	Coolant channel	Bypass gap	Control Hole
	kg/s	kg/s	kg/s
CFX	15.9	1.468	8.88
CORONA	15.673	1.441	9.134
FastNet	14.76	1.572	9.908

Table 5.5 Maximum temperature in the fuel columns [°C]

Column	CFX	CORONA	**FastNet**	**Column**	CFX	CORONA	**FastNet**
1	779	763	751	**7**	756	779	775
2	769	741	770	**8**	905	935	**849**
3	912	**960**	861	**9**	992	981	948
4	813	815	820	**10**	815	819	807
5	794	753	778	**11**	809	776	796
6	916	961	899				

Table 5.6 Difference of temperatures [°C]

	Max temp. difference [°C]	Average difference [°C]
CFX vs. CORONA	48 (column 3)	25.55
CFX vs. FastNet	56 (column 8)	23.6
CORONA vs. FastNet	99 (column 3)	35.2

Table 5.7 Calculation speed of FastNet over that of CORONA

Case		FastNet calculation speed compared to CORONA
Single column analysis		X 700
Whole core analysis	Parallel core	X 66
	Single core	X 254

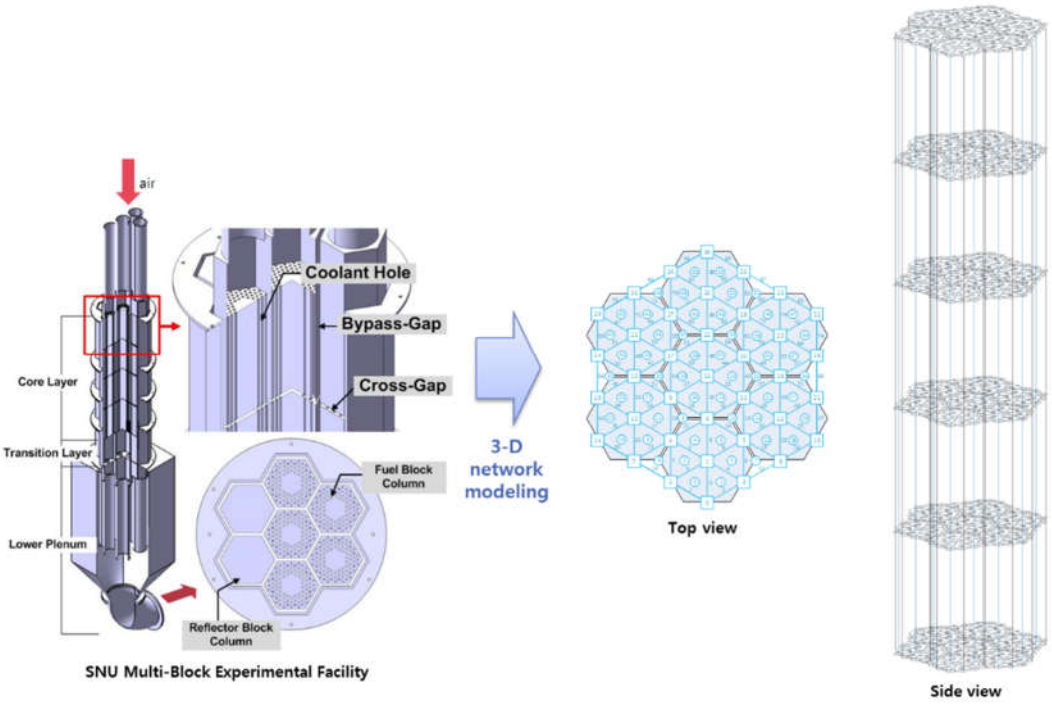

Figure 5.1 SNU multi-block experimental facility and block configuration and the fluid mesh for the experimental facility

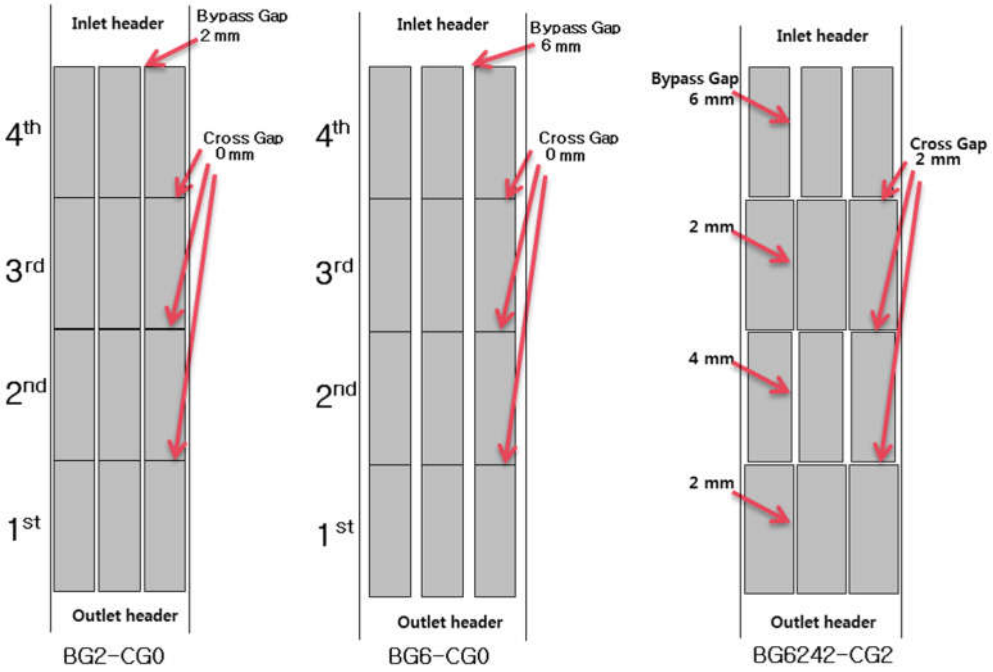

Figure 5.2 Block configuration of each case

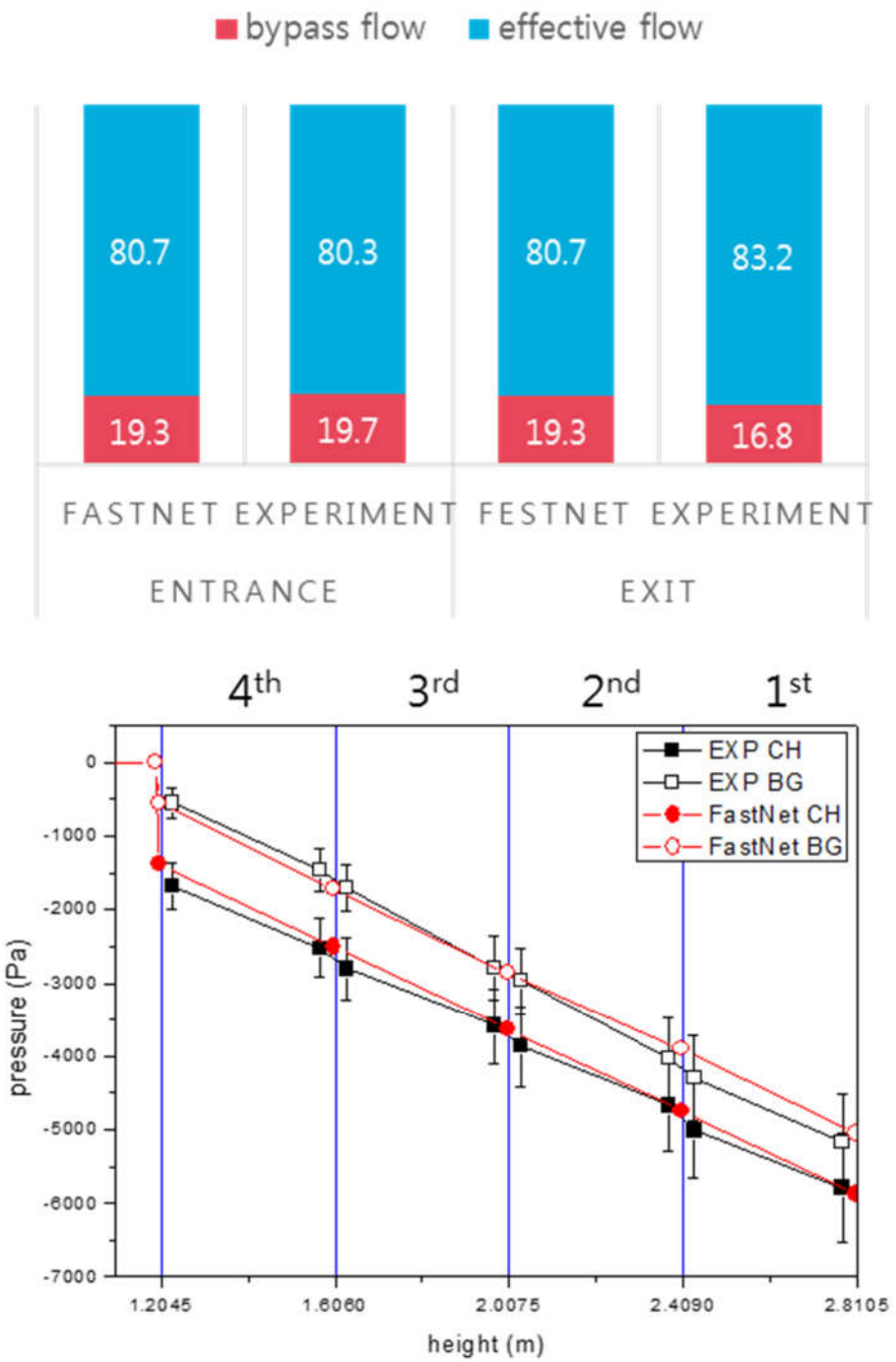

Figure 5.3 Comparative results of FastNet prediction and experimental data (BG2-CG0 case)

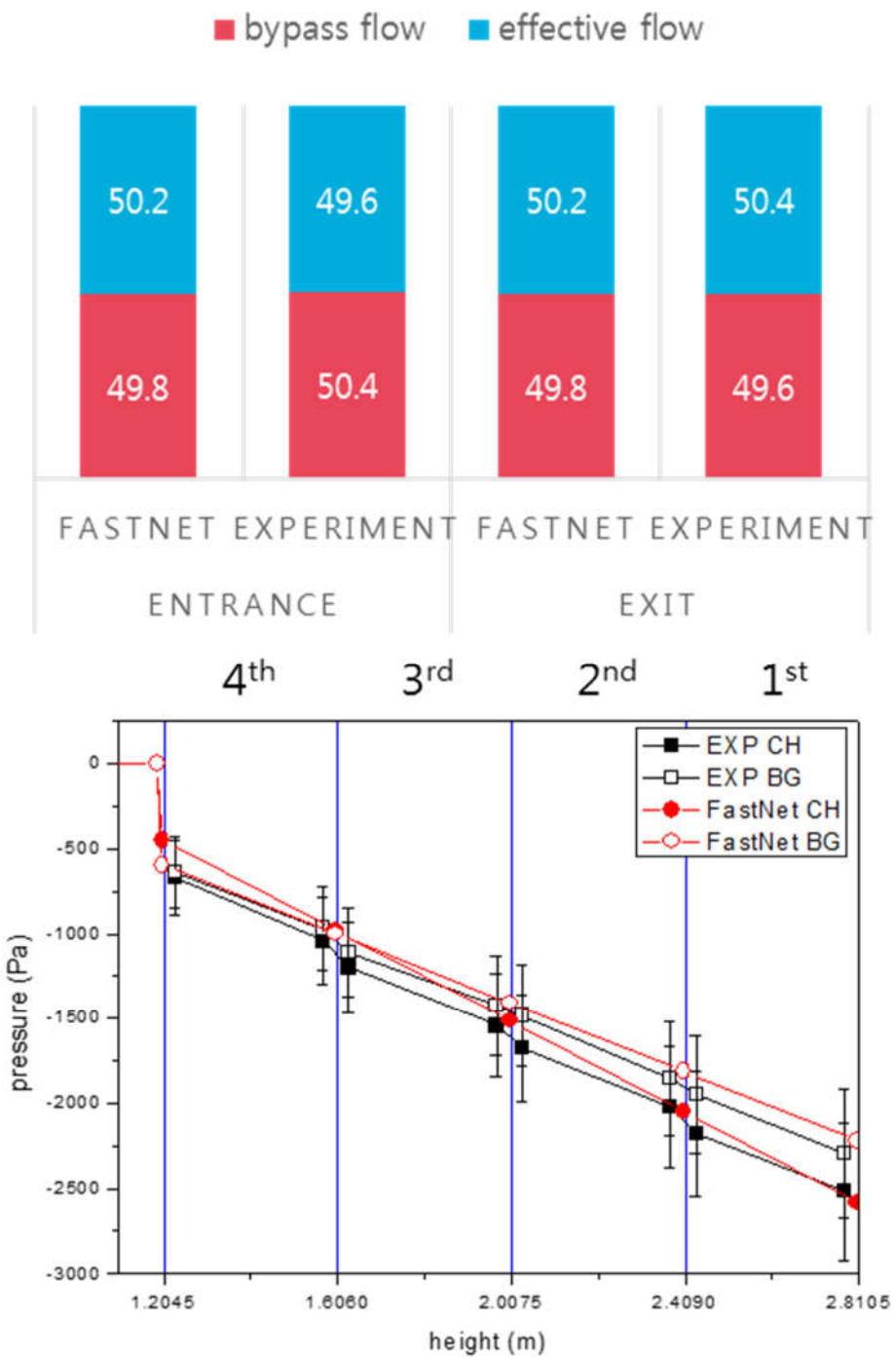

Figure 5.4 Comparative results of FastNet prediction and experimental data (BG6-CG0 case)

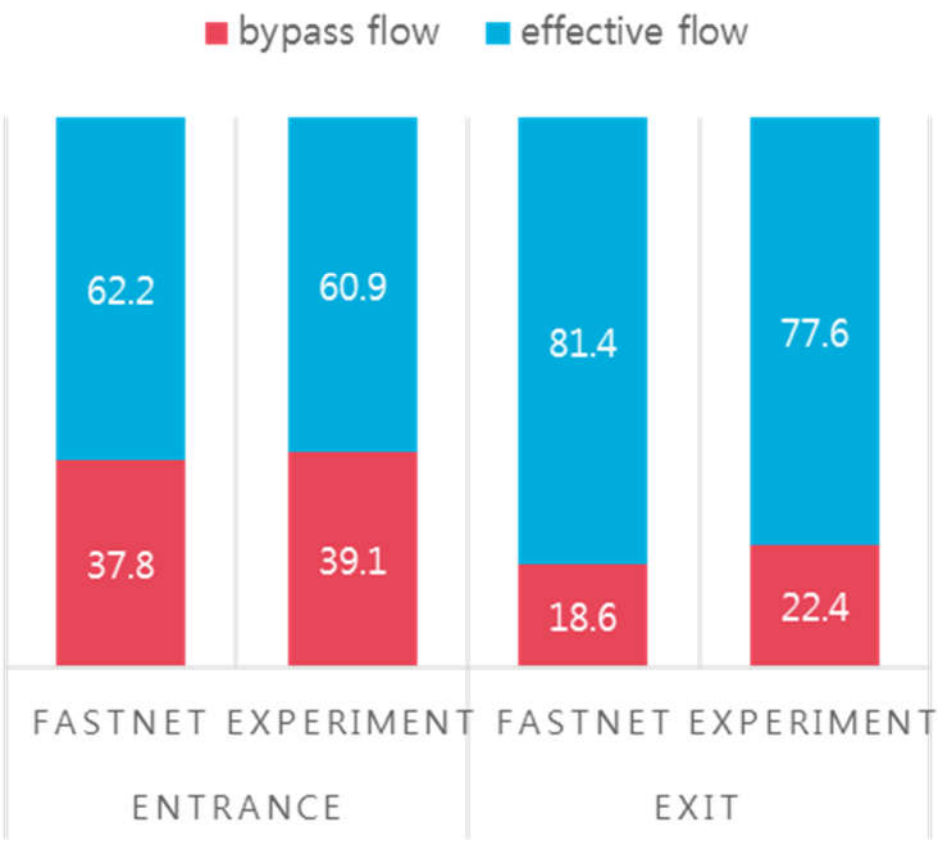

Figure 5.5 Comparative results of FastNet prediction and experimental data: bypass flow ratio (BG6242-CG2 case)

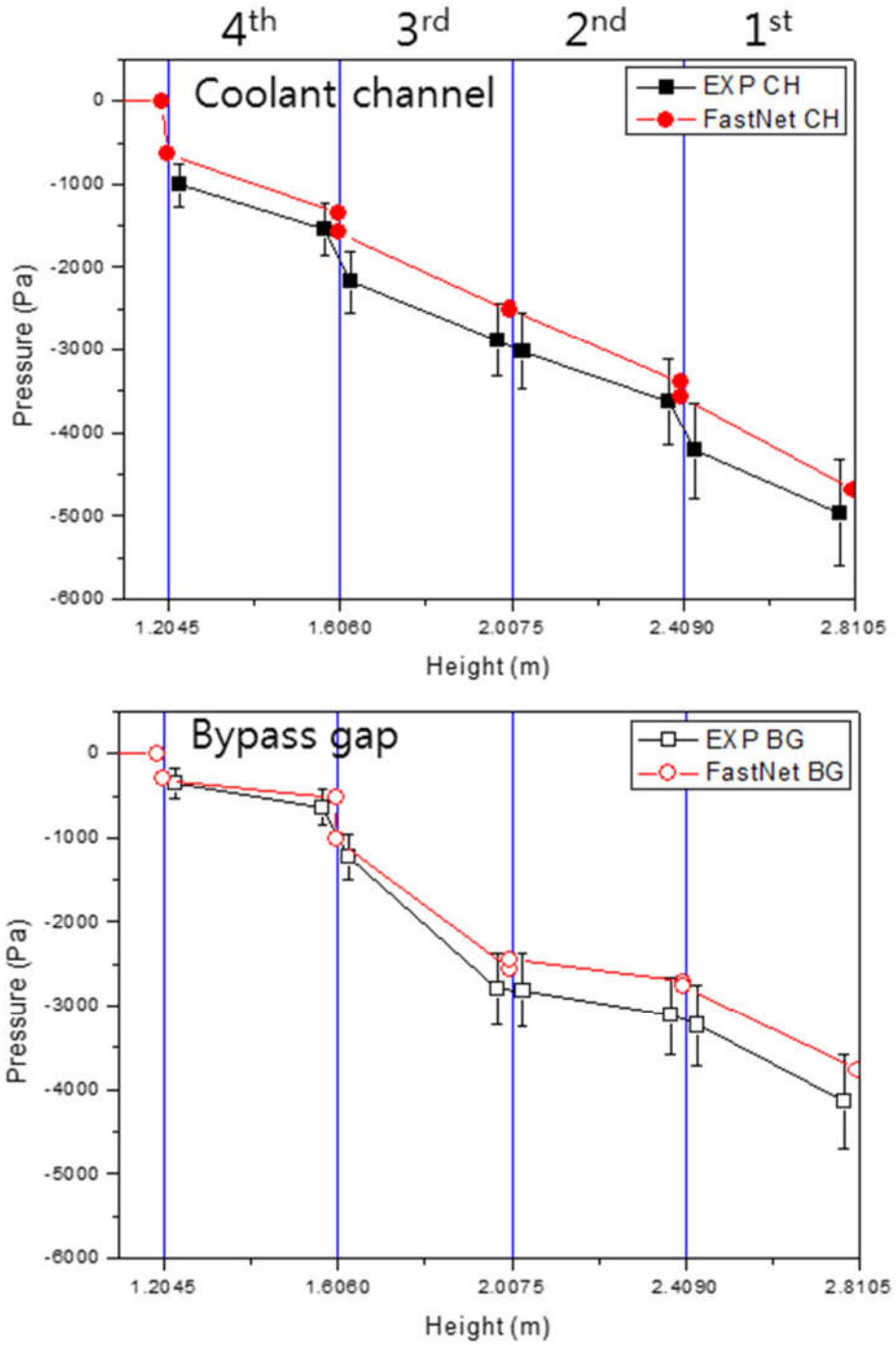

Figure 5.6 Comparative results of FastNet prediction and experimental data: pressure drop (BG6242-CG2 case)

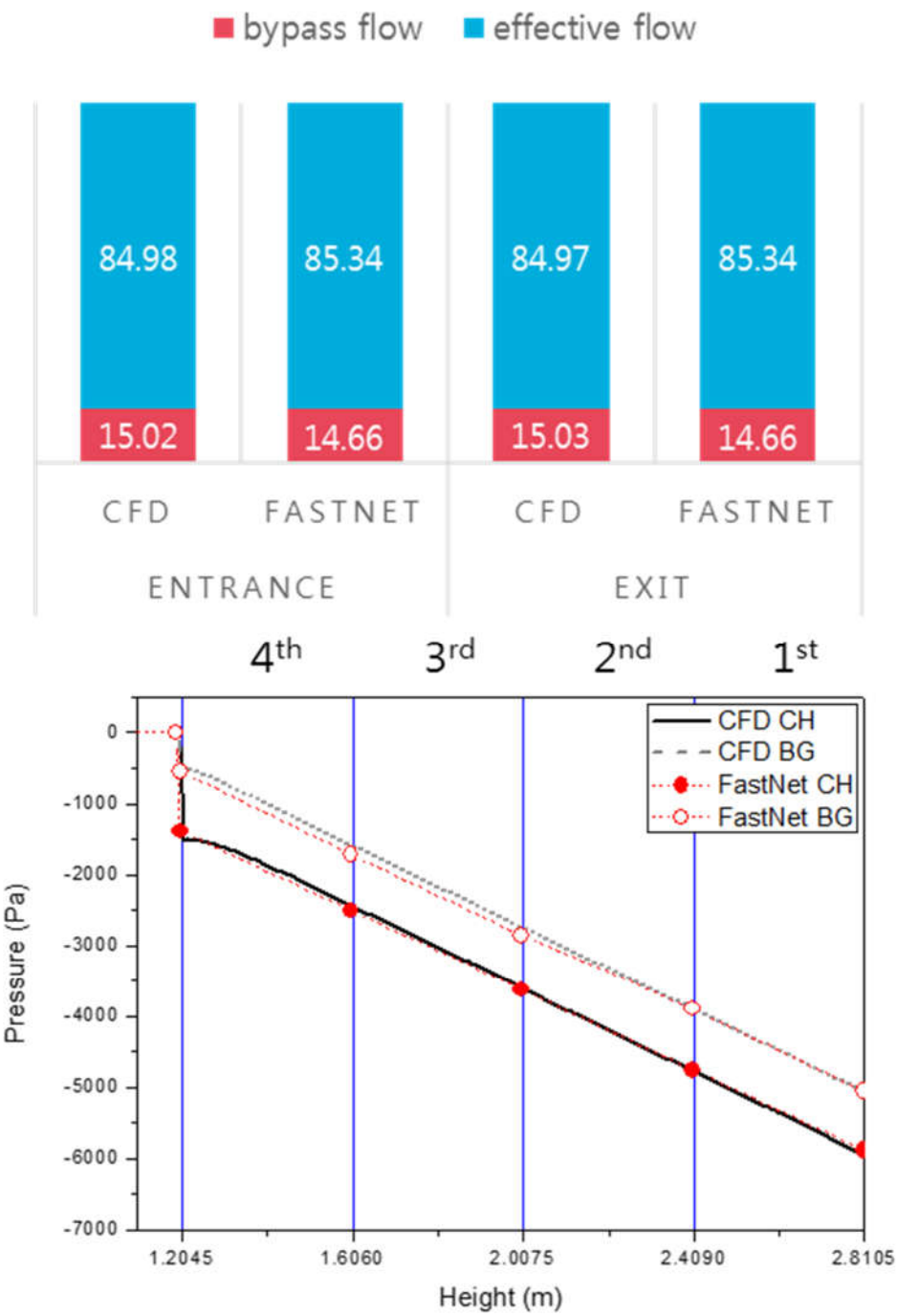

Figure 5.7 Comparative results of FastNet prediction and CFD analysis (BG2-CG0 case)

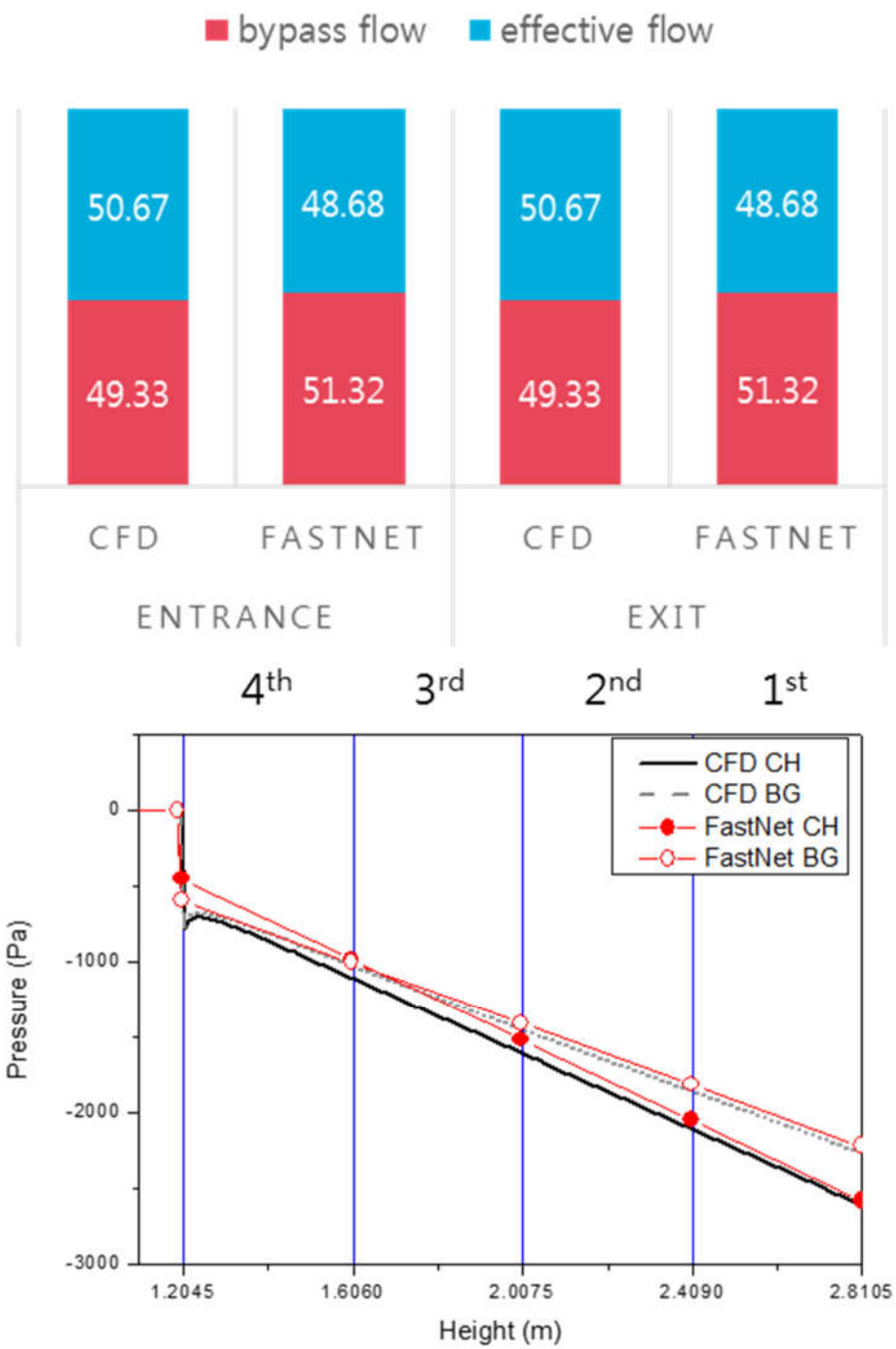

Figure 5.8 Comparative results of FastNet prediction and CFD analysis (BG6-CG0 case)

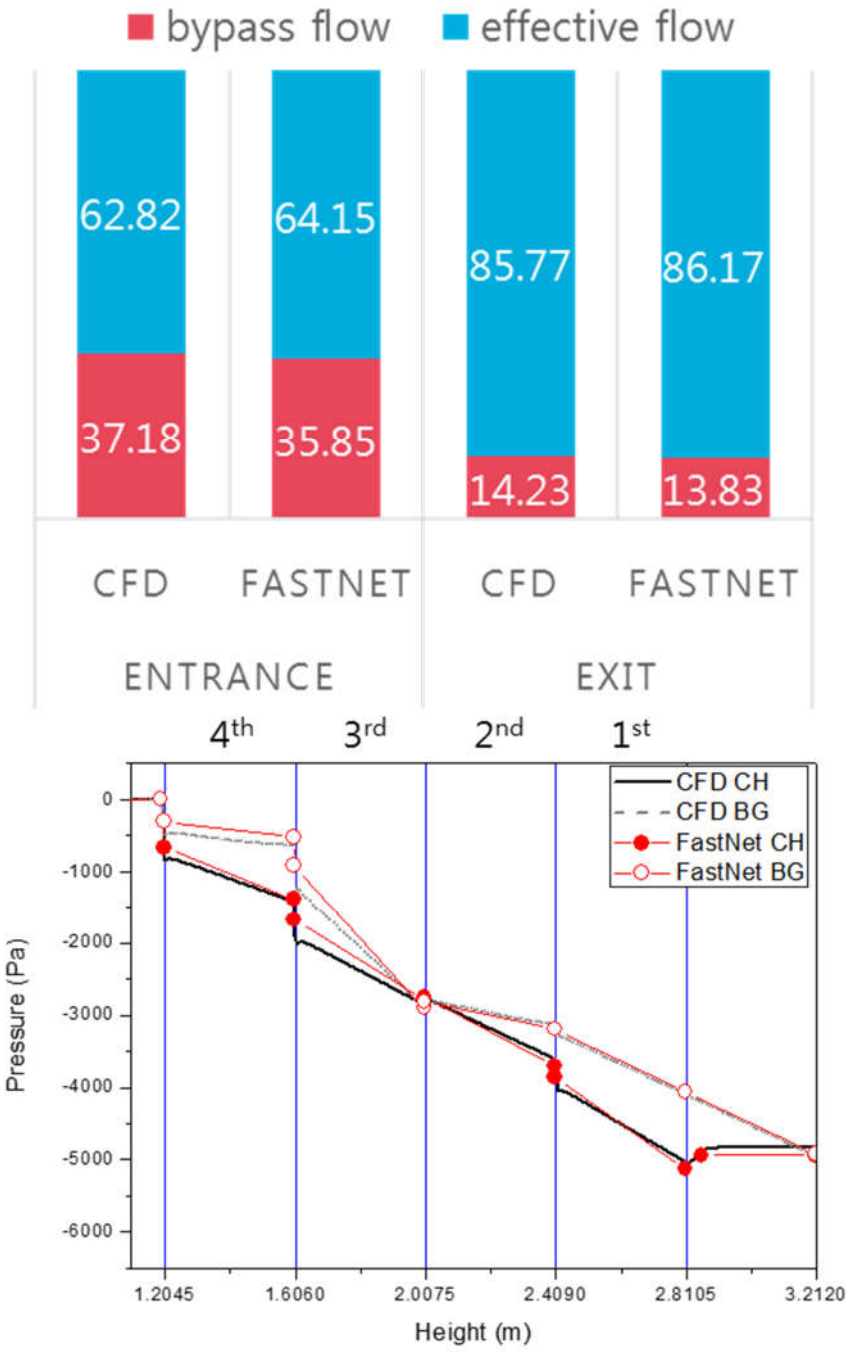

Figure 5.9 Comparative results of FastNet prediction and CFD analysis (BG6242-CG2 case)

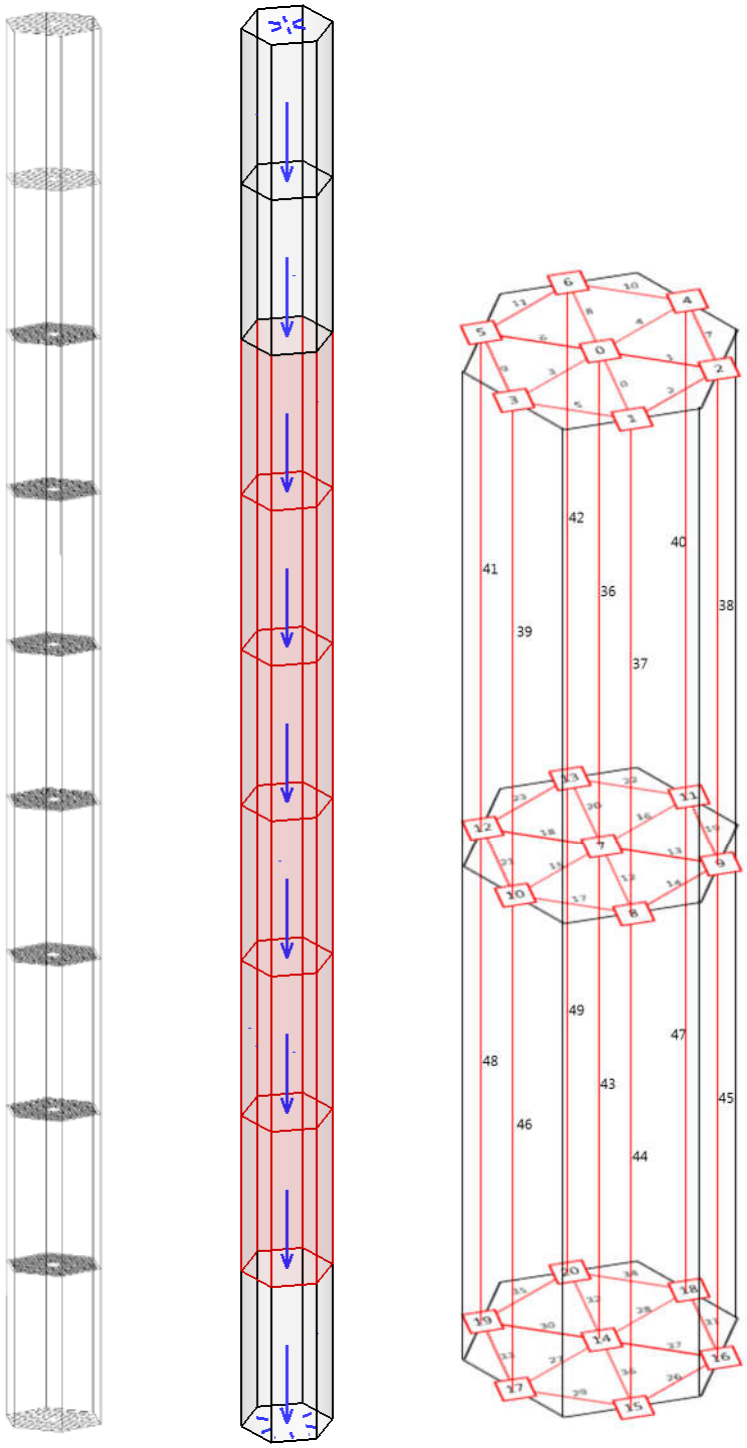

Figure 5.10 Calculation domain for CFD and network model of FastNet

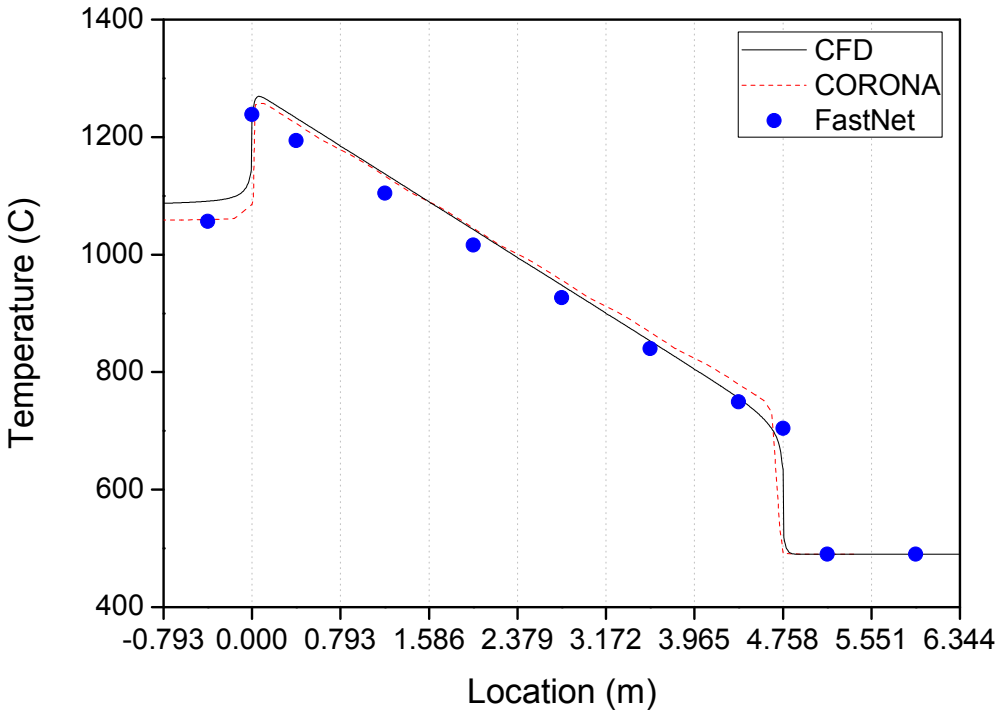

Figure 5.11 Comparison results of CFD analysis and FastNet prediction (axial distribution of hottest fuel compact)

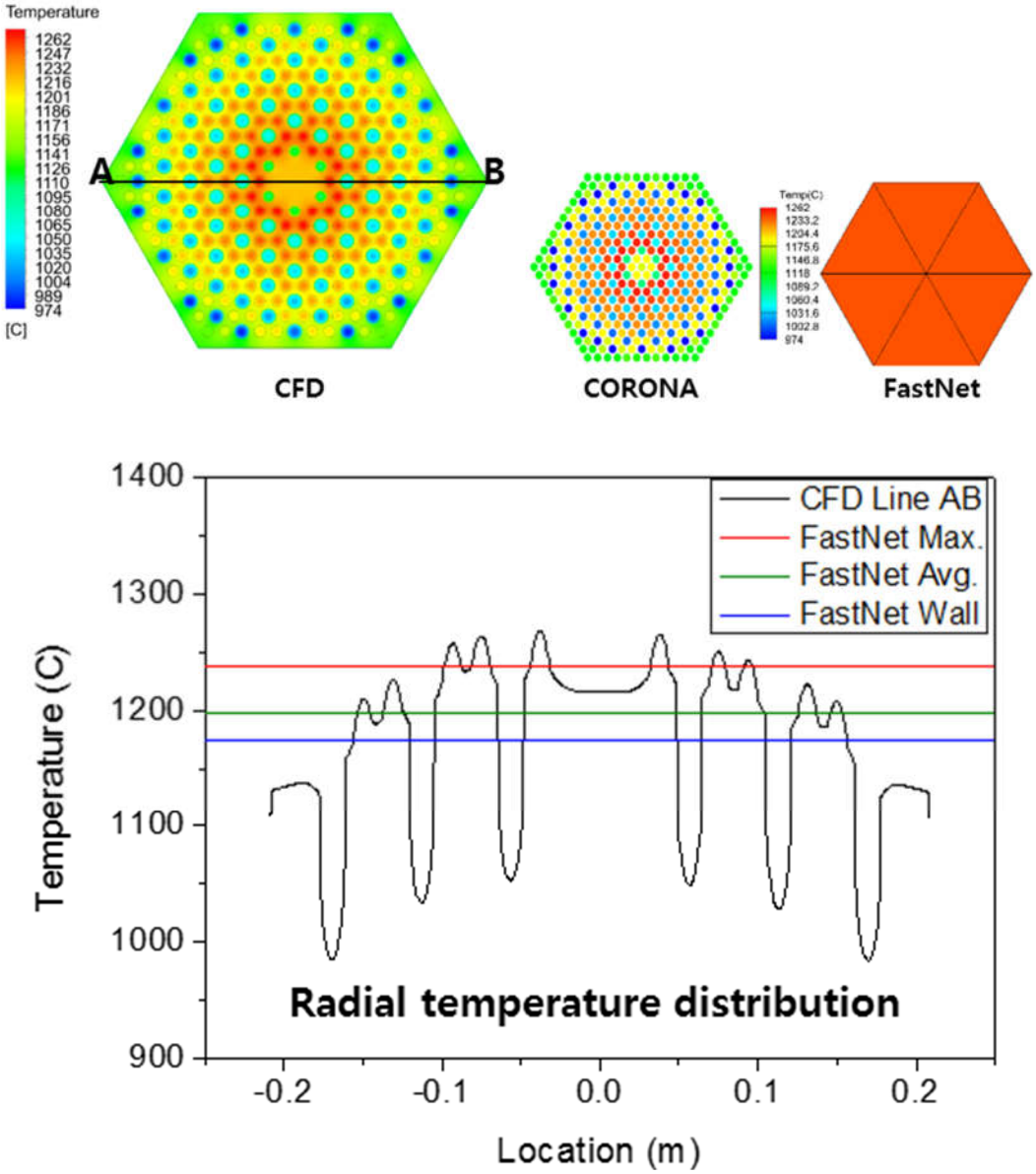

Figure 5.12 Temperature distribution at Line AB (CFD and FastNet)

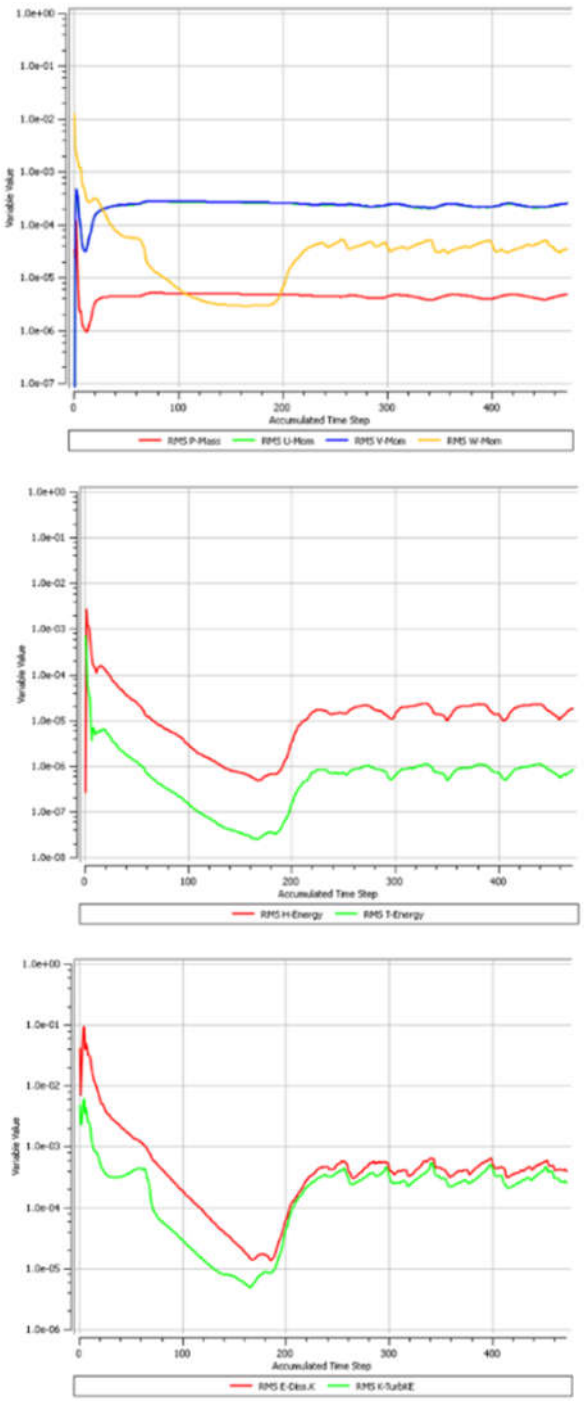

Figure 5.13 Residual graph of CFX calculation (left: momentum and mass, middle: heat transfer, right: turbulence KE)

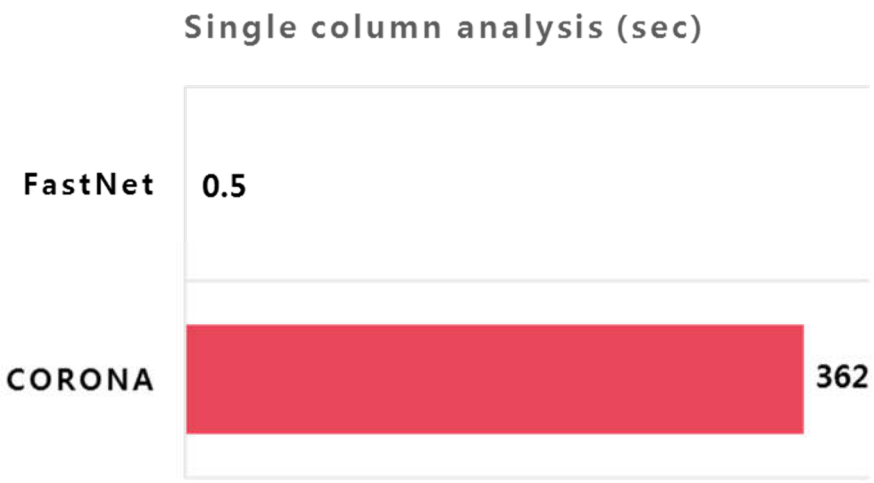

Figure 5.14 Comparison of calculation time between FastNet and CORONA

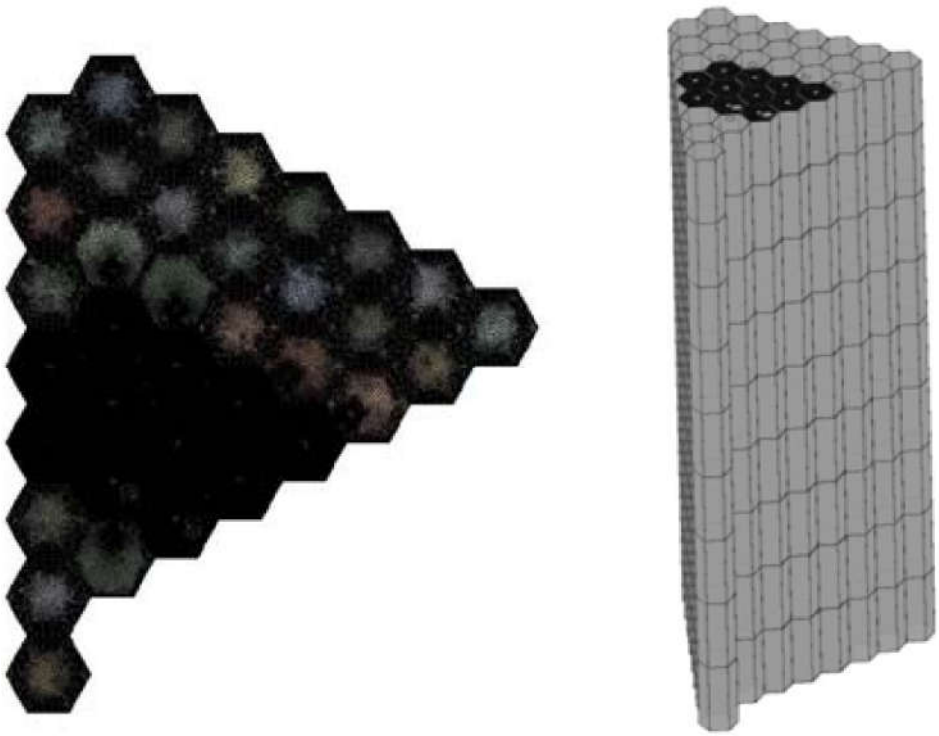

Figure 5.15 1/6 core model for CFD calculation (S.N. Lee, 2017)

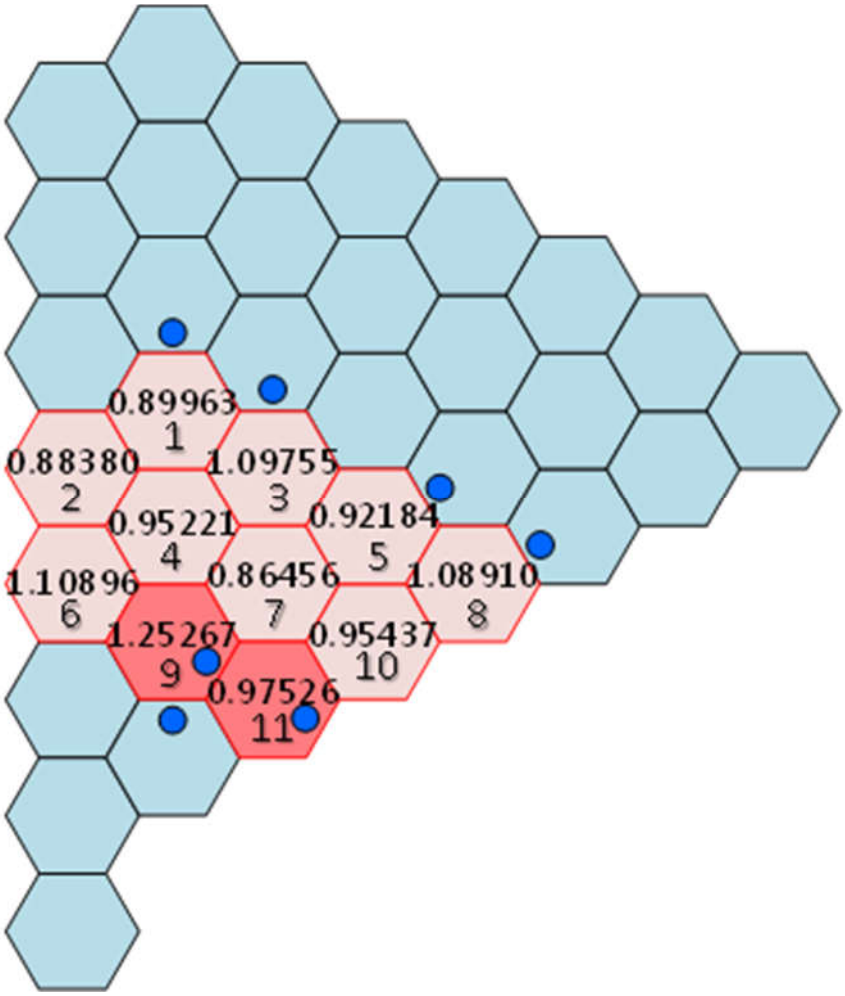

Figure 5.16 Fuel column number and power peaking factor

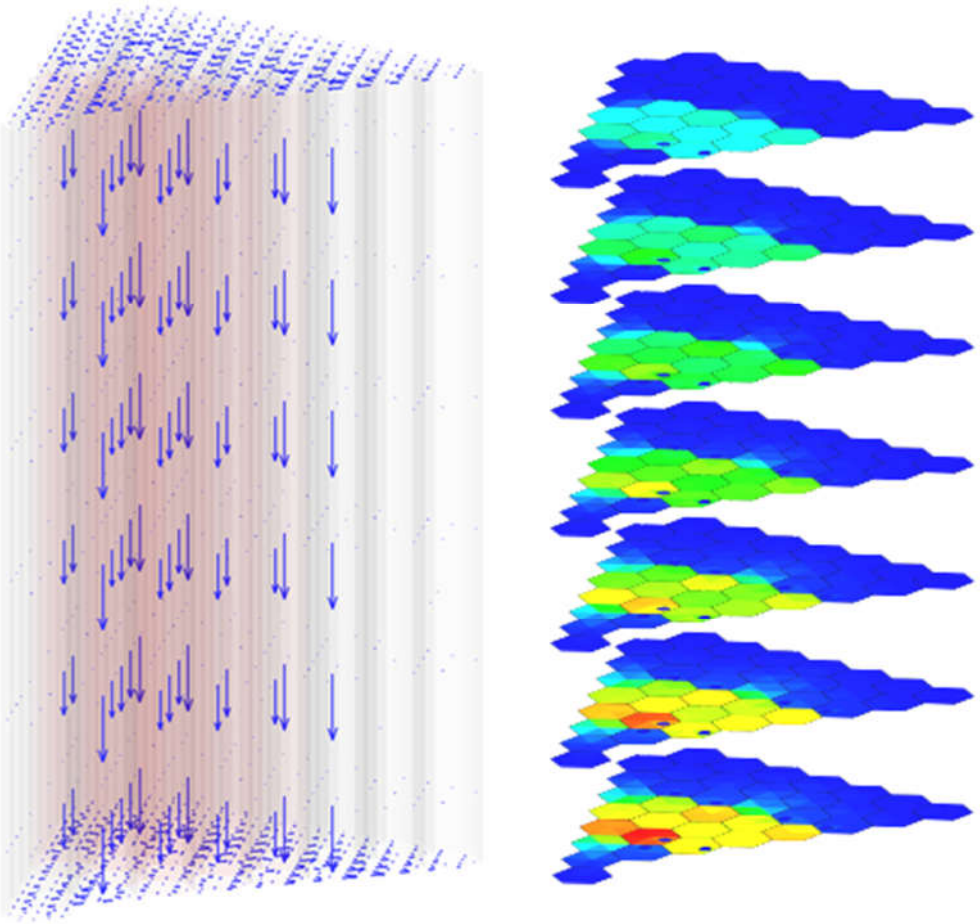

Figure 5.17 FastNet calculation results of flow distribution and temperature distribution of core

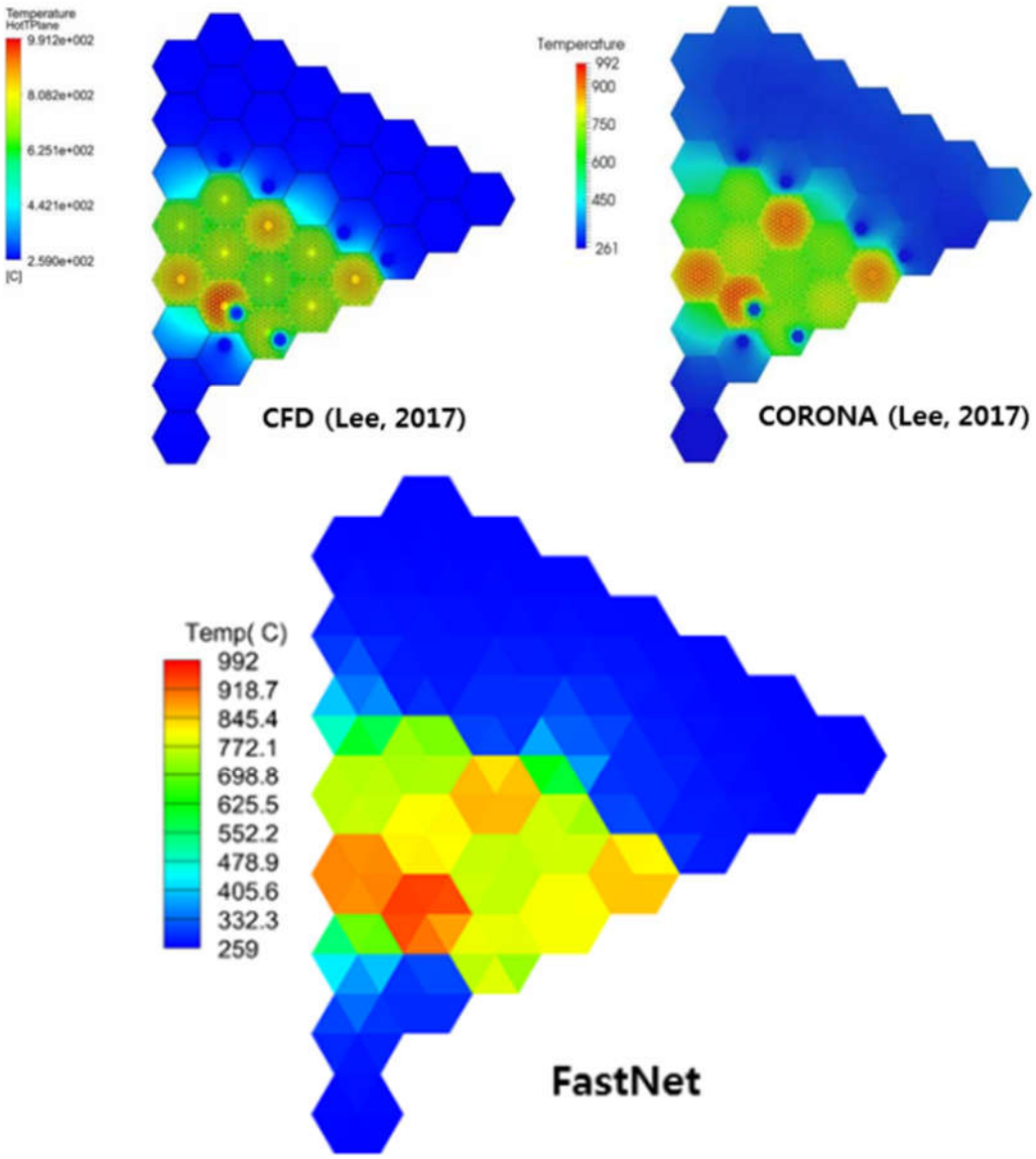

Figure 5.18 Comparison results of temperature distributions at the hot spot plane (CFX, CORONA, FastNet)

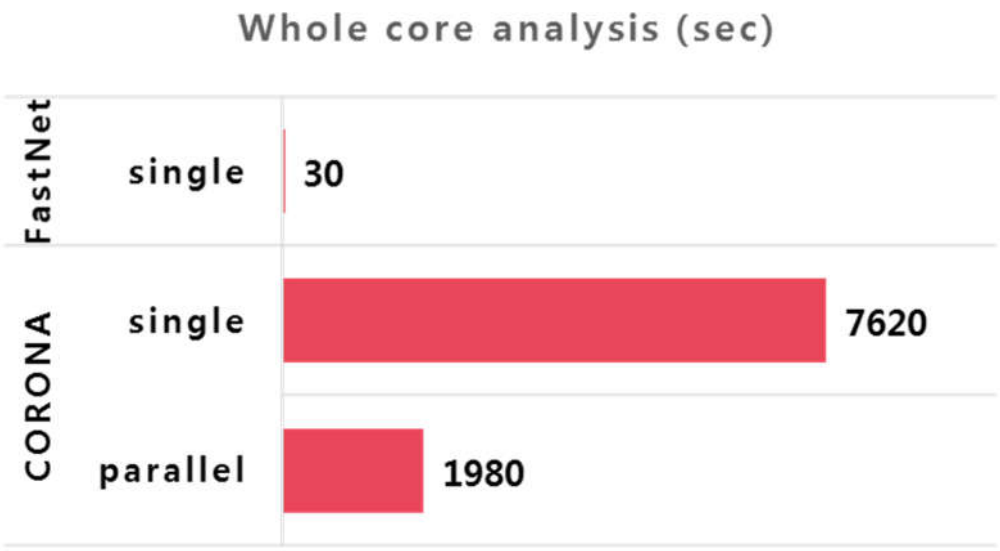

Figure 5.19 Comparison of calculation time between FastNet and CORONA for whole core simulation

Chapter 6

Conclusions

6.1 Summary

A flow network analysis code, FastNet (Flow Analysis for Steady-state Network), was developed for thermo-fluid analysis of prismatic VHTR core by using looped network analysis method. In order to analyze 3-D flow networks, a new methodology for 3-D network analysis was developed. Through this methodology, simple and fast calculations for 3-D network for the core of prismatic VHTR have become possible.

In order to find out pressure loss coefficient of the cross flow for the core of GT-MHR, the cross flow experiment was carried out. With the CFD calculation, cross reference was carried out and the applicability of the CFD simulation to the cross flow was verified. From the experimental data and CFD analysis results, the correlation of the pressure loss coefficient of the cross flow for the core of GT-MHR was developed and the developed correlation was implemented in FastNet as well as GAMMA+ and CORONA.

For the better computational accuracy of FastNet, ETC model was applied, and a maximum fuel temperature model was developed and applied to the developed code.

The developed code, FastNet, was verified and validated by comparing experimental data and other codes, such as CFD and CORONA. With the SNU multiblock experiment, the flow network analysis was validated and with the CFD and CORONA calculations, the thermo-fluid analysis capability of FastNet was verified with the single column analysis and whole core analysis. Not only the calculation results were in good agreement with other codes, but also the calculation time became much reduced.

It is highly expected that the FastNet code can contribute to assure the core thermal margin by predicting the bypass flow in the whole core of prismatic VHTR as well as the maximum fuel temperature. Thanks to its quick calculation, FastNet can be used for preliminary calculations for core of prismatic VHTR. Through the preliminary calculations with FastNet, the number of cases requiring detailed calculations with CORONA or CFD can be reduced.

6.2 Recommendations

Through the present study, followings are suggested.

- FastNet under predicts maximum temperature over other codes such as CFD and CORONA. This is a weakness of the code in terms of conservatism. A reliable model which can predict the peak temperature of the block due to the parabolic temperature distribution should be modeled. The parabolic shape of the temperature distribution in the fuel block could be a function of the bypass ratio and temperature of the bypass flow. Further study can be modeling of the prediction model for peak temperature of the fuel block.

- Since the correlation of pressure loss coefficient for cross flow lacks generality, it is inevitable to develop new correlations whenever the geometry of the fuel block changes. Even if the geometry of the fuel block changes, a correlation which can cover it should be developed in the near future. For the further study, above all, the relationship between the cross flow pressure loss coefficient and the geometry of the fuel block should be investigated in various aspects.

Nomenclature

A_{CH}	Coolant channel area
A_{CG}	Inlet cross-sectional area of the crossflow gap
A_{BG}	Bypass gap area
a	Length of one edge of the hexagonal interface at the cross gap
C_1, C_2	Empirically determined constant values for equation fitting
CR	Ratio of mass flow rate at the cross gap to outlet of the downstream block
D	Channel diameter
D_{CH}	Channel diameter at the coolant hole
D_{BGh}	Hydraulic diameter at the bypass gap
f	Friction factor through the flow channel
g	Local acceleration due to gravity
h_f	Head loss due to frictional loss
K	Pressure loss coefficient
K_{Gr}	Groehn's pressure loss coefficient
K_{Ka}	Kaburaki's pressure loss coefficient
L	Length of the flow channel
m_{cross}	Mass flow rate at the cross gap
m_{main}	Mass flow rate at the outlet of the downstream block
P	Wetted perimeter
P_{wedge}	Wetted perimeter for the wedge-shaped gap
$P_{parallel}$	Wetted perimeter for the parallel gap
Q_{jn}	Flow rate of *n-th* flow path at node *j*
Q_{kn}	Flow rate of *n-th* flow path at the *k-th* loop
R	Flow resistance of the flow path
R_{CH}	Flow resistance at the coolant hole

R_{BG}	Flow resistance at the bypass gap
R_{CG}	Flow resistance at the cross gap
Re	Reynolds number
Re_{CG}	Reynolds number at the cross gap opening
V	Velocity of air
ΔP	Pressure difference
δ	Gap width
μ	Dynamic viscosity
ρ	Density of air
$\emptyset$	Extrapolated solution by Richardson Extrapolation method

References

ANSYS Inc., “ANSYS CFX-Solver Theory Guide,” ANSYS Inc., Canonsburg, PA, 2009.

BARDINA, J.E. Huang, P.G., Coakley, T.J. “Turbulence Modeling Validation,” AIAA 97-2121, 1997.

Baxter, A., Rodriguez, C., Richards, M., Kuzminski, J., “Helium-cooled Reactor Technologies for Accelerator Transmutation of Nuclear Waste,” *Proceedings of 6th Information Exchange Meeting on Actinide and Fission Product Partitioning and Transmutation*, Madrid, Spain, 2000.

Blasius, P.R.H., "Das aehnlichkeitsgesets bei reibungsvorgangen in flüssigkeiten." *Forschungsheft* Vol. 131, pp. 1-41, 1913.

Chang, J., Kim, Y.W., Lee, K.Y., Lee, J.L., Noh, J.M., Kim, M.H., Lim, H.S., Shin, Y.J., Jung, K.D., "A study of a nuclear hydrogen production demonstration plant," *Nuclear Engineering Technology*, Vol. 39, pp. 111-122, 2007.

Davis, T., "Direct Methods for Sparse Linear Systems," *SIAM*, 2006, ISBN: 0898716136, LC: QA188.D386

Fluent Inc., “GAMBIT 2.2 User’s Guide” Fluent Inc., Lebanon, NH, 2004.

Gauthier, J.C., Brinkmann, G., Copsey, B., Lecomte, M., “ANTARES: The

HTR/VHTR project at Framatome ANP," *Nuclear Engineering and Design*, Vol. 236, pp. 526-533, 2006.

General Atomics, "Graphite Design Handbook," DOE-HTGR-88111, Rev. 0, 1988.

General Atomics, "GT-MHR design, performance, and safety," GA-A21924, 1994.

Groehn, H.G., "Estimate of Cross Flow in High Temperature Gas-cooled Reactor Fuel Blocks," *Heat Transfer and Fluid Flow, Nuclear Technology*, Vol. 5, pp. 392-400, 1982.

Haaland, S.E., "Simple and Explicit Formulas for the Friction Factor in Turbulent Flow". *Journal of Fluids Engineering*, Vol. 105 (1). pp. 89-90, 1983.

Han, J.C., Driscoll, M.J., Todreas, N.E, "Effective Thermal Conductivity of Prismatic MHTGR Fuel", MIT, MIT-ANP;TR-005, 1989.

Idelchik, I.E., "Handbook of Hydraulic Resistance (3rd ed.)," pp. 75-237, Begel House, New York. 1996.

INEEL, "Design Features and Technology Uncertainties for the Next Generation Nuclear Plant," INEEL/EXT-04-01816, 2004.

INEEL, “RELAP5-3D© Code Manual,” Vol. 1–5, Rev. 3, INEELEXT-98-00834, 2009.

Johnson, R.W., Sato, H., "Bypass flow computations using a one-twelfth symmetric sector for normal operation in a 350 MWth prismatic VHTR," *Nuclear Engineering and Design*, Vol. 251, pp. 84-91, 2012.

Kaburaki, H., Takizuka, T., "Crossflow characteristics of HTGR fuel blocks." *Nuclear Enineering and Design*, Vol. 120, pp. 425-434, 1990.

Kanjanakijkasem, W., Wang, H., Dominguez-Ontiveros, E., Hassan, Y.A., "Experimental and CFD studies of the bypass flow in a prismatic core of VHTR using a small-scale model." *Progress in Nuclear Energy*, Vol. 91, 223-235, 2016.

Kim, M.H., Lim, H.S., 2011. Evaluation of the influence of bypass flow gap distribution on the core hot spot in a prismatic VHTR core. *Nuclear Engineering and Design*, Vol. 241, pp. 3076-3085.

Langtry, R.B., Menter, F.R., "Transition modeling for general CFD applications in aeronautics," Proceedings of 43rd AIAA Aerospace Sciences Meeting, Reno, NV, USA, 2005.

Lee, J.H., Yoon, S.J., Cho, H.K., Jae, M., Park, G.C., "Experimental investigation and CFD analysis on cross flow in the core of PMR200," *Annals of Nuclear Energy*, Vol. 83, pp. 422-435, 2015.

Lee, J.H., Yoon, S.J., Park, J.W., Park, G.C., “Development of flow network analysis code for block type VHTR core by linear theory method,” *Proceedings of ICAPP ‘12*, Chicago, IL, USA, 2012.

Lim, H.S., “General analyzer for multi-component and multi-dimensional transient application, GAMMA+ 1.0 volume II: theory manual,” KAERI/TR-5728/ 2014, 2014.

Lim, H.S., NO, H.C., “GAMMA multidimensional multi-component mixture analysis to predict air ingress phenomena in an HTGR,” *Nuclear Science and Engineering*, Vol. 152, pp. 87-97i 2006.

Maruyama, S., Fujimoto, N., Kiso, Y., Murakami, T., Sudo, Y., “Verification of Combined Thermal–Hydraulic and Heat Conduction Analysis Code. FLOWNET/TRUMP,” JAERI-M pp. 88-173, 1988.

MAXWELL, J.C. “A Treatise on Electricity and Magnetism, 1st ed.,” Vol. 1, Chap. 9, pp. 435–441, Clarendon Press, Oxford, United Kingdom, 1873.

McCARTNEY, L.N., KELLY, A., “Maxwell’s FarField Methodology Applied to the Prediction of Properties of Multi-Phase Isotropic Particulate Composites,” *Proceedings of the Royal Society A*, Vol. 464, pp. 423-446, 2007.

Menter, F.R. “Two-Equation Eddy-Viscosity Turbulence Models for Engineering Applications,” *AIAA Journal*, Vol. 32, No.8, pp. 1598-1605, 1994.

Menter, F.R., Kuntz, M., R. Langtry, “Ten Years of Industrial Experience with the SST Turbulence Model,” *Turbulence, Heat and Mass Transfer*, Vol. 4, 2003.

Moody, L.F., “Friction factors for pipe flow,” *Transactions of the American Society of Mechanical Engineers*, Vol. 66, pp. 671-684, 1944.

Olson, H.G., Brey, H.L., Warembourg, D.W., “The Fort St. Vrain high temperature gas-cooled reactor: X. Core temperature fluctuations.” *Nuclear Engineering and Design*, 72, 125–137, 1982.

Paul, C.R., “Fundamentals of Electric Circuit Analysis,” Ch.2, Jonh Wiley & Sons, New Jersey, 2000.

Richardson, L.F., “The approximate arithmetical solution by finite differences of physical problems involving differential equations, with an application to the stresses in a masonry dam,” *Philosophical Transactions of The Royal Society A Mathematical Physical and Engineering Sciences*, Vol. 210, pp. 307-357, 1910.

Richardson, L.F., Gaunt, J.A., “The deferred approach to the limit,” *Philosophical Transactions of The Royal Society A Mathematical Physical and Engineering Sciences*, Vol. 226, pp. 299-361, 1927.

Sato, H., Johnson, R., Schultz, R., “Computational fluid dynamic analysis of core bypass flow phenomena in a prismatic VHTR,” *Annals of Nuclear Energy*, Vol. 37,

pp. 1172–1185. 2010.

Selengut, D.S., “Diffusion Coefficients for Heterogeneous System,” *Transactions of the American Nuclear Society*, Vol. 4, pp. 398, 1961.

Shin D.H., Yoon, S.J. Cho, H.K. Park, G.C., “Development of effective thermal conductivity models for reserve shutdown control fuel block of prismatic HTGR for hydrogen production,” *International Journal of Hydrogen Energy*, 2017, http://dx.doi.org/10.1016/j.ijhydene.2017.04.128

Shin, D.H., Yoon, S.J., Cho, H.K., Park, G.C., “Analytical study on the effective thermal conductivity of VHTR fuel block geometry with multiple cylindrical holes,” *Nuclear Technology*, Vol. 191, pp. 213-222, 2015.

Strydom, G. Epiney, A.S. Alfonsi, A., Rabiti, C., “Comparison of the PHISICS/RELAP5-3D ring and block model results for phase I of the OECD/NEA MHTGR-350 Benchmark,” *Nuclear Technology*, Vol. 193, pp.15-35, 2016.

Tak, N.I., Lee, S.N., Kim, M.H., Lim, H.S., Noh, J.M., “Development of a core thermo-fluid analysis code for prismatic gas cooled reactors.” *Nuclear Engineering Technology*, Vol. 46, No. 5, pp. 641-654, 2014.

Tung, Y.H., Johnson, R.W., Sato, H., “Effects of graphite surface roughness on bypass flow computations for an HTGR,” *Nuclear Engineering and Design*, Vol. 252, pp. 78–87, 2012.

Vilim, R.B., “GAS-NET: a two-dimensional network code for prediction of core flow and temperature distribution in the prismatic gas reactor,” *Proceedings of ICAPP-07*, Nice, France, 2007.

Wang, H., Dmingues-Ontiveros, E., Hassan, Y.A., “Computational fluid dynamics analysis of core bypass flow and crossflow in a prismatic very high temperature gas-cooled nuclear reactor based on a two-layer block model,” *Nuclear Engineering and Design*, Vol. 268, pp. 64-76, 2014.

Wang, H., Hassan, Y.A., Dominguez-Ontiveros, E., “Experimental study of core bypass flow in a prismatic VHTR based on a two-layer block model,” *Nuclear Engineering and Design*, Vol. 306, pp. 98-107. 2016.

Wood, D.J. and Charles, C.O., “Hydraulic Network Analysis using Linear Theory, Journal of the Hydraulic Division,” Vol. 98, p. 1157-1170, ASCE, New York, US, 1972.

Yoon, S.J., Jin, C.Y., Lee, J.H., Kim, M.H., Park, G.C., “Study on the flow distribution in prismatic VHTR core with a multi-block experiment and CFD analysis,” *Nuclear Engineering and Design*, Vol. 241, pp. 5174-5182. 2011.

Yoon, S.J., Lee, J.H., Kim, M.H., Park, G.C., “The effects of cross flow gap and axial bypass gap distribution on the flow characteristics in prismatic VHTR core.” *Nuclear Engineering and Design*, Vol. 250, pp. 465-479. 2012.

Appendix A

Uncertainty Analysis for the Cross Flow Experiment

The uncertainty analysis was conducted to provide the reliability of the experiment. For the measured main flow rate and cross flow rate is provided as follows.

The main, inlet and cross flow rates were obtained by

$$m_{main} = V_{main} \cdot \rho \cdot A$$
$$m_{inlet} = V_{inlet} \cdot \rho \cdot A$$
$$m_{cross} = m_{main} - m_{inlet}$$

where, $V = 1.277\sqrt{\frac{\Delta P}{K}\frac{1.013}{P}\frac{T}{288}\frac{1}{\rho}}$, ΔP is pressure difference, K = 1.8, P is room pressure, T is room temperature, and ρ is density of the air, respectively. Since the K factor and the density of the air can be considered as constant values, the uncertainty of the main mass flow rate becomes

$$U_{m_{main}}^2 = \left(\frac{\partial m_{main}}{\partial \Delta P} U_{\Delta P}\right)^2 + \left(\frac{\partial m_{main}}{\partial P} U_P\right)^2 + \left(\frac{\partial m_{main}}{\partial T} U_T\right)^2$$

The uncertainty of the pressure difference can be expressed as

$$U_{\Delta P} = \sqrt{\left(\varepsilon_{\Delta P}\right)^2 + \left(\sigma_{\Delta P}\right)^2} .$$

where $\varepsilon_{\Delta P}$ = 2 Pa is bias error (0.04% of span) of the measuring instrument and $\sigma\Delta P \approx 0.024 \cdot \Delta P$ is precision error which is standard deviation of the measured data. Hence, the uncertainty of the pressure difference can be expressed as

$$U_{\Delta P} \approx \sqrt{\left(2\right)^2 + \left(0.024 \cdot \Delta P\right)^2} .$$

Therefore, at the minimum flow rate condition (0.1 kg/s of m_{main}) and the maximum flow rate condition (1.35 kg/s of m_{main}), the uncertainties are approximately 2.01 Pa (20.1%) and 43.2 Pa (2.51%), respectively.

The uncertainty of the room pressure can be expressed as

$$U_P = \sqrt{\left(\varepsilon_P \cdot \Delta P\right)^2 + \left(\sigma_P\right)^2} = 0.0016 \cdot P$$

where ε_P = 0.001 is bias error of 0.1% of the measuring instrument and $\sigma_P \approx 0.0012 \cdot \Delta P$ is precision error which is standard deviation of the measured data.

The uncertainty of the room temperature can be written as

$$U_T = \sqrt{\left(\varepsilon_T \cdot \Delta P\right)^2 + \left(\sigma_T\right)^2} = 0.0075 \cdot T$$

where ε_T = 0.0073 is bias error of 0.1% of the measuring instrument and $\sigma_T \approx$

$0.0018 \cdot \Delta T$ is precision error which is standard deviation of the measured data. Therefore, the uncertainty of the main flow rate can be rewritten as

$$U_{m_{main}}^2 = \left(\frac{1}{2} \cdot \frac{U_{\Delta P}}{\Delta P} \cdot m_{main}\right)^2 + \left(\frac{1}{2} \cdot \frac{U_P}{P} \cdot m_{main}\right)^2 + \left(\frac{1}{2} \cdot \frac{U_T}{T} \cdot m_{main}\right)^2$$
$$\approx \left(\frac{1}{2} \cdot \frac{0.024 \cdot \Delta P}{\Delta P} \cdot m_{main}\right)^2 + \left(\frac{1}{2} \cdot \frac{0.016 \cdot P}{P} \cdot m_{main}\right)^2 + \left(\frac{1}{2} \cdot \frac{0.0075 \cdot T}{T} \cdot m_{main}\right)^2$$

At the minimum flow rate condition (0.1 kg/s of m_{main}) and the maximum flow rate condition (1.35 kg/s of m_{main}), the uncertainties are approximately 0.01 kg/s (10% of m_{main}) and 0.023 kg/s (1.67% m_{main}), respectively.

On the other hand, the uncertainty of the cross flow can be expressed as

$$U_{m_{cross}} = \sqrt{\left(U_{m_{main}}\right)^2 + \left(U_{m_{inlet}}\right)^2}$$

At the minimum flow rate condition (0.1 kg/s of m_{main}) and the maximum flow rate condition (1.35 kg/s of m_{main}), the uncertainties are approximately 0.014 kg/s (14% of m_{main}) and 0.032 kg/s (2.4% of m_{main}), respectively.

And the ratio of the cross flow is defined as

$$CR = \frac{m_{cross}}{m_{main}}$$

Hence, the uncertainty of the ratio of the cross flow becomes

$$U_{CR} = CR \cdot \sqrt{U_{m_{cross}}{}^2 + U_{m_{main}}{}^2}$$

At the minimum flow rate condition (0.1 kg/s of m_{main}) and the maximum flow rate condition (1.35 kg/s of m_{main}), the uncertainties are approximately 17.5% and 2.90%, respectively. Therefore, we estimate the maximum uncertainties of main mass flow rates and cross mass flow rates as 0.023 kg/s and 0.032 kg/s, respectively.

The readings of inlet and outlet flow rates in 6 mm wedge-shaped gap were summarized as Table A.1.

Table A.1 Readings of inlet and outlet flow rate.

Outlet flow rate (kg/s)	Inlet flow rate (kg/s)	Cross flow (kg/s)	Error (kg/s)
1.3370	1.1335	0.2035	0.0321
1.2447	1.0541	0.1906	0.0305
1.1591	0.9842	0.1748	0.0291
1.0949	0.9293	0.1656	0.0281
1.0270	0.8693	0.1578	0.0270
0.9740	0.8243	0.1497	0.0262
0.9379	0.7943	0.1437	0.0257
0.9039	0.7656	0.1383	0.0252
0.8753	0.7380	0.1374	0.0247
0.8431	0.7130	0.1302	0.0243
0.8113	0.6842	0.1270	0.0238
0.7643	0.6463	0.1180	0.0232
0.7155	0.6038	0.1116	0.0225
0.6914	0.5825	0.1089	0.0222
0.6618	0.5597	0.1021	0.0219
0.6256	0.5296	0.0960	0.0214
0.5913	0.4993	0.0919	0.0210
0.5677	0.4788	0.0889	0.0208
0.5363	0.4520	0.0843	0.0204
0.5036	0.4252	0.0784	0.0201
0.4814	0.4063	0.0752	0.0198
0.4637	0.3909	0.0728	0.0197
0.4459	0.3746	0.0713	0.0195
0.4230	0.3550	0.0680	0.0193
0.3794	0.3197	0.0598	0.0189
0.3128	0.2630	0.0498	0.0184
0.2481	0.2078	0.0403	0.0180
0.1831	0.1531	0.0300	0.0177
0.1250	0.1047	0.0203	0.0175

Appendix B

Flow Direction Dependency of Cross Flow Loss Coefficient

Since the flow loss coefficient may vary depending on the flow direction of the cross flow, confirmation of these phenomena is required. Because the applicability of CFD code for cross flow phenomena was verified in Chapter 3, the CFD code can be used to confirm these phenomena. Fig. A.1 shows the conditions of CFD analysis for two opposite flow direction cases. The conditions of the left side are the same calculation conditions as the experimental conditions, of which cross flow direction is inflow and the cross flow direction of right side is outflow. Although the direction of the cross flow changes, there is no significant difference in the pressure loss coefficient as seen in Fig. A.2. The loss coefficient is defined by

$$K = \frac{\Delta P}{\frac{1}{2}\rho V^2}.$$

ΔP is the pressure difference between outside of the cross gap and inside of coolant channel and V is the averaged velocity at the cross flow gap opening.

And therefore, the cross flow loss coefficient correlation can be used regardless of the flow direction as

$$K = \frac{37 \cdot \lambda}{\delta \mathrm{Re}_{Gap}} + 3.5.$$

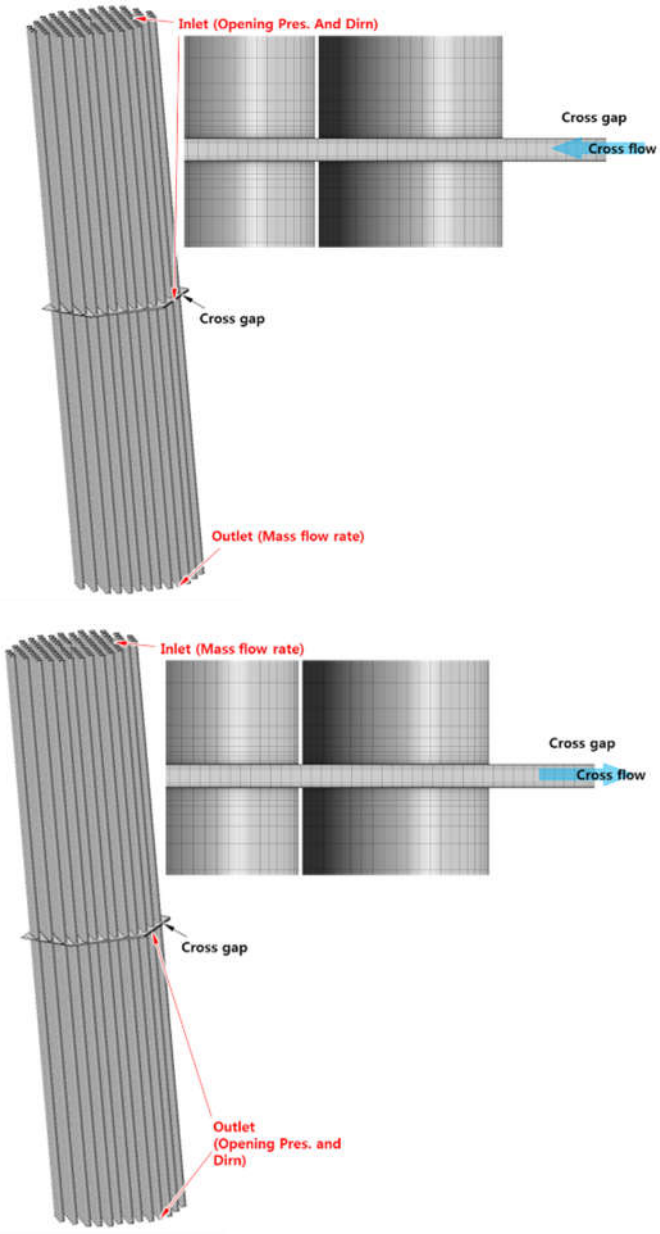

Figure A.1 Two different conditions with the opposite direction of cross flow

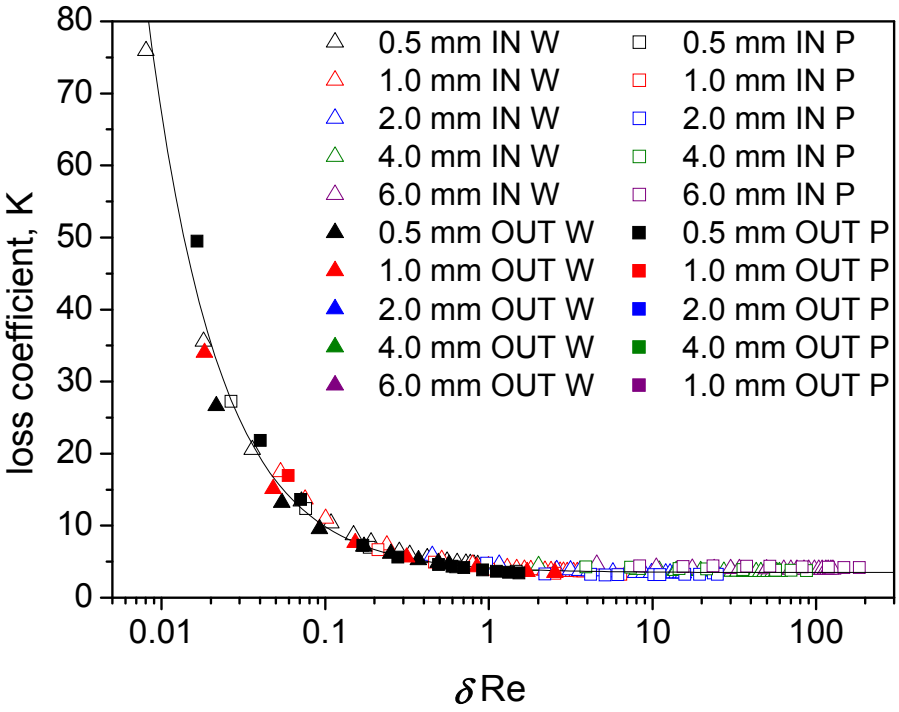

Figure A.2 Pressure loss coefficient for cross flow

Appendix C

Friction Factor Model Sensitivity Test

Friction factor used in this study is Haaland equation. However, since there is some discrepancy among friction factor models, the friction factor model sensitivity test was conducted.

To confirm the error of the model, 5 other models were compared as shown in Fig A.3.

Tested models are as follows.

$$f = 0.316\,\mathrm{Re}^{-\frac{1}{4}} \quad \text{(Blasius, 1913)}$$

$$\frac{1}{f^{1/2}} = -1.8\log\left[\frac{6.9}{\mathrm{Re}_d} + \left(\frac{\varepsilon/d}{3.7}\right)^{1.11}\right] \quad \text{(Haaland, 1983)}$$

$$\frac{1}{f^{1/2}} = -2\log\left(\frac{5.74}{\mathrm{Re}^{0.9}} + \frac{\varepsilon/d}{3.7}\right) \quad \text{(Swamee-Jain, 1976)}$$

$$\frac{1}{f^{1/2}} = 1.8\log\left(\frac{\mathrm{Re}}{0.135\,\mathrm{Re}(\varepsilon/d) + 6.5}\right) \quad \text{(Round, 1980)}$$

$$f = \frac{6.4}{\left(\ln(\mathrm{Re}) - \ln\left(1 + 0.01\mathrm{Re}\frac{\varepsilon}{d}\left(1 + 10\sqrt{\frac{\varepsilon}{d}}\right)\right)\right)^{2.4}} \quad \text{(Avci and Karagoz, 2009)}$$

$$f = 1.613\left[\ln\left(0.234\varepsilon^{1.1007}\right) - \frac{60.525}{\mathrm{Re}^{1.1105}} + \frac{56.291}{\mathrm{Re}^{1.0712}}\right]^{-2} \quad \text{(Fang, 2011)}$$

The tested Reynolds number range is from 4000 to 60000. As seen in Fig. A.3, the maximum difference between Haaland equation and Blasius equation is 2.4%. Furthermore, the maximum difference with other 4 equations is 1.7%. Therefore, it can be said that the error from the friction factor model is under 2%.

In addition to this, the roughness sensitivity test was carried out. The roughness of the graphite is usually 2 μm RMS and that of aluminum is 5 μm RMS. When Reynolds number is 23000 (Reynolds number at the coolant channel for normal operation condition), the friction factors are 0.0251 and 0.0255 as tabulated in Table A.1. The error from the roughness is approximately 1.5%. In FastNet calculation, roughness was set to 2 μm RMS. When the roughness is 0, since the difference is only 0.89%, it can be said that the error from the roughness is insignificant.

Table A.2 Friction factor according to roughness

Roughness (μm)	Friction factor	Difference
0	0.0249	0.89%
2	0.0251	-
5	0.0255	1.5%

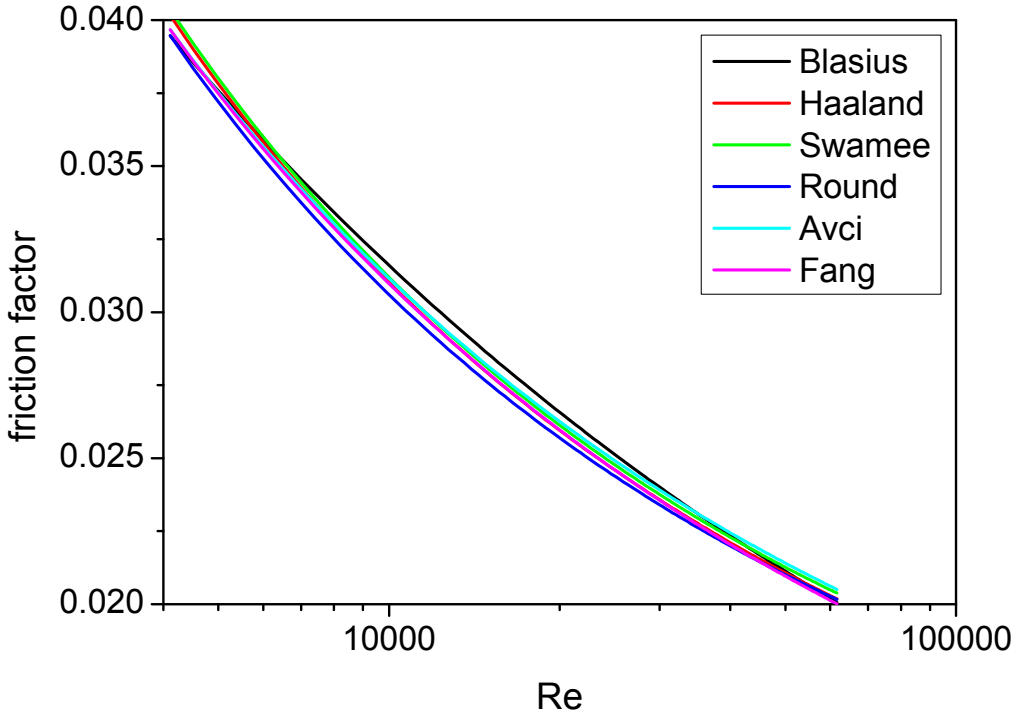

Figure A.3 Comparison of 6 friction factor equations

Appendix D

y^+ Sensitivity Test for Gamma-Theta Model

For and accurate analysis for flow separation, y^+ must be less than 1. Since the y+ values for CFD analysis in the cross flow experimental study are greater than 1, the y^+ sensitivity test was conducted. The 2 mm parallel cross gap with 0.5 kg/s main flow rate case (Reynolds number is 20550) was tested. The y+ value and the other important variables are summarized in Tables A.2 and A.3.

As shown in Fig. A.4, both cases have similar turbulence intermittency. Most of the cross gaps, 1 in the coolant channel, 2 in the coolant hole closest to the exterior, and 0 in the center of the cross gap. It can be seen that all except the central part of the cross gap is analyzed as turbulence. Fig. A.5 shows a similar tendency in the radial direction, but the laminar region is predicted more widely in the case where y^+ is smaller than 1. The velocity distribution in axial direction also show similar results in both cases as plotted in Fig. A.6. The velocity distributions in radial direction also have similar results in both cases as presented in Fig. A.7. The maximum velocity is observed in the cross flow near the outermost coolant hole, and the maximum velocity difference between the two cases is approximately 3%. The radial pressure distributions in the cross gap are very similar in both cases as seen in Fig. A. 8. The velocity streamline is also similar to each other as represented in Fig. A.9. In both cases, the cross flow pressure loss coefficients are calculated to be 3.4 and 3.6, respectively. When this is applied to the correlation of the cross flow loss coefficient, it is estimated to be 3.55. Hence it can be said that the CFD analysis

with relatively high y+ is also quite reliable.

Table A.3. y^+ values for two different mesh cases

Case	Turbulent model	y^+	
		Coolant channel	Cross gap
High y^+	SST, Gamma-Theta model	3.7	2.7
Low y^+	SST, Gamma-Theta model	0.72	0.77

Table A.4 Variables for two different mesh cases

Case	Cross flow rate (kg/s)	Pressure difference between outside of gap and inside of coolant hole (Pa)	Loss coefficient
High y^+	0.0571	-759	3.4
Low y^+	0.0549	-746	3.6

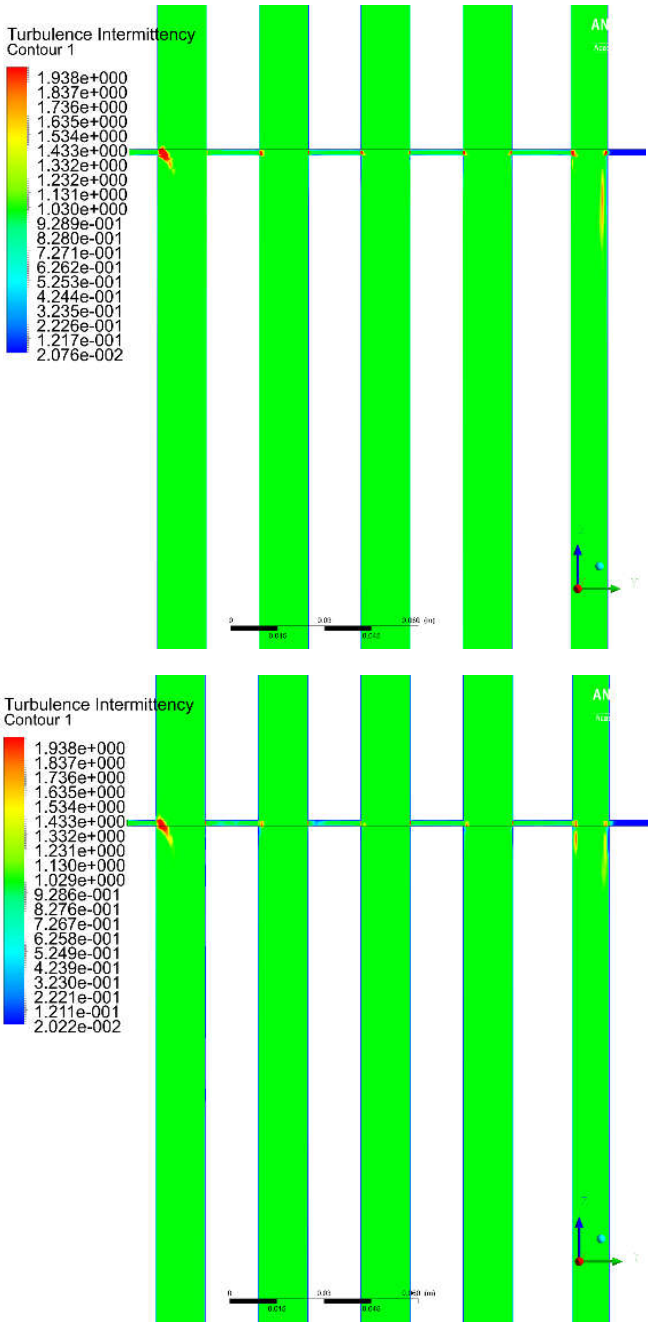

Figure A.4 Turbulent intermittency distributions in axial direction (top: high y^+, bottom: low y^+)

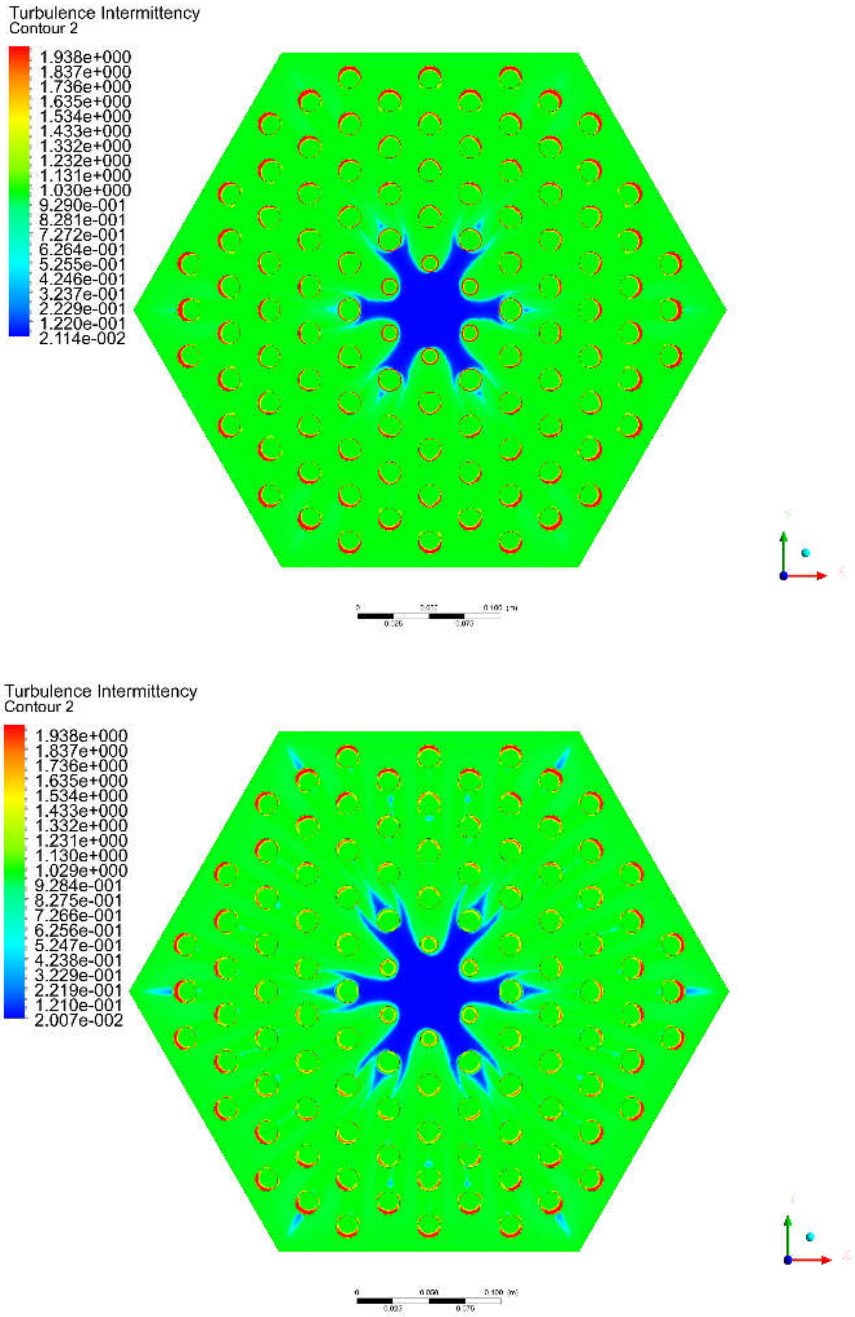

Figure A.5 Turbulent intermittency distribution in radial direction (top: high y^+, bottom: low y^+)

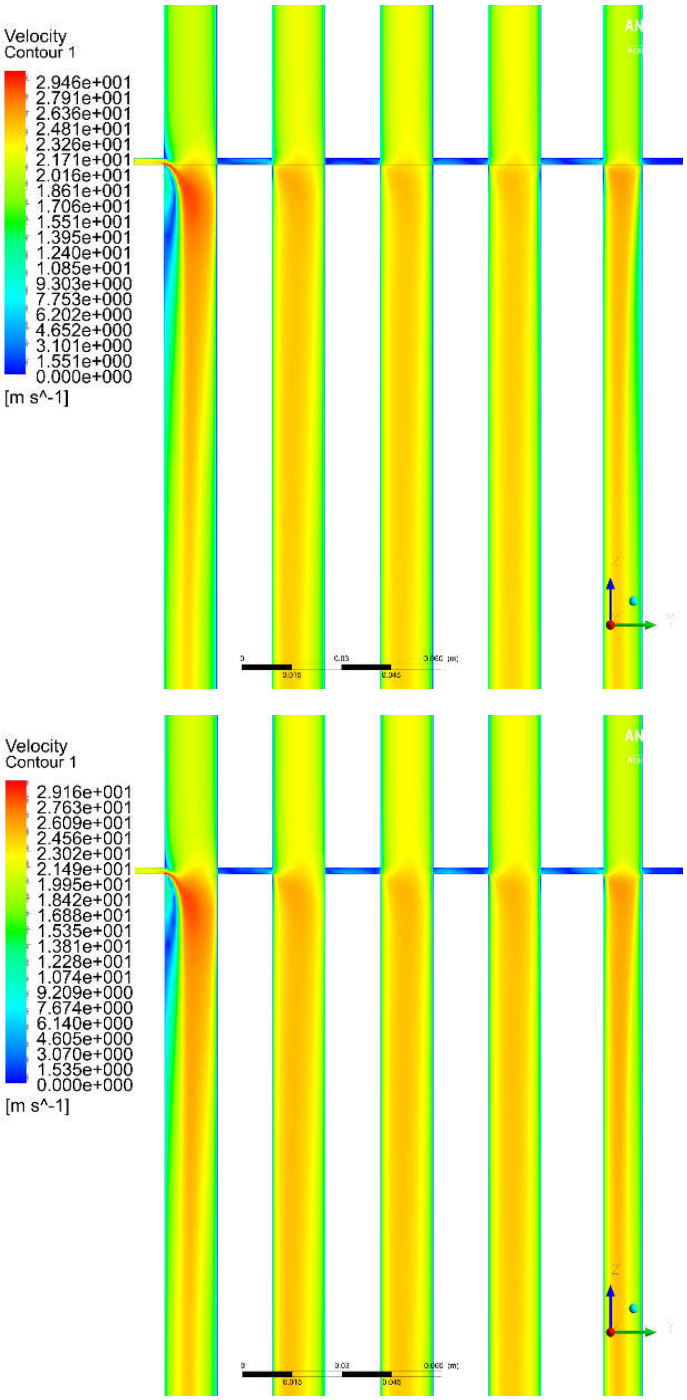

Figure A.6 Velocity distribution in axial direction
(top: high y^+, bottom: low y^+)

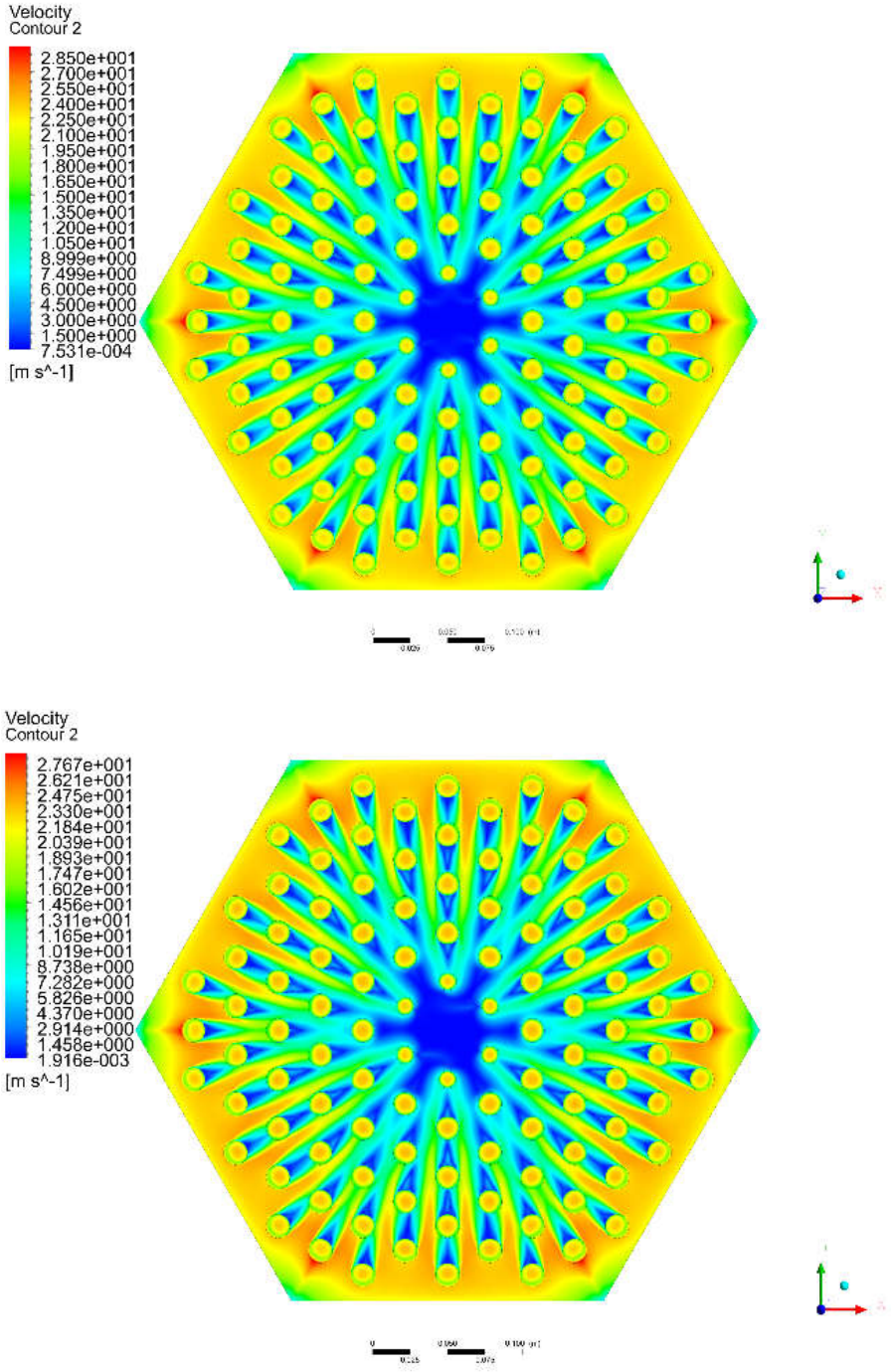

Figure A.7 Velocity distribution in radial direction
(top: high y^+, bottom: low y^+)

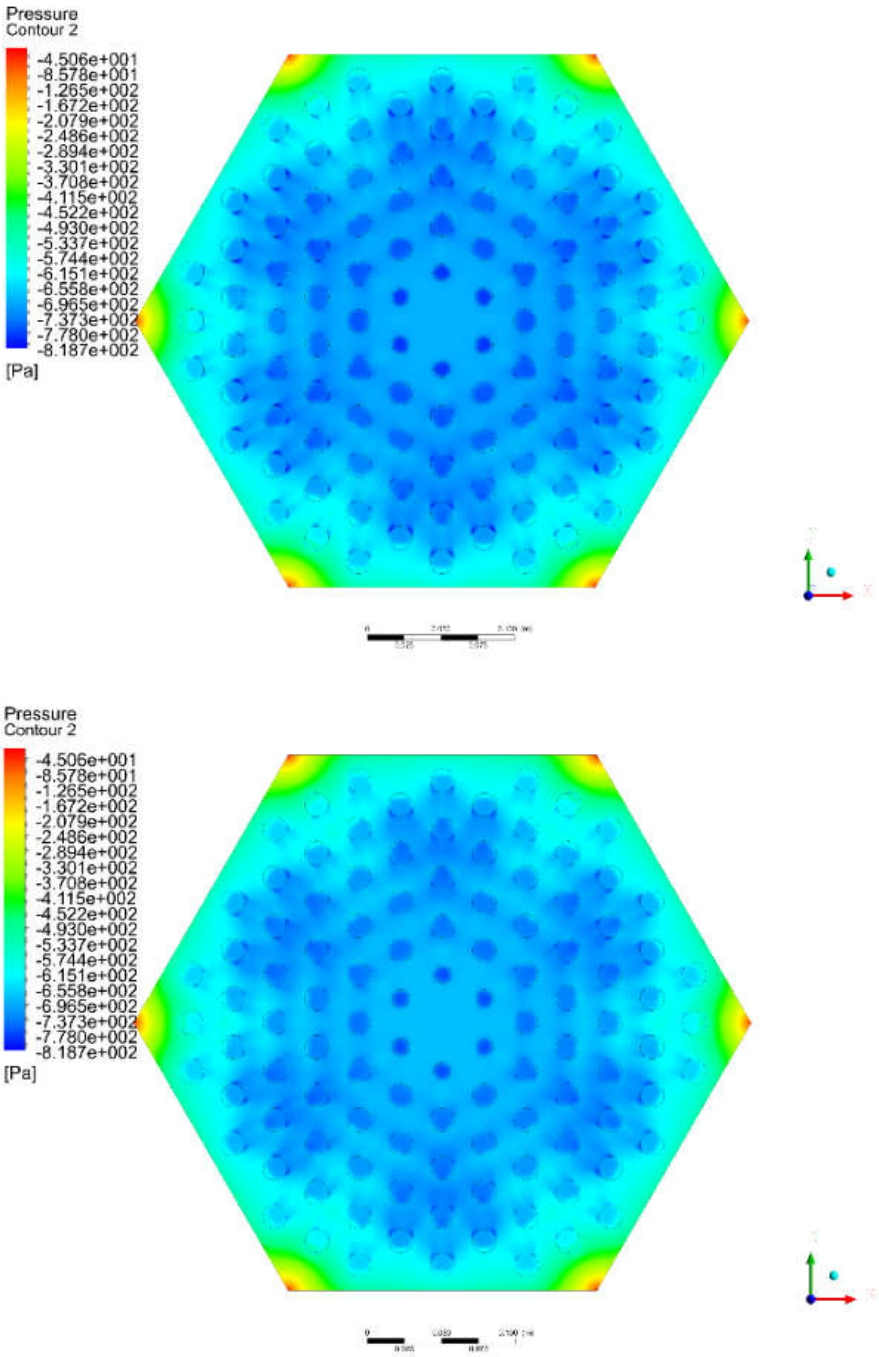

Figure A.8 Pressure distribution at the cross gap in radial direction (left: high y^+, right: low y^+)

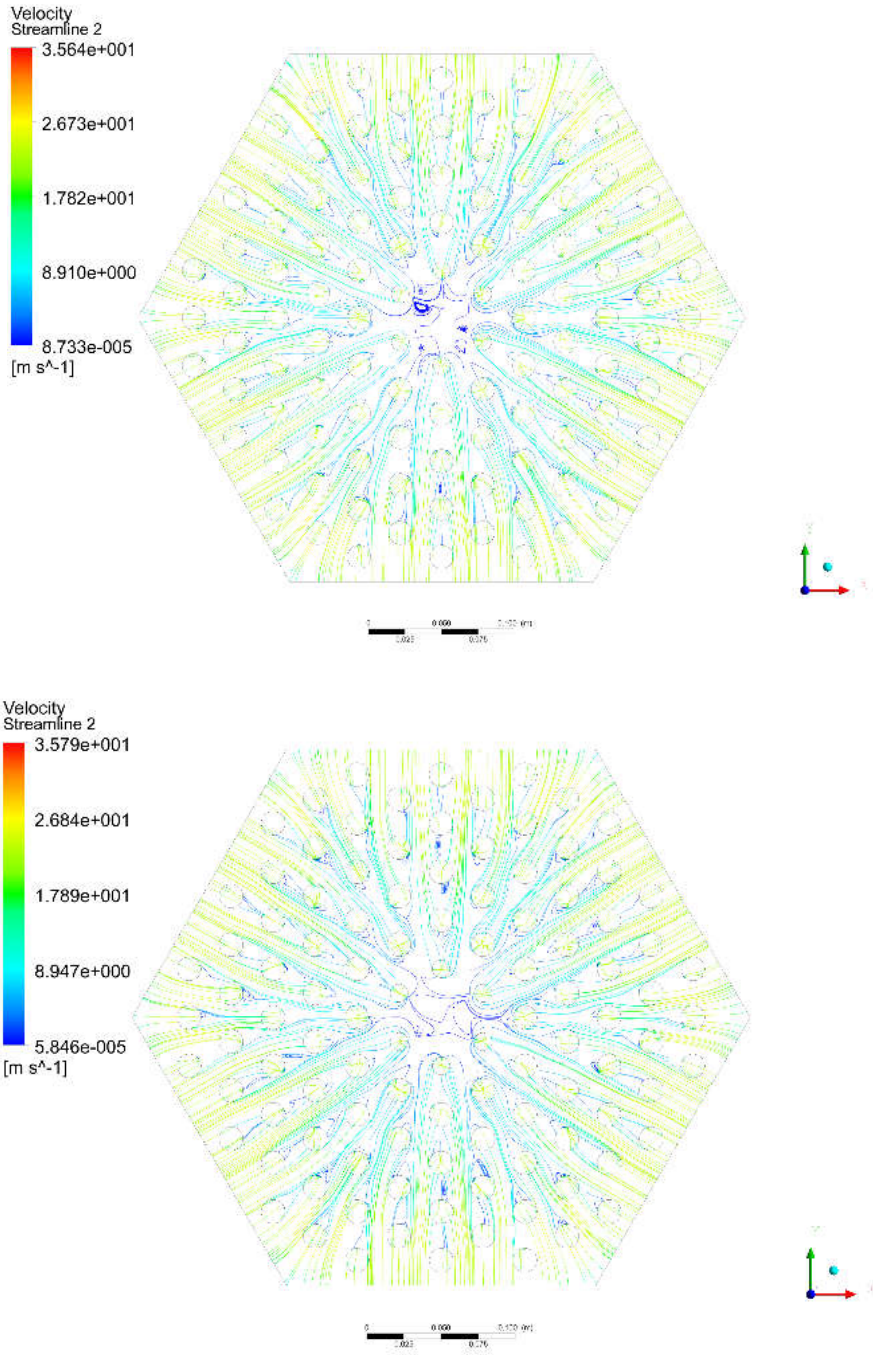

Figure A.9 Velocity streamline at cross gap in radial direction (left: high y^+, right: low y^+)

국문 초록

블록형 초고온가스로의 노심은 육각기둥 형태의 핵연료 블록과 흑연 반사체 블록을 적층한 형태로 구성된다. 구조적 특성으로 인하여 블록 사이에 간극이 존재하며, 중성자 조사로 인한 흑연의 수축으로 운전주기 동안 간극의 크기가 변하게 된다. 노심우회유량비가 증가하게 되면, 냉각채널의 유량이 감소하게 되고, 이는 열 제거 효율을 저해하여 핵연료 블록의 국부적인 과열을 초래할 수 있다. 더욱이, 간극 크기의 변화는 노심 유동분포의 불확실성을 증가시켜 열적 여유도에 대한 평가를 어렵게 만든다.

최근에는 CFD (computational fluid dynamics) 코드가 초고온가스로의 노심의 유동에 대한 거동을 이해하는 기법 중 하나로 많은 주목을 받고 있다. 그러나 CFD 코드로 노심 전체를 해석하기에는 많은 계산 비용과 시간이 소요되어 현실성이 매우 떨어진다. 다른 방법으로 lumped 변수를 사용하는 시스템 코드를 이용하는 방법이 있지만, 해석 결과의 정확도가 낮은 단점이 있다. 따라서, 블록형 초고온가스로의 노심의 유동분포를 해석하기 위해 looped network analysis method를 활용한 FastNet (Flow Analysis for Steady-state Network) 코드가 본 연구를 통해 개발되었다.

유동 네트워크 해석 코드는 유로를 저항의 네트워크로 나타내어 해석하는 방법으로 주어진 형상에서 압력손실과 유속 사이의 관계가 필요하다. 초고온가스로의 노심은 크게 냉각채널, 우회유로, 횡류유로로 구성된다. 이 중 냉각채널과 우회유로는 유량과 압력강하의 관계를 나타내는 해석해가 존재하지만 횡류간극은 복잡한 형상으로 인해 쉽게 해석할 수 없다. 또한, 횡류간극은 냉각채널과 우회간극을 연결하는 유로로 노심의 유동분포를 복잡하게 만드는 요인 중 하나이다. 따라서 초고온가스로의 노심 횡류유동의 거동특성을 파악하

기 위해 횡류유동 실험이 수행되었고, CFD 해석과의 비교를 통해 CFD의 횡류유동 현상에 대한 적용성을 검증하였다. 실험 결과와 CFD 해석 결과가 잘 일치하였으며, 계산 결과와 실험결과를 통해 횡류유동 압력 손실계수 상관식을 개발하였다. 개발된 상관식은 FastNet에 적용되어 노심 유동분포 해석의 정확성이 향상되었다.

FastNet 코드에서 열전도 해석을 위한 solid mesh는 한 블록당 6개의 cell을 할당하기 때문에, 유효열전도도 (Effective Thermal Conductivity) 모델을 채택하였다. 이 모델을 통해 다수의 매질에 대한 열전도도는 하나의 균질화된 전도도로 변환되어 사용할 수 있다. 또한 unit cell을 사용하여 핵연료 최고온도를 예측할 수 있는 Maximum Fuel Temperature 모델을 적용하였다.

FastNet의 유동분포 해석능력에 대한 검증을 위해 SNU multi-block 실험결과를 이용하였다. 또한, 단일칼럼 해석과 전노심 해석에 대한 계산결과를 CFD 코드 및 CORONA 코드의 해석 결과와의 비교를 통해 FastNet의 전체적인 계산능력을 평가하였다. 단일칼럼 및 전노심 해석에서 FastNet은 매우 빠른 계산 속도 뿐만 아니라 비교적 높은 정확도를 보여주었다.

검증결과를 통해 FastNet은 블록형 초고온가스로의 노심 유동분포와 온도분포 해석에 대한 신뢰할 수 있는 계산결과를 제공할 수 있다고 판단되며, 초고온가스로 노심의 열적 여유도 평가에 기여할 수 있을 것으로 판단된다.

주요어

초고온가스로, VHTR, FastNet, 우회유동, 횡류유동, 네트워크코드, 유동네트워크해석, Looped network analysis, 압력손실계수, 압력손실계수상관식, 실험, 전산유체해석, 코드검증

학번: 2012-30267